

**MEASUREMENTS OF ANNULAR COUETTE  
FLOW STABILITY AT THE FLUID  
REYNOLDS NUMBER  $\text{Re} = 4.4 \times 10^6$ :  
THE FLUID DYNAMIC PRECURSOR  
TO A LIQUID SODIUM  $\alpha\omega$  DYNAMO**

by

Howard Foster Beckley

Submitted in Partial Fulfillment  
of the Requirements for the Degree of  
Doctor of Philosophy in Physics

New Mexico Institute of Mining and Technology  
Socorro, New Mexico  
December, 2002

## ABSTRACT

I present this dissertation as the result of the design, development, construction, and fluid dynamic operation of an experimental liquid sodium  $\alpha\omega$  dynamo. The culmination of this work is the laboratory operation of the dynamo apparatus that tests and verifies the operation of the rotating experiment and the ability of the apparatus to create and sustain stable annular Couette flow at very high Reynolds number. The data reported in this dissertation approaches the last laboratory engineering phase and is the first phase of scientific operation of the dynamo apparatus.

Stable annular Couette flow is defined as the non-turbulent, laminar, azimuthal fluid flow between two co-directionally rotating cylinders. The flow is described by an angular frequency parameter  $\Omega(R)$ . The theoretical range over which annular Couette flow can be stable is where  $\Omega = \text{constant}$ , i.e. solid-body rotation, to  $\Omega \propto 1/R^2$ , i.e. maximum stable laminar differential shear. The radius ratio of inner to outer cylinders is  $R_1:R_0 = 1:2$ ; thus the rotation rate scales from 1:1 for solid-body, to 4:1 for maximum stable differential shear. The cylindrical radii are  $R_1 = 15.25$  and  $R_0 = 30.50$  cm.

The apparatus is designed to withstand the mechanical stress, with a factor of three safety, of differential rotation frequencies at 120 Hz and 30 Hz for the inner and outer cylinders respectively. The maximum stress induced by the pressure of the differentially rotating fluid at the maximum rate condition is 72 atm. During part of the engineering test phase the apparatus was successfully

hydrostatically pressure tested to 24 atm. This value, 1/3 of the maximum pressure stress, was chosen for two reasons, one being mechanical safety that is detailed in the dissertation body itself. The second was that it would intentionally coincide with the predetermined upper limit of safe rotation frequencies that could be achieved in the laboratory. The imposed upper limit was 10% of the maximum yield stress of the rotating mass of the apparatus. This translates to 1/3 the maximum differential rotation velocity, since  $\Omega \propto v$ .

In the laboratory tests, using the limiting rotation frequencies of 40 Hz and 10 Hz, the resulting maximum Reynolds number for the annular Couette flow was  $\text{Re}_{H_2O} = 4.4 \times 10^6$ . The importance of this result is that it is significantly greater than previous values of similar flow configurations by a factor of 20. Efforts were made to acquire reliable torque and power data reported in this dissertation. Subsequent error analysis of the data and comparison to hydrodynamic theory provide evidence, as predicted, that the annular Couette flow in the dynamo apparatus was stable at  $\text{Re} = 4.4 \times 10^6$ .

The impetus for this project has been to build an experiment that could simulate one of the possible types of dynamo processes of magnetic field creation and sustainment believed to operate in nature on size scales ranging from planets, convective envelopes of stars, accretion disks, galactic disks, and on the largest scale, possibly in clusters of galaxies.

The basis of the present design of the liquid sodium  $\alpha\omega$  dynamo I have built, tested and operated is to create an apparatus that can differentially rotate a stable annular flow of liquid sodium. Subsequently we may add to the apparatus the injection of axially-aligned periodic plumes within the annulus. Differen-

tial rotation results in the magnetodynamic effect of the  $\omega$ -deformation, and the  $\alpha$ -helicity is the magnetohydrodynamic effect of the non-axisymmetric, axially-aligned plumes. With these two flows an  $\alpha\omega$  dynamo can be investigated. The fluid dynamic results discussed in this dissertation show that the experimental apparatus is well suited to creating and analyzing the requisite fluid flow fields for the  $\omega$ -deformation component of the  $\alpha\omega$  dynamo.

## ACKNOWLEDGMENT

This project was funded by the National Science Foundation, Grant # 99-00661, Los Alamos National Laboratory, BOA # 0413J0017-23, and the New Mexico Institute of Mining and Technology.

The design, construction and initial operation of this experiment has been at the New Mexico Institute of Mining and Technology. Those involved in the conceptual design, engineering, mechanical design, and theoretical considerations of the experiment are associated with the New Mexico Institute of Mining and Technology and Los Alamos National Laboratory both located in the State of New Mexico. The experiment is therefore referred to as the New Mexico Dynamo Experiment.

The following list denotes the people associated the New Mexico Dynamo Experiment and their affiliations.

- Howard F. Beckley, New Mexico Institute of Mining and Technology
- Stirling A. Colgate, Los Alamos National Laboratory, New Mexico Institute of Mining and Technology
- James C. Weatherall, New Mexico Institute of Mining and Technology
- Rocky D. Ginanni, New Mexico Institute of Mining and Technology
- Richard Sonnenfeld, New Mexico Institute of Mining and Technology
- Hui Li, Los Alamos National Laboratory
- Philipp P. Kronberg, Los Alamos National Laboratory, University of Toronto

- Koichi Noguchi, Los Alamos National Laboratory
- Vladimir I. Pariev, University of Rochester, Los Alamos National Laboratory
- John M. Finn, Los Alamos National Laboratory

This dissertation was typeset with  $\text{\LaTeX}$ <sup>1</sup> by the author.

---

<sup>1</sup> $\text{\LaTeX}$  document preparation system was developed by Leslie Lamport as a special version of Donald Knuth's  $\text{\TeX}$  program for computer typesetting.  $\text{\TeX}$  is a trademark of the American Mathematical Society. The  $\text{\LaTeX}$  macro package for the New Mexico Institute of Mining and Technology dissertation format was adapted from Gerald Arnold's modification of the  $\text{\LaTeX}$  macro package for The University of Texas at Austin by Khe-Sing The.

# TABLE OF CONTENTS

|  |           |
|--|-----------|
| <b>LIST OF TABLES</b>  | <b>v</b>  |
| <b>LIST OF FIGURES</b>   | <b>vi</b> |
| <b>1. INTRODUCTION</b>   | <b>1</b>  |
| <b>2. THE NEW MEXICO DYNAMO EXPERIMENT: MODELING<br/>ASTROPHYSICAL DYNAMOS</b>   | <b>4</b>  |
| Abstract . . . . .   | 4         |
| 2.1 Introduction . . . . .   | 4         |
| 2.2 How the $\alpha\omega$ Dynamo Works . . . . .  | 5         |
| 2.3 Numerical Simulations of the Dynamo . . . . .  | 7         |
| 2.4 Conclusions . . . . .  | 16        |
| Acknowledgments . . . . .  | 17        |
| <b>3. ROTATION OF A PULSED JET IN A ROTATING ANNULUS:<br/>A SOURCE OF HELICITY FOR AN <math>\alpha\omega</math> DYNAMO</b> | <b>18</b> |
| Abstract . . . . .   | 18        |
| 3.1 Introduction . . . . .   | 19        |
| 3.1.1 Convection, Turbulence, Helicity, and Dynamos . . . . .  | 19        |
| 3.1.2 Plumes, Entrainment, & Mixing Length Theory . . . . .  | 22        |
| 3.1.3 Turbulent Plumes Originating from a Point Source . . . . .   | 22        |
| 3.1.4 Mixing Length Theory . . . . .   | 25        |
| 3.1.5 Plume Formation . . . . .  | 26        |
| 3.2 Plume Rotation and the $\alpha\omega$ Dynamo . . . . .   | 28        |
| 3.2.1 Plume Rotation . . . . .   | 28        |

|           |   |           |
|-----------|---|-----------|
| 3.2.2     | Plume Rotation Damping . . . . .                                    | 29        |
| 3.2.3     | Plumes in a Rotating Frame: The Origin of Dynamo Helicity           | 30        |
| 3.2.4     | The $\alpha\omega$ Dynamo . . . . .                                 | 30        |
| 3.2.5     | Consequences of Plume Helicity . . . . .                            | 31        |
| 3.2.6     | Plume Turbulence . . . . .  | 33        |
| 3.2.7     | Plume Characteristics . . . . .                                     | 34        |
| 3.3       | The Experiment . . . . .  | 35        |
| 3.3.1     | Apparatus . . . . .   | 37        |
| 3.3.2     | Subsystems . . . . .  | 38        |
| 3.3.3     | Flow Visualization Methods . . . . .                                | 39        |
| 3.4       | Results . . . . .   | 41        |
| 3.4.1     | The Rising Plume . . . . .  | 41        |
| 3.4.2     | The Rotating Plume . . . . .  | 42        |
| 3.4.3     | Convergent Flow . . . . .   | 47        |
| 3.4.4     | Differential Frame Rotation . . . . .                               | 48        |
| 3.5       | Conclusions . . . . .   | 50        |
| 3.6       | Geophysical and Astrophysical Examples . . . . .                    | 51        |
|           | Acknowledgments . . . . .   | 51        |
| <b>4.</b> | <b>DESIGN OF THE LIQUID SODIUM <math>\alpha\omega</math> DYNAMO</b> | <b>53</b> |
| 4.1       | Introduction . . . . .  | 53        |
| 4.1.1     | Background Science and Engineering Parameters . . . . .             | 56        |
| 4.2       | Design of the Experiment . . . . .                                  | 58        |
| 4.2.1     | Centrifugal Pressure . . . . .                                      | 60        |
| 4.2.2     | Power Requirements . . . . .  | 61        |
| 4.3       | Engineering of the Experimental Apparatus . . . . .                 | 63        |
| 4.3.1     | The Cylindrical Vessel . . . . .                                    | 63        |
| 4.3.2     | The End Plates . . . . .  | 64        |



|           |   |           |
|-----------|---|-----------|
| 4.3.3     | Dynamic Balance and Bearings . . . . .  | 66        |
| 4.3.4     | Seals . . . . .   | 67        |
| 4.3.5     | Thermal Properties . . . . .  | 68        |
| 4.4       | Torque Measurement Equipment and Instrumentation . . . . .  | 68        |
| 4.4.1     | Configuration for Background Torque Measurements . . . . .  | 70        |
| 4.4.2     | Configuration for Torque Transmitted by the Fluid Measure-<br>ments . . . . .                           | 70        |
| 4.5       | Safety . . . . .  | 71        |
| 4.6       | Electronic Instrumentation . . . . .  | 73        |
|           | Acknowledgments . . . . .   | 75        |
| <b>5.</b> | <b>HYDRODYNAMIC THEORY OF COUETTE FLOW AND THE<br/>EKMAN LAYER</b>                                      | <b>76</b> |
| 5.1       | Introduction . . . . .  | 76        |
| 5.2       | Couette Flow and the Ekman Layer . . . . .  | 76        |
| 5.2.1     | Annular Rotational Couette Flow . . . . .   | 80        |
| 5.2.2     | Planar Rotational Couette Flow and the Ekman Layer . . . . .  | 84        |
| 5.3       | Annular Rotational Couette Flow and the Ekman Layer:<br>Application to Experimental Operation . . . . . | 89        |
| 5.3.1     | Prediction of Torque from Ekman Layer Turbulence . . . . .  | 89        |
| 5.3.2     | Prediction of Torque from Couette Flow Turbulence:<br>An Approximation to Turbulent Pipe Flow . . . . . | 92        |
| 5.4       | Consequences of Hydrodynamic Conditions to the<br>$\alpha\omega$ Dynamo . . . . .                       | 93        |
| <b>6.</b> | <b>DATA AND ANALYSIS FROM HYDRODYNAMIC OPERA-<br/>TION OF THE NEW MEXICO DYNAMO EXPERIMENT</b>          | <b>95</b> |
| 6.1       | Introduction . . . . .  | 95        |
| 6.2       | Data Tables . . . . .   | 95        |
| 6.3       | Analysis of Torque Measurement Data . . . . .   | 102       |

|           |   |            |
|-----------|---|------------|
| 6.3.1     | Error Analysis . . . . .                                | 102        |
| 6.3.2     | Graphical Analysis of Torque Measurement Data . . . . . | 103        |
| 6.4       | Analysis of Torque Transmitted by Fluid . . . . .       | 109        |
| 6.5       | Conclusions . . . . .                                   | 115        |
| <b>7.</b> | <b>SUMMARY AND CONCLUSIONS</b>                          | <b>118</b> |
|           | <b>REFERENCES</b>                                       | <b>120</b> |

## LIST OF TABLES

|     |   |     |
|-----|---|-----|
| 6.1 | Gear Selection and RPM Values for Differential Rotation Operation<br>of the Hydrodynamic Experiments . . . . .    | 96  |
| 6.2 | Force Measurements of Solid Body Rotation . . . . .   | 98  |
| 6.3 | Force Measurements of Differential Rotation for the Outer Cylinder<br>where $\Omega_1/2\pi = 40.067$ Hz . . . . . | 99  |
| 6.4 | Force Measurements of Differential Rotation for the Outer Cylinder<br>where $\Omega_1/2\pi = 23.133$ Hz . . . . . | 100 |
| 6.5 | Force Measurements of Differential Rotation for the Outer Cylinder<br>where $\Omega_1/2\pi = 11.600$ Hz . . . . . | 101 |

## LIST OF FIGURES

|      |   |    |
|------|---|----|
| 2.1  | The Magnetic Flux Distribution of the $\alpha\omega$ Dynamo . . . . .   | 6  |
| 2.2  | The Poloidal and Toroidal Magnetic Fields in the $\omega$ Phase of the<br>Experiment . . . . .  | 11 |
| 2.3  | The Time Evolution of the Magnetic Energy of the Dynamo . . . . .   | 15 |
| 2.4  | The Dependence of the Growth Rate of the Dynamo on the Plume<br>Rate . . . . .  | 16 |
| 3.1  | A Plume Rising and Diverging in a Stratified, Stationary Atmosphere   | 23 |
| 3.2  | A Schematic Representation of a Point-Source MTT Plume Rising<br>in a Stationary Uniform Background Fluid . . . . .                       | 25 |
| 3.3  | A Schematic of the Pulsed Jet Plume . . . . .   | 28 |
| 3.4  | The $\alpha\omega$ Dynamo in a Galactic Black Hole Accretion Disk . . . . .   | 32 |
| 3.5  | The Plume Rotation Experiment Apparatus . . . . .   | 36 |
| 3.6  | Plume Rotation Experiment Schematic . . . . .   | 37 |
| 3.7  | Side View Showing the Laminar Flow Ahead of the Plume in an<br>$\Omega=0$ Static Fluid Field with a Hydrogen Electrolysis Pulse . . . . . | 41 |
| 3.8  | Side View of a Rising Plume Showing Turbulent Entrainment in an<br>$\Omega=0$ Static Fluid Field with Guanidine . . . . .                 | 42 |
| 3.9  | Top View Showing Plume Rotation in an $\Omega = \textit{const}$ Fluid Flow<br>Field with 3.3 cm Port . . . . .                            | 42 |
| 3.10 | Top View Showing Plume Rotation in an $\Omega = \textit{const}$ Fluid Flow<br>Field with 4.8 cm Port . . . . .                            | 43 |

|      |   |    |
|------|---|----|
| 3.11 | The Schematic Side and Top Views Show Respectively the Plume Divergence and Rotation in an $\Omega = \text{const}$ Rotating Frame . . . . . | 43 |
| 3.12 | Rotation of the Large Port Plume when Striking the Witness Plate as Observed with Guanidine . . . . .                                       | 44 |
| 3.13 | A Plot of the Data for the Differential Rotation of Plumes . . . . .  | 46 |
| 3.14 | Delayed Electrolysis Pulse Shows that the Base of the Plume is Co-Rotating with the Reference Frame . . . . .                               | 47 |
| 3.15 | Extended Electrolysis Pulse Showing an Overlay of the Counter-Rotation of the Plume Head and the Co-Rotation of the Plume Base              | 47 |
| 3.16 | Top View Showing Plume Rotation in an $\Omega_{\text{differential}}$ Fluid Flow Field   | 49 |
| 3.17 | Delayed Electrolysis Pulse in an $\Omega_{\text{differential}}$ Flow Field . . . . .  | 49 |
| 4.1  | $\omega$ -Phase & $\alpha$ -Phase Drawings of the Experimental Apparatus . . .  | 54 |
| 4.2  | Photograph of the New Mexico Liquid Sodium $\alpha\omega$ Dynamo Experiment . . . . .   | 59 |
| 4.3  | Photographs of the Belt Drive System and the Recirculating Oil Supply System for the Dynamo Apparatus . . . . .                             | 60 |
| 4.4  | Photograph of the New Mexico Liquid Sodium $\alpha\omega$ Dynamo Experiment . . . . .   | 67 |
| 4.5  | Photographs of the Torque Measurement Sensors and Equipment used for Hydrodynamic and Magnetodynamic Operation of the Dynamo . . . . .      | 69 |
| 4.6  | Photograph of the Rotating Electronic Instrumentation for the New Mexico Liquid Sodium $\alpha\omega$ Dynamo Experiment . . . . .           | 73 |
| 4.7  | Photograph of the Stationary Electronic Instrumentation for the New Mexico Liquid Sodium $\alpha\omega$ Dynamo Experiment . . . . .         | 74 |

|     |   |     |
|-----|---|-----|
| 4.8 | Photograph of the Radial Probe Housing used for Internal Magnetic Field Measurements . . . . .  | 75  |
| 5.1 | Schematic of the Annular Region Where Couette Flow will be Established . . . . .  | 78  |
| 5.2 | Schematic Representation of Pressure Stress and Shear Stress Components . . . . .   | 80  |
| 5.3 | Schematic Representation of Ekman Layer Induced Circulation . . .   | 85  |
| 6.1 | Torque as a Function of Frequency for Solid Body Rotation . . . . .   | 104 |
| 6.2 | Torque as a Function of Outer Cylinder Frequency for Differential Rotation where $\Omega_1/2\pi = 40.067$ Hz . . . . .                      | 105 |
| 6.3 | Torque as a Function of Outer Cylinder Frequency for Differential Rotation where $\Omega_1/2\pi = 23.133$ Hz . . . . .                      | 106 |
| 6.4 | Torque as a Function of Outer Cylinder Frequency for Differential Rotation where $\Omega_1/2\pi = 11.600$ Hz . . . . .                      | 108 |
| 6.5 | Torque Transmitted by Fluid as a Function of Outer Cylinder Frequency for Differential Rotation where $\Omega_1/2\pi = 40.067$ Hz . . . . . | 112 |
| 6.6 | Torque Transmitted by Fluid as a Function of Outer Cylinder Frequency for Differential Rotation where $\Omega_1/2\pi = 23.133$ Hz . . . . . | 113 |
| 6.7 | Torque Transmitted by Fluid as a Function of Outer Cylinder Frequency for Differential Rotation where $\Omega_1/2\pi = 11.600$ Hz . . . . . | 114 |

This dissertation is accepted on behalf of the faculty of the Institute by the following committee:

---

James C. Weatherall, Advisor

---

---

---

---

---

Howard Foster Beckley

Date

# CHAPTER 1

## INTRODUCTION

The New Mexico Dynamo Experiment is designed to demonstrate the excitation of an astrophysical-type dynamo due to non-axisymmetric plumes rising through differentially rotating liquid sodium. The fluid-dynamic operation of the dynamo apparatus that characterizes Couette flow is delineated by the *angular frequency* parameter  $\Omega$ . The fluid-dynamic operation of the dynamo apparatus used both water and a low-viscosity mineral oil as the fluid flow media. The magnetodynamic operation of the dynamo that characterizes a topological change in magnetic field configuration is delineated by the *deformation* parameter  $\omega$ . The magnetohydrodynamic operation of the dynamo that characterizes a gain in magnetic field by translation and rotation of embedded magnetic flux is delineated by the *helicity* parameter  $\alpha$ . The forthcoming magnetodynamic and magnetohydrodynamic operation of the dynamo will use liquid sodium as the electrically conducting fluid flow media.

The liquid sodium  $\alpha\omega$  dynamo experiment was designed after a water visualization experiment confirmed the existence of the two fundamental fluid motions necessary for a laboratory experiment to demonstrate the  $\alpha\omega$  dynamo. These are: (1) the maximum differential shear and stability of Couette flow and (2) the production of axially aligned diverging plumes from pulsed jets and their subsequent anticyclonic and limited rotation relative to a rotating frame. The qualitative confirmation of these fundamental flows are the basis of the design of the liquid sodium  $\alpha\omega$  dynamo apparatus. More accurate measurements will be possible of both these flows in the completed dynamo apparatus. In Chap. 2 it will



be shown how these two orthogonal flows make an  $\alpha\omega$  dynamo when produced in a conducting fluid of sufficiently large magnetic Reynolds number.

Real dynamos operate in Nature on astrophysical scales, in planets, convective envelopes of stars, galactic discs, accretion discs, and, possibly, on the largest scale in the clusters of galaxies. Since Parker (1955), most astrophysical dynamo theories, especially  $\alpha\omega$  dynamos, refer to cyclonic or anticyclonic plumes as a source of the helicity. In the case of planetary and stellar dynamos such plumes are believed to be rising and sinking convective cells (Mestel 1999, Parker 1978). Here it is invoked for both the experiment and the accretion disk dynamo anticyclonic plumes because of their finite rotation angle,  $\simeq \pi/2$  radians. In the case of Galactic dynamos, supernovae explosions can also produce the necessary anticyclonic motions (Ferrière 1993a, 1993b, 1992). Finally, the most energetic dynamos in the present day universe should exist in the accretion discs around black holes in the nuclei of active galaxies (Zeldovich 1983). The magnetic dynamo in the black hole accretion discs in the centers of galaxies could be due the stars passing through the accretion disc and producing the plumes of heated gas. These plumes rise above the disc plane, expand and produce anticyclonic motion necessary for the operation of an  $\alpha\omega$  dynamo (Colgate 2001, Pariev 2001).

There are two important similarities in all these types of dynamos, and it represents the fundamental difference between nature's dynamos and man's mechanical dynamos. The first and primary similarity is that they involve an electrically conducting media being either liquid or plasma, such that there is no effective insulation between conducting parcels within a volume. The second similarity is a direct result of the first such that fluid dynamic motions can invoke a magnetohydrodynamic deformation of topology, and through resistivity or reconnection, can exponentially add magnetic flux to an initial external field resulting in the growth and sustainment of a magnetic field. The important difference be-

tween industrial and fluid (liquid or plasma) dynamos is insulation of the solid conducting members, i.e. wires and plates. Thus an industrial or mechanical dynamo can produce electromagnetic energy efficiently when driven by a turbine or engine. In a liquid or plasma dynamo there is no mechanism to insulate conducting parcels. Conversely it is necessary that fluid dynamic motions be utilized to physically reconfigure volumes of the conducting media that have magnetic flux embedded within them, change the topology of the magnetic flux through rotation and translation, decouple it from its initial source all in order to have a resulting gain in the overall magnetic field. In addition the time scale must be less than that of the resistive diffusion decay rate within the conducting media.

The plan of this dissertation is to discuss how an  $\alpha\omega$  dynamo works in Chap. 2. Included in Chap. 2 are the results of the numerical simulation of the dynamo growth rate with boundary conditions expected to be achieved in the experiment. V. Pariev performed the numerical simulations based on the theory developed by himself and S.A. Colgate. H.F. Beckley and S.A. Colgate provided the background data required to have the simulations accurately represent the mechanical and operational parameters of the experimental apparatus. Chapter 3 will review the practicality of creating the necessary flow geometry as demonstrated in water visualization experiments. The actual design and construction features of the experiment are discussed in Chap. 4. In Chap. 5 the development of the theoretical fluid dynamics involved with the experimental operation of the apparatus is set forth. Chapter 6 concludes this dissertation with the experimental data, the results and the analysis.

## CHAPTER 2

# THE NEW MEXICO DYNAMO EXPERIMENT: MODELING ASTROPHYSICAL DYNAMOS<sup>1</sup>

### Abstract

A magnetic dynamo experiment is under construction at the New Mexico Institute of Mining and Technology. The experiment is designed to demonstrate in the laboratory the  $\alpha\omega$  magnetic dynamo, which is believed to operate in many rotating and conducting astrophysical objects. The experiment uses the Couette flow of liquid sodium between two cylinders rotating with different angular velocities to model the  $\omega$ -effect. The  $\alpha$ -effect is created by the rising and expanding jets of liquid sodium driven through a pair of orifices in the end plates of the cylindrical vessel, presumably simulating plumes driven by buoyancy in astrophysical objects. The water analog of the dynamo device has been constructed and the flow necessary for the dynamo has been demonstrated. Results of the numerical simulations of the kinematic dynamo are presented. The toroidal field produced by the  $\omega$ -effect is predicted to be  $B_\phi \simeq (R_m/2\pi)B_{poloidal} \simeq 20 \times B_{poloidal}$  for the expected magnetic Reynolds number of  $R_m \sim 120$ . The critical rate of jets necessary for the dynamo self-excitation is predicted from the calculations to be a pair of plumes every 4 revolutions of the outer cylinder. For reasonable technical limitations on the strength of materials and the power of the drive, the self-excitation of the dynamo appears to be feasible.

### 2.1 Introduction

Recent years have been marked by exciting developments in the field of MHD dynamos, in particular the experimental realization of homogeneous dynamos was achieved. After many years of research and preparations, an expo-

---

<sup>1</sup>Portions of this chapter were submitted to *Magnitnaya Gidrodinamika*: Colgate, S.A., Pariev, V., Beckley, H.F., Ferrel, R., Romero, V.D., and Weatherall, J.C., The New Mexico  $\alpha\omega$  Dynamo Experiment: Modeling Astrophysical Dynamos, *Magnitnaya Gidrodinamika*, Accepted, Aug. 28, 2001.

nentially growing dynamo mode was observed in the experiment conducted in a liquid-sodium facility in Riga, Latvia (Gailitis 2001, Gailitis 2000). This experiment reproduces the simplest dynamo flow proposed by Parker (1955) and also subsequently by Ponomarenko (1973) in the laboratory. Another successful dynamo experiment of a different type was built in Karlsruhe, Germany. This experiment verifies the ability of a regular spatial arrangement of vortices to amplify the magnetic field. The growth of the magnetic field starting from the initial seed value of  $\approx 1$  Gauss up to  $\approx 70$  Gauss was observed in Karlsruhe experiment (Stieglitz 2001). The magnetic field reached the back-reaction, saturated limit, and the excitation of the non-axisymmetric mode predicted by the theory was observed. There are a number of other dynamo experiments, which are under preparation or discussion. Each of these experiments is designed to test different flow patterns capable of dynamo action. All these experiments (except Karlsruhe experiment) are designed to use axisymmetric rotating flows, either stationary or non-stationary. We designed another kind of dynamo experiment, which will use essentially non-axisymmetric, non-stationary flows.

Here, because the flow is non-stationary and non-axisymmetric, then in both cases the field averaged over many plume ejections will approach a near steady state of axisymmetric symmetry. The flux from such a dynamo thus may simulate the astrophysical fluxes observed on large scales.

## 2.2 How the $\alpha\omega$ Dynamo Works

Figure 2.1(A) shows how the  $\alpha\omega$  dynamo works in the New Mexico Dynamo Experiment and Fig. 2.1(B) shows how the  $\alpha\omega$  dynamo works in the accretion disk forming the massive, central galactic black hole. In Fig. 2.1(A) differential rotation is established in the liquid sodium between two rotating cylinders as limiting stable Couette flow,  $\Omega \propto 1/R^2$ , by driving  $\Omega_1 = 4\Omega_0$  where  $R_0 = 2R_1$  and for the disk Fig. 2.1(B) as Keplerian rotation,  $\Omega \propto 1/R^{-3/2}$ , around the central

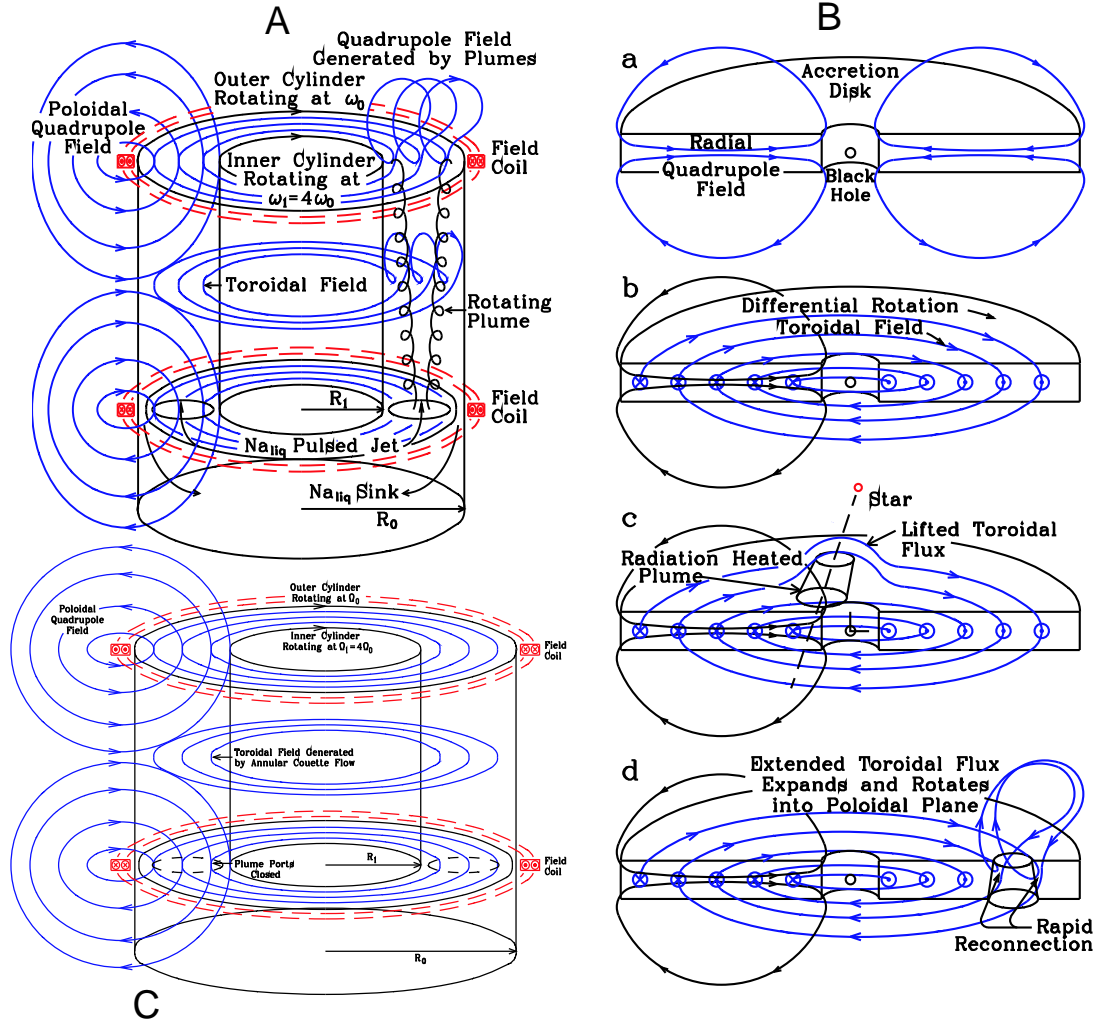


Figure 2.1: A schematic of the sodium dynamo experiment Fig. 2.1(A) in comparison to the accretion disk dynamo of Fig. 2.1(B). In both cases differential rotation in a conducting fluid wraps up an initial poloidal, radial field component into a much stronger toroidal field. Then either liquid sodium plumes driven by pulsed jets or star-disk collisions eject and rotate a loop of toroidal flux into the poloidal plane. Resistivity or reconnection merges this new or additional poloidal flux with the original poloidal flux leading to dynamo gain. Figure 2.1(C) shows the  $\omega$ -phase of the dynamo, Phase I of this experiment. The multiplication of the poloidal field by the differential shear flow produces an enhanced toroidal field which can be directly measured with large signal to noise ratio.

mass or the black hole. This differential rotation wraps up the radial component of an initial poloidal field Fig. 2.1(B(a)) either made with coils or an infinitesimally small,  $< 10^{-19}$  G seed field from density structure at decoupling. The resulting toroidal field becomes stronger than the initial poloidal field Fig. 2.1(B(b)) by  $B_{toroidal}/B_{poloidal} = n_{\Omega}B_{poloidal}$ , where in equilibrium with resistive decay, the limiting number of turns becomes  $n_{\Omega} \simeq R_{m,\Omega}/2\pi$ , and  $R_{m,\Omega} = v_0(R_0 - R_1)/\eta$  is the magnetic Reynolds number. This multiplication factor depends upon the resistivity of liquid sodium or for the disk, upon the resistivity of the ionized and turbulent plasma. Then a driven pulsed jet or a collision with the disk by a star, Fig. 2.1(B(c))] causes a plume to rise either toward the end plate or above the disk with the corresponding displaced toroidal flux forming a loop of toroidal flux. The radial expansion of the plume material causes the plane of this loop to untwist or rotate differentially about its own axis relative to the rotating frame so that the initial toroidal orientation of the loop is transformed to a poloidal one, Fig. 2.1(B(d)).

Resistive diffusion in liquid sodium metal or reconnection in the ionized plasma of the disk allows this now poloidal loop to merge with the original poloidal field. For positive dynamo gain, the rate of addition of poloidal flux must be greater than its decay. It is only because the toroidal multiplication can be so large or that  $R_{m,\Omega}$  can be so large that the helicity necessary for gain of the  $\alpha\omega$  dynamo can be much smaller and episodic.

### 2.3 Numerical Simulations of the Dynamo

At the current stage of numerical modeling of the New Mexico Dynamo Experiment we assumed the following simplified model. We consider the flow of the liquid sodium only inside the cylindrical, annular, space bounded by the radii  $R_1$  and  $R_0$  and the end plate and port plate at  $z = L/2$  and  $z = -L/2$ . The walls are assumed perfectly conducting. In view of the conductivity of aluminum walls

being higher than the sodium, this assumption qualitatively predicts the evolution of magnetic fields and the growth rate of the dynamo. However, to obtain more accurate results, one needs to consider more realistic boundary conditions taking into account the finite thickness of the walls, the insulating air, i.e., vacuum, outside the device, and the plenum filled with liquid sodium at one end. We also assume a simplified kinematic model for the flow and do not actually solve the hydrodynamic equations. In other words we do not take into account the ponderomotive force ( $\mathbf{j} \times \mathbf{B}$ ).

The kinematic dynamo equation is

$$\frac{\partial \mathbf{B}}{\partial t} = -\nabla \times (\eta \nabla \times \mathbf{B}) + \nabla \times (\mathbf{v} \times \mathbf{B}), \quad (2.1)$$

where  $\eta$  is the a coefficient of magnetic diffusivity,  $\eta = \frac{c^2}{4\pi\sigma}$ . Instead of solving the dynamo equation for  $\mathbf{B}$  we introduce potentials  $\mathbf{A}$  and  $\varphi$ . Using the gauge condition  $c\varphi - \mathbf{v} \cdot \mathbf{A} + \eta \nabla \cdot \mathbf{A} = 0$  one can derive the following equation for the evolution of the vector potential  $\mathbf{A}$

$$\frac{\partial A^i}{\partial t} = -A_k \frac{\partial v^k}{\partial x^i} - v^k \frac{\partial A^i}{\partial x^k} + \eta \frac{\partial^2 A^i}{\partial x^k \partial x_k}, \quad (2.2)$$

where the magnetic diffusivity  $\eta$  is assumed to be constant throughout the cylinder and the coordinate notations refer to a Cartesian coordinate system  $x^i$ . We use our 3D kinematic dynamo code to solve Eq. (2.2). Then, the magnetic field can be obtained at any time by taking the curl of  $\mathbf{A}$ . The code is written in cylindrical coordinates and uses an explicit scheme with the central spatial differencing in the advection term and the standard nine points stencil for the diffusion term. We assume all boundaries of the cylinder ( $r = R$ ,  $z = -L/2$ , and  $z = L/2$ ) to be perfect conductors. Then, the boundary conditions for  $\mathbf{A}$  at perfectly conducting boundaries compatible with the gauge can be chosen as follows: the components of  $\mathbf{A}$  parallel to the boundary are zeros and the divergence of  $\mathbf{A}$  at the boundaries

is zero. This gives three boundary conditions for three components of the vector potential.

We use the following dimensionless units: the unit of length is the outer radius of the test volume,  $R_0$ , the unit of velocity is the azimuthal velocity of the outer cylinder,  $\Omega_0 R_0$ . Therefore, the outer cylinder makes one revolution during the dimensionless time  $2\pi$ , the inner cylinder makes one revolution during the dimensionless time  $\pi/2$ . The critical Couette velocity profile is assumed,  $\Omega = 1/r^2$  in our units. The inner radius is  $1/2$  in our units, the length of the test volume is 1. In order to account for the conducting material inside the inner cylinder we extended our computational region toward  $r = 0.5$  and assumed solid body rotation for  $r < 0.2$  with the angular velocity equal to the angular velocity of the inner cylindrical wall of the test volume. We work in cylindrical coordinates with the axis of rotation centered on the axis of symmetry of the device. The  $z = -0.5$  plane is the port plate of the test volume, the  $z = 0.5$  plane is the end plate of the test volume.

We assume that there is a bias magnetic field produced by external coils and frozen in the ideally conducting boundaries. To approximate this field we choose the initial conditions in the form  $A_r = 0$ ,  $A_z = 0$ ,  $A_\phi = r(z + 0.5)$ . Then, the initial magnetic field is  $B_r = -r$ ,  $B_z = 2(z + 0.5)$ ,  $B_\phi = 0$ . This poloidal field satisfies the equation  $\nabla^2 \mathbf{B} = 0$  and, therefore, is unchanged if only rotation is present.

First, we do simulations without plumes, when the flow velocity inside the device is Couette flow given by

$$\Omega = \frac{\Omega_1 R_1^2}{r^2} = \frac{\Omega_0 R_0^2}{r^2}. \quad (2.3)$$

Both the poloidal and stationary state toroidal fields are shown in Fig. 2.3 for  $Rm_\Omega = 120$ . The ratio of the toroidal field to the poloidal field is  $\sim 20$  and



depends on the position of measurement inside the test volume. The toroidal field near the end plate has the opposite sign from the toroidal field in the middle of the test volume. The reversal of the sign of the toroidal magnetic field can be understood in terms of the conservation of total flux of the toroidal magnetic field through the cross section of the cylindrical computational space. Since this space is bounded by an ideal conductor, the total magnetic flux cannot change. Initially, the toroidal magnetic field was zero, so the total net flux of the toroidal magnetic field should remain zero. Therefore, regions of the magnetic field with different signs must exist in the rotating liquid. Of course, there is no actual discontinuity of the fluid velocity near the end plates of the test volume. Instead, the Ekman boundary layers develop at the end plates. However, the approximation of the Ekman layer by a mathematical discontinuity of the toroidal velocity near the end plates has very little effect on the structure of the magnetic fields excited in the conducting rotating fluid under the conditions of the experiment.

Next, we modeled the kinematic dynamo produced by jets of sodium together with the Couette differential rotation. The plume flow is interposed onto a background Couette differential rotation occupying the whole computational domain  $\mathbf{v}_c = \frac{1}{r}\mathbf{e}_\phi$ . A jet of liquid sodium is simulated by a vertically progressing cylinder of radius  $r_p$  in the co-rotation frame that starts at the port plate of the disk located at  $z = -L/2$  and emerges to a height of  $z = L/2$ . At the same time the cylinder axis moves with the local Couette velocity. By the time the plume reaches its highest point the jet cylinder rotates by  $\pi$  radians. The cylinder does not rotate with respect to the rest frame. Therefore, in the frame rotating with the Keplerian velocity, it untwists by  $\pi$  radians during the time it rises. At the same time the axis of the cylinder moves by  $\pi$  radians around the central axis participating in the rotation with the Couette speed. The length of the cylinder increases with time and its velocity,  $v_{pz} \approx v_c$ . The vertical velocity of the liquid inside the cylinder is constant and is equal to  $v_{pz}$ . After the time the plume

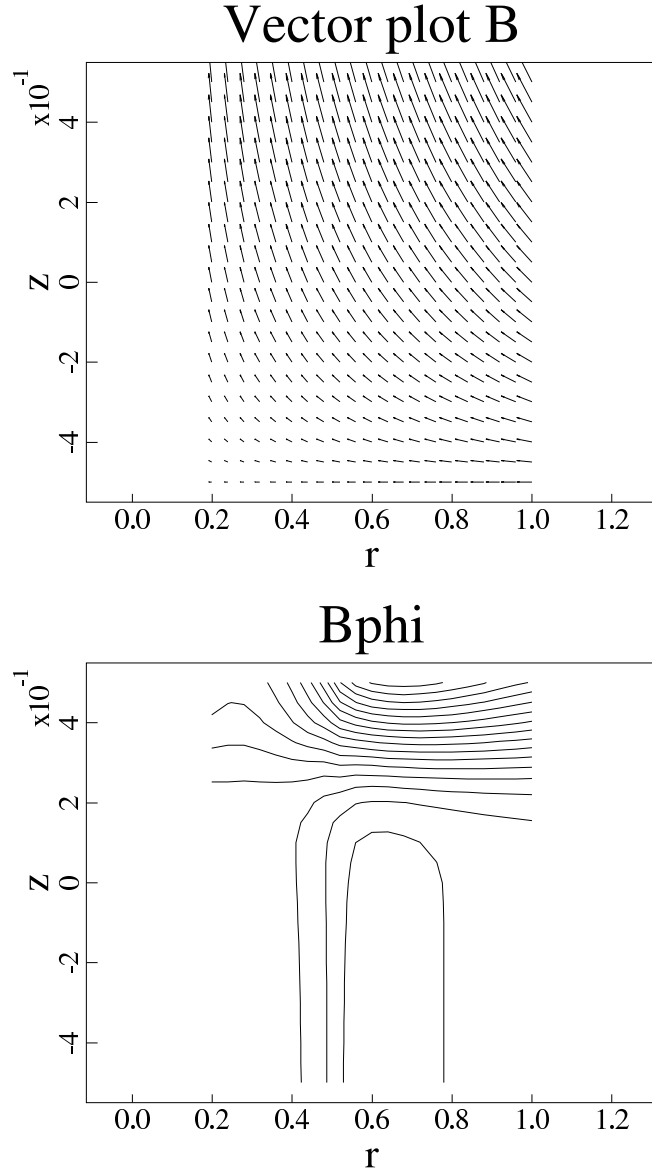


Figure 2.2: The top panel shows the poloidal magnetic field and the bottom panel shows the contours of equal values of the toroidal magnetic field. The toroidal magnetic field is shown after the steady state between stretching and diffusion of the magnetic field has been reached.

rotates by  $\pi$  it is stopped and the velocity field is restored to be pure Couette differential rotation everywhere. This very simplified flow field captures the basic features of the actual and complicated flow produced by the driven sodium jets. We note, however, that in view of the water visualization experiments that this

approximation of constant radius plumes may be a conservative approximation, because the actual plumes diverge in radius leading to a progressive increase in  $R_{m,plume}$ .

Since Eq. (2.2) requires spatial derivatives of the velocity components, we apply smoothing of discontinuities in the flow field described above. Also we introduce smooth switching on and off of the jets in time. For all three components of velocity  $v^k$  we use the same interpolation rule, which for two plumes is

$$v^k = v_{in1}^k s_1 + v_{in2}^k s_2 + (1 - s_1 - s_2) v_{out}^k. \quad (2.4)$$

Here  $s_1(r, \phi, z, t)$  and  $s_2(r, \phi, z, t)$  are smoothing functions for plume 1 and 2 correspondingly. Each function  $s$  is close to 1 in the region of space and time occupied by the plume and is close to 0 in the rest of space and during times when the plume is off. Transition from 1 to 0 happen in a narrow layer at the boundary of the plume and during the interval of time short compared to the characteristic time of the plume rise.  $v_{in1}^k$  and  $v_{in2}^k$  are velocities of the flow of plumes 1 and 2,  $v_{out}^k$  is the velocity of the flow outside the regions occupied by the plumes. For spatial derivatives of the velocity components, one has from expression (2.4)

$$\begin{aligned} \frac{\partial v^k}{\partial x^i} = & \frac{\partial s_1}{\partial x^i} (v_{in1}^k - v_{out}^k) + \frac{\partial s_2}{\partial x^i} (v_{in2}^k - v_{out}^k) + \\ & s_1 \frac{\partial v_{in1}^k}{\partial x^i} + s_2 \frac{\partial v_{in2}^k}{\partial x^i} + (1 - s_1 - s_2) \frac{\partial v_{out}^k}{\partial x^i}. \end{aligned} \quad (2.5)$$

It is easy to extend this approach for the case of arbitrary number of plumes.

Let us assume that the cylindrical jet, going in the positive direction of the  $z$  axis, is launched at the position of the axis of the jet at  $r = r_0$  and  $\phi = \phi_0$ . Let us denote this plume as number 1 and the symmetric plume also ejected at the same time as number 2. Then, after time  $(t - t_p)$  from the starting moment of the plume  $t = t_p$ , its position is

$$\phi_1 = \phi_0 + (t - t_p) r_0 \Omega_{c0}, \quad (2.6)$$

where  $\Omega_{c0} = \Omega_c(r_0)$  is the Couette angular rotational velocity at  $r = r_0$ . The position of the axis of the symmetric plume is

$$\phi_2 = \phi_1 + \pi. \quad (2.7)$$

The radii of both plumes are  $r_p$ . The originating surface of the plumes 1 and 2 is at the port plate at  $z = -L/2$ . The leading surface of the plume 1 is at  $z_1 = -L/2 + v_{pz}(t - t_p)$  and the leading surface of the plume 2 is  $z_2 = z_1$ . The velocity field inside the upward jet number 1 is

$$v_1^r = r_0 \Omega_{c0} \sin(\phi - \phi_1), \quad (2.8)$$

$$v_1^\phi = r_0 \Omega_{c0} \cos(\phi - \phi_1), \quad (2.9)$$

$$v_1^z = v_{pz}. \quad (2.10)$$

The same velocity field given by expressions (2.8–2.10) is inside the jet number 2 with the obvious replacement of  $\phi_1$  by  $\phi_2$ . We choose the following interpolation functions

$$s_1 = \left( \frac{1}{2} + \frac{1}{\pi} \arctan \frac{r_p^2 - r_1'^2}{2r_p \Delta} \right) \left( \frac{1}{2} + \frac{1}{\pi} \arctan \frac{(z + L/2)(z_1 - z)}{\Delta \sqrt{(z_1 + L/2)^2 + \Delta^2}} \right) S(t) \quad (2.11)$$

and

$$s_2 = \left( \frac{1}{2} + \frac{1}{\pi} \arctan \frac{r_p^2 - r_2'^2}{2r_p \Delta} \right) \left( \frac{1}{2} + \frac{1}{\pi} \arctan \frac{(z + L/2)(z_2 - z)}{\Delta \sqrt{(z_2 + L/2)^2 + \Delta^2}} \right) S(t). \quad (2.12)$$

Here  $r_1'^2 = r_0^2 + r^2 - 2r_0 r \cos(\phi - \phi_1)$  is the distance from the axis of the plume 1,  $r_2'^2 = r_0^2 + r^2 - 2r_0 r \cos(\phi - \phi_2)$  is the distance from the axis of the plume 2,  $\Delta$  is the thickness of the transition layer of the functions  $s_1$  and  $s_2$  from their value 1 inside the plume to 0 outside the plume,  $\Delta \ll r_p$ . The square root expressions in  $z$ -parts of  $s_1$  and  $s_2$  ensure that the thickness of the transition layer in the  $z$  direction is never less than  $\Delta$ , even just after the plumes are started, when the differences  $(z_1 + L/2)$  and  $(z_2 + L/2)$  are zero. We choose  $\Delta = 0.01$ .

The function  $S(t)$  ensures a smooth “turning on” and “turning off” of the plumes at prescribed moments of time. If the plumes are to be started at  $t = t_p$  and to be terminated at  $t = t_d$  ( $t_d > t_p$ ), then we adopt the following form of the function  $S(t)$

$$\begin{cases} S(t) = 0, & \text{for } t < t_p - \delta t/2, \\ S(t) = \frac{1}{2} + \frac{1}{2} \sin\left(\pi \frac{t-t_p}{\delta t}\right), & \text{for } t_p - \delta t/2 < t < t_p + \delta t/2, \\ S(t) = 1, & \text{for } t_p + \delta t/2 < t < t_d - \delta t/2, \\ S(t) = \frac{1}{2} - \frac{1}{2} \sin\left(\pi \frac{t-t_d}{\delta t}\right), & \text{for } t_d - \delta t/2 < t < t_d + \delta t/2, \\ S(t) = 0, & \text{for } t > t_d + \delta t/2. \end{cases}$$

where  $\delta t$  is the length of the transition period.  $S = 0$  corresponds to the flow without plumes,  $S = 1$  corresponds to the flow with plumes. One needs to ensure that  $\delta t < t_d - t_p$ . We took  $\delta t = (t_d - t_p)/5$ . The cycles with the cylindrical jets present are interchanged periodically with the cycles without such jets and with the pure Couette rotation only. The time between two subsequent ejections is  $\Delta t_p$  and we always have  $\Delta t_p > t_d - t_p$ , such that at any time only one pair of plumes are present.

We take the radius of the jet  $r_p = 0.21$ , the position of the center of the jet at  $r_0 = 0.71$ , and the vertical velocity of the flow inside the rising cylinder  $v_{pz} = 0.63$ . The radius of the jet is chosen to be the maximum possible, and the vertical velocity of the liquid in the jet requires only moderate power of the piston driving mechanism. The vertical velocity of the plume is chosen such that the plume reaches the end plate during the time when the fluid at the radius of the plume rotates by the angle  $\pi$ . During this same time the plume rotates clockwise by  $\approx \pi$  radians in the local Couette rotating frame. Such a timing should maximize the release of the poloidal magnetic flux due to the diffusion out of the twisting plume into surrounding conducting fluid. After the plume reaches the end plate, the velocity field of the flow is smoothly set back to the pure Couette profile without further poloidal motions. There are two identical plumes ejected simultaneously through the two orifices located symmetrically with respect to the

rotation axis of the device. We performed simulations with different time intervals between subsequent plume ejections. We looked at the various rates of: (1) one pair of plumes per one revolution of the outer cylinder (i.e., per  $2\pi$  units of time), (2) one pair of plumes per two revolutions of the outer cylinder, (3) one pair of plumes per three revolutions of the outer cylinder, and so on, until the dynamo could no longer be excited. The typical curve of the energy growth of the magnetic field is presented in Fig. 2.3. The dependence of the growth rate of the dynamo vs. the rate of plumes (the rate is the inverse of the number of revolutions of the outer cylinder,  $N$ , per one ejected pair of plumes) is shown in Fig. 2.3. One can see that the threshold for the dynamo excitation is somewhere between one pair of plumes per 4 revolutions and one pair of plumes per 5 revolutions. The smallest point on the graph for  $N = 5$  may not have converged numerically, and so is likely to be below the axis where  $\gamma = 0$ .

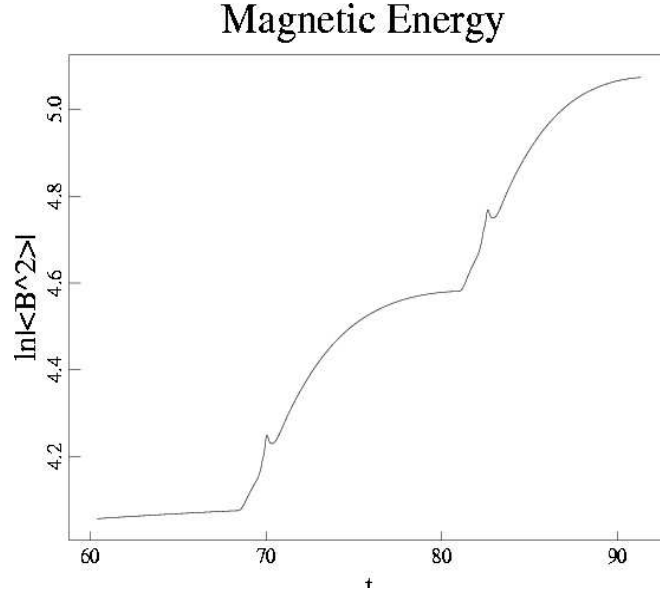


Figure 2.3: Part of one simulation for one pair of plumes per three revolutions showing exponential growth of the dynamo. The small spikes on the graph are due to the action of each single plume. The slowly rising and decaying arches are due to the production of the toroidal field from the fraction of the poloidal field added by the plume.

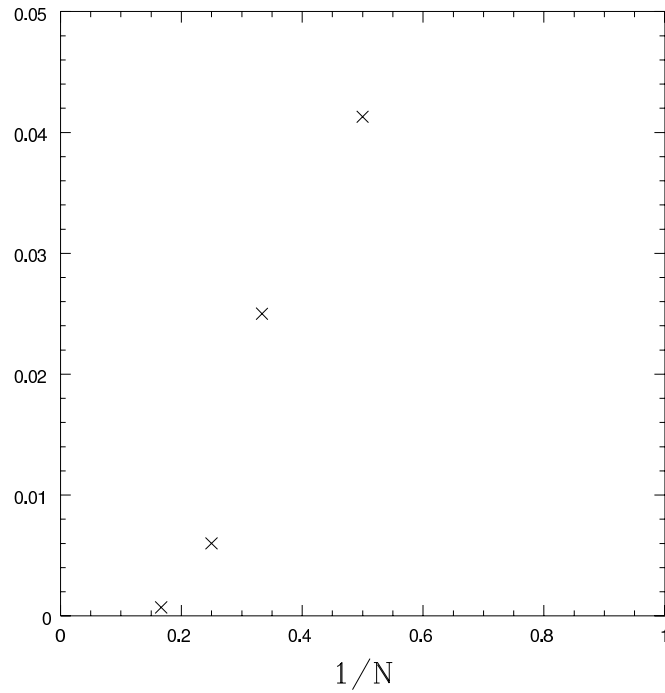


Figure 2.4: The dependence of the growth rate of the dynamo on the plume rate.  $N$  is the number of revolutions of the outer cylinder from one ejection of a pair of plumes to the next ejection of a pair of plumes.

## 2.4 Conclusions

The numerical simulations along with the engineering design feasibility give us confidence that, with a continuing effort a positive gain  $\alpha\omega$  dynamo can be made in the laboratory.

## Acknowledgments

This work was partially supported by the US Department of Energy, under contract W-7405-ENG-36 and NSF Grant 9900661. We particularly acknowledge the initial support of the New Mexico Institute of Mining and Technology, (NMIMT) through the Energetic Materials Research and Testing Center (EMRTC) that allowed this project to begin.

We would like to express our gratitude to J. M. Finn, LANL for numerous discussions on magnetic dynamos and help with the numerical code and Hui Li, LANL, for discussions on how this work joins to astrophysics.



## CHAPTER 3

# ROTATION OF A PULSED JET IN A ROTATING ANNULUS: A SOURCE OF HELICITY FOR AN $\alpha\omega$ DYNAMO<sup>1</sup>

### Abstract

A hydrodynamic flow visualization experiment was performed to investigate how an expanding plume rotates when injected off-axis into a rotating annular flow field. In the experiment the plumes were injected parallel to, but radially displaced from the axis of rotation. The plumes were observed to counter-rotate  $\Delta\phi \sim \pi/2$  to  $\pi$  radians relative to the rotating frame before dispersing into the background flow because of turbulence. The differential counter-rotation of an expanding plume in a rotating frame is the key result of the experiment. The counter-rotation of the plume is produced by the change in moment of inertia with conserved angular momentum, or equivalently, the partial conservation of circulation due to radial divergence of the flow at the head of the plume. Rapid turbulent entrainment of the plume flow with the background flow during radial divergence limits the net rotation of the plume, whereas shear within a differentially-rotating background flow enhances the net plume rotation. The coherent nature of naturally occurring buoyant plumes in a rotating flow field, i.e. *the same direction of rotation, the same vertical motion, and the finite angle of rotation for every plume*, make such plumes nearly ideal for producing the deformation of magnetic flux called the  $\alpha$ -helicity of the  $\alpha\omega$  dynamo. The  $\omega$ -deformation is the magnetodynamic effect of changing the topology of a poloidal field to that of a toroidal field by differentially winding the magnetic field in a conducting media. The  $\Omega$ -flow is the fluid dynamic effect of differential rotation of the flow field established between two coaxial cylinders whose outer radius,  $R_0=15$  cm, inner radius,  $R_1=7.5$  cm, and height,  $Z=10$  cm. The Reynolds number was  $\simeq 10^5$  in order to simulate the behavior of turbulent entrainment at high Reynolds number. The differential rotation was varied from constant rotation,  $d\Omega/dR = 0$ , to the limit of stable Couette flow,  $\Omega \propto 1/R^2$ . However, the interaction of plumes and sheared flow was observed only for the intermediate case where the inner boundary rotates at  $\Omega_1 = \Omega_0 R_0/R_1$ . The

---

<sup>1</sup>Portions of this chapter were submitted to *Physics of Fluids*: Beckley, H.F., Colgate, S.A., Romero, V.D., and Ferrel, R., Rotation of a Pulsed Jet in a Rotating Annulus: A Source of Helicity for an  $\alpha\omega$  Dynamo, *Physics of Fluids*, Submitted, 2001.

fact that the properties of the  $\alpha$ -helicity produced by a driven jet and the  $\Omega$ -flow both occur naturally makes the  $\alpha\omega$  dynamo the likely explanation of astrophysical dynamos as well as feasible to demonstrate in the laboratory. The flow was visualized by pulsed hydrogen electrolysis from a tungsten wire and dispersed guanidine in water. The flow was imaged using a digital video camcorder operating at 30 Hz frame rate. This hydrodynamic flow visualization experiment is a precursor to the design and development of an experiment using liquid sodium to produce an  $\alpha\omega$  dynamo with positive gain in the laboratory. The experiment also simulates the  $\alpha\omega$  dynamo expected in astrophysical circumstances.

### 3.1 Introduction

This chapter describes the flow field necessary for producing a laboratory demonstration of the  $\alpha\omega$  dynamo. This chapter will describe and demonstrate the origin of the  $\alpha$ -*helicity*. This is the most puzzling aspect of dynamo flow, both in astrophysical objects and in the experiment. Another facet of discussion in this chapter will describe the Couette or  $\Omega$ -flow in the plume rotation experiment. The  $\Omega$ -flow simulates the differential rotation that occurs naturally in astrophysical bodies because of Keplerian rotation in accretion disks and meridional circulation in rotating stars. The  $\omega$ -deformation has the magnetohydrodynamic effect of differentially winding the radial component of a quadrupole magnetic field into a toroidal field.

This chapter starts with a discussion of convective plumes and then of their coherent properties, followed by their further coherence when formed in a rotating frame. Subsequently discussed will be the importance of these properties for making the  $\alpha\omega$  dynamo and then demonstrate experimentally this behavior of plumes in the laboratory.

#### 3.1.1 Convection, Turbulence, Helicity, and Dynamos

Convective plumes driven by buoyancy are evident in our environment, i.e. the typical smoke stack plume. Usually such plumes are approximately steady

state and diverge convectively to large radial dimensions. When the radial size is large compared to the size of the source, Morton, Taylor and Turner (MTT) (1956) described it as the point source approximation. Such plumes are explained by turbulent entrainment between the mixed plume material and the background uniform medium. Similarly convection in stellar atmospheres is also explained by turbulence, as in the Mixing Length Theory (MLT) by Böhm-Vitense (1958). Previously in dynamo theory a finite *helicity* must be extracted from the average of turbulent motions. However, the observation of a relatively coherent behavior of plumes as compared to the purely random motions of turbulence has led to the possibility of a new source of *helicity* for explaining the occurrence of the  $\alpha\omega$  dynamo in astrophysical objects. As will be discussed later, this flow property of *helicity* requires both an axial translation and a finite rotation of the flow relative to a rotating frame. In dynamos helicity serves the function of changing the field of one direction, toroidal, to an orthogonal one, poloidal. Helicity is defined as:

$$\alpha = \mathbf{v} \cdot (\nabla \times \mathbf{v}). \quad (3.1)$$

This is the  $\alpha$ -deformation of the  $\alpha\omega$  dynamo. The  $\omega$ -component is differential rotation,  $d\omega/dR < 0$ , typical of Keplerian flow in a gravitational field or Couette flow in the laboratory.

For a plume an axial translation is obvious, but the rotation of the plume flow relative to the frame is less so. When plumes are derived from finite buoyant elements as in the experiments of Sánchez et al. (1989), then the lack of turbulence and the coherent nature of the axial flow becomes evident. This coherence is not only the singular direction upward (downward) of the flow, but also the uniform radial divergence (convergence) of the flow. It is then evident that the moment of inertia of a buoyant element would increase (decrease). If either were to occur in a rotating frame, and if the friction between the expanding buoyant element and the background fluid is finite, then one would expect to see a differential rotation

between the expanding buoyant element and the background frame material as in conserved circulation (Pedlosky 1987). In geophysical fluid dynamics, the circulation is defined as the line integral of  $\mathbf{u}$  around the closed curve  $C$  as in  $\oint_C \mathbf{u} \cdot d\mathbf{r} = \Gamma$ . But  $\mathbf{u} \cdot \mathbf{r}$  defines specific angular momentum about an axis. They are equivalent when the axis is within  $C$ .

There is a significant difference between divergent and convergent flow. In divergent flow the vorticity decreases and so the differential rotation is bounded by that of the frame. In convergent flow, the vorticity can become nearly infinite. This is not useful for the dynamo as explained by Parker (1978) because then the total rotation of the plume becomes very large and the mean rotation angle averages to zero. Therefore this work is limited to the case of the diverging plume only. It was further recognized that in laboratory experiments this translation and rotation of a buoyant element could be approximated by a driven pulse of fluid. The pulse of fluid is driven by a transient, high pressure flow through an orifice as compared to the relatively lower velocities produced by convective forces. This then made possible a laboratory experiment demonstrating the  $\alpha\omega$  dynamo using liquid sodium (Colgate 1994). The two flows, the differential rotation of the  $\omega$ -flow and the helicity of the  $\alpha$ -flow, can be driven by high power and high pressure resulting in high velocities  $v$ , and consequently high magnetic Reynolds number,  $R_m = \frac{Lv}{\eta}$  in a conducting fluid of resistivity  $\eta$  and dimension  $L$ . A high magnetic Reynolds number,  $R_m > 100$ ,  $\alpha$ -helicity, and  $\omega$ -differential rotation of a conducting fluid are the conditions for creating a positive gain  $\alpha\omega$  dynamo. The purpose of this experiment is to demonstrate the helicity produced by transient, driven jets. We describe first some aspects of the theory to place these complicated requirements in the context of the experiment.

### 3.1.2 Plumes, Entrainment, & Mixing Length Theory

Figure 3.1 shows our image of a large buoyant element rising in a stratified stellar atmosphere (Colgate, Herant & Willet 2000). Initially the slow motion of the buoyant element is laminar, but then becomes turbulent at its boundary resulting in entrainment of the background fluid. As the density of the atmosphere decreases with height, the buoyant mass expands in order to achieve pressure equilibrium with the background. The rate of radial expansion may or may not exceed the rate of turbulent entrainment depending upon the ratio of the initial radius to the local pressure scale height. In Fig. 3.1(A) the plume rises in a stationary atmosphere and radially expands faster than the width of the turbulent entrainment zone. The same plume in Fig. 3.1(B) in a rotating atmosphere will rotate differentially, i.e. *untwist* relative to the frame. The confirmation of this prediction is the purpose of the experiment except that we create the divergent property of the plume by a pulsed jet in a constant, uniform density background. The two recognized theories of plumes and convection would not predict this result because the initial assumption in both cases is that the flow is dominated by uniform isotropic homogeneous turbulence either within the plume (MTT) or throughout the atmosphere (MLT).

### 3.1.3 Turbulent Plumes Originating from a Point Source

The original theory of turbulent plumes is due to MTT (1956) who studied systems in which buoyant material is ejected from a small, point-like source. The source is assumed to be steady state and the interior of the plume becomes turbulent. The MTT theory was based partly on the work of Schmidt (1941) who viewed the observed conical plumes as a balance between horizontal transport of heat and momentum and vertical convection. The most striking aspect of such a plume is the linear horizontal growth in width with vertical displacement.

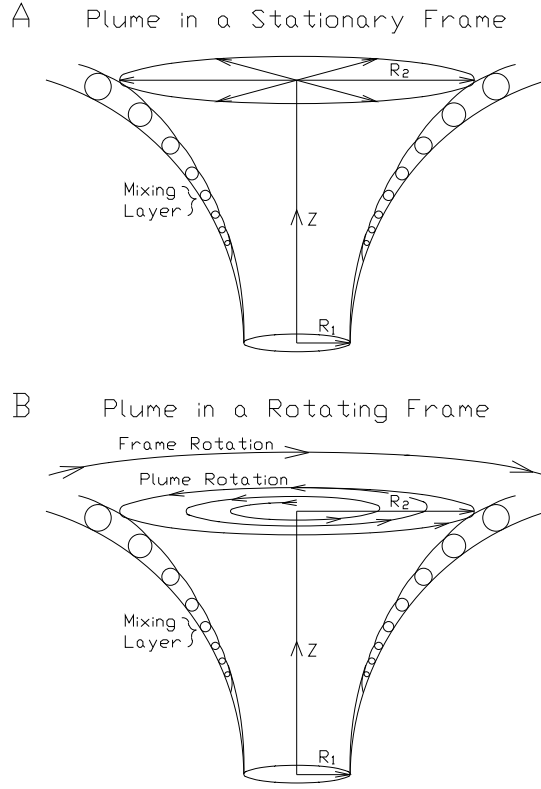


Figure 3.1: Figure 3.1(A) shows a plume rising and diverging in a stratified, stationary atmosphere with developing entrainment at the boundaries. Figure 3.1(B) shows the same plume in a stratified rotating atmosphere where the conservation of angular momentum or circulation causes a differential rotation of the plume relative to the frame.

Assuming the horizontal dependence of the fluid variables maintain a similar functional form along the plume, MTT derived a set of equations expressing the conservation of mass, vertical momentum and energy (buoyancy). In addition, the Boussinesq (1903) approximation and the entrainment hypothesis of Batchelor (1954) were integral parts of the theory. The latter assumption offers a way of explaining the linear growth and reducing the complicated turbulent behavior to a simple statement: The horizontal velocity of the boundary implies adding mass of undisturbed material to the flow proportional to the local vertical velocity. The constant of proportionality  $\Delta\phi \sim O(1/10)$  depends on the choice of horizontal

profile. An integration of the two velocities results in the concept of a fractional entrainment of undisturbed fluid per unit of vertical displacement. Figure 3.2 illustrates these two velocities under the assumption that the motion within the plume is dominated by a single large scale eddy or vortex where the inner boundary of the vortex rolls in contact with the axis going up and the outer boundary rolls against the stationary background. Then the vortex grows in radius by entraining the stationary fluid by a factor equal to its own radius per revolution of the vortex. This leads to  $\Delta\phi \simeq 1/2\pi$ . By way of comparison, if the outer boundary were equally turbulent as the plume rather than quiescent, we would expect each eddy to rotate and break-up in half a revolution rather than a full revolution.

In this picture the plume grows by entraining fluid from its surroundings. It does not grow by the radial divergent velocity of its individual fluid elements. This is evident by the stream lines added to Fig. 3.2. This is important for the applicability of these experiments, because we do not expect rotation of the fluid of the plume relative to its surroundings within the plume provided there is no radial divergence to the flow. On the other hand, the fluid at the head of the plume continuously diverges and is laminar before being entrained by the plume. The motion of this laminar fluid at the head of the plume is what should give rise to the helicity desired both in this experiment and in dynamo theory. Hence we consider only a short or transient pulse of buoyant fluid or jet. In convection in stars such large transient buoyant elements should occur naturally as in Fig. 3.1 at the base of the convection zone due to the large local gradient of the unstable buoyancy (Chandrasekhar 1961). The opposite view is mixing length theory where the convection is driven entirely by turbulence. We discuss this model next emphasizing the calculations that indicate a departure from this simple picture toward structures, and by inference, plumes.

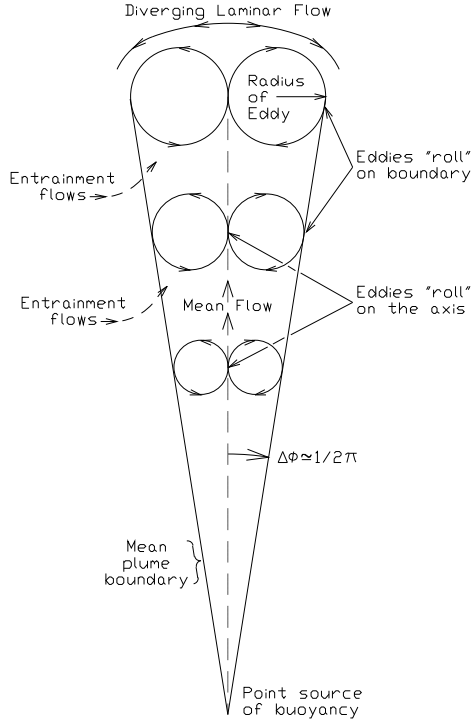


Figure 3.2: A schematic representation of a point-source MTT plume rising in a stationary uniform background fluid. The progressive entrainment is depicted as due to the friction of the outer boundary of the largest vortex that can fit within the flow. This friction then doubles the size of the vortex per revolution, resulting in the typical half angle  $\Delta\phi \simeq 1/2\pi$ . The stream lines of entrainment are shown as entering the plume flow at the outer boundary and therefore show negligible subsequent average radial divergence. However, before entrainment at the plume head the flow diverges rapidly. It is in this flow that we expect and measure the rotation that creates helicity.

### 3.1.4 Mixing Length Theory

The Mixing Length Theory (MLT) describes energy transport in a convective atmosphere as an ensemble of random eddies dominated by the largest size. MLT has been widely applied to astrophysical problems by Schmidt (1941), Taylor (1945), Prandtl (1952), and reached its canonical form in the work of Böhm - Vitense (1958). The simplicity of a diffusion-type process has made it popular in stellar evolution calculations with a notable lack of an alternative approach.



Numerical simulations by Chan and Sofia (1989, 1987) of convection in gravitationally stratified atmospheres have partially validated the mixing length concept. That is, the idea that convective elements move a finite distance before dispersing in the ambient medium. However, simulations also strongly suggest that the physical picture presented in MLT requires that convective flows develop on larger scales and be much less disordered than implied by MLT's reliance on turbulence for the mixing process. This conclusion persists even after taking into account the smoothing effect of intrinsic numerical viscosity. (For examples see Stein & Nordlund (1989), Cattaneo et al. (1991), Canuto, Goldman & Mazzitelli (1996), Hossain & Mullan (1993), Singh & Chan (1993), and Hurlburt et al. (1994).) Furthermore, the time dependence of the flow is both intermittent but persistent on longer time scales than one would expect from MLT. This is consistent with our view that local departures in the entropy contrast are initiated over large scales, comparable to the pressure scale height at the base of the convection zone, i.e. the initiation. They lead to the episodic formation of long lived buoyant structures. We call these structures *plumes*. However, in the present context our plumes are fundamentally different from the classical steady state turbulent plumes briefly described in the next section. We are furthermore interested in the rotation of these structures when they are formed in a rotating atmosphere. By considering the dynamics of individual plumes, it is possible to obtain a physical picture of the topology of velocity fields leading to the deformations that can create a dynamo effect.

### 3.1.5 Plume Formation

The most extensive experimental, analytic, and numerical modeling of the initial transient state of convective plumes has been undertaken by Sánchez et al. (1989). Special care was taken to launch buoyant elements from a static state in experiments of plume development in stratified and unstratified environ-

ments. These plumes and their environment were both incompressible fluids and so would not be expected to demonstrate the rapid radial divergence expected of compressible flow. But they did demonstrate the delay of several diameters of axial motion of the buoyant element before the onset of significant entrainment and before a state of self-similarity had been reached. The background fluid is described by a density increasing in depth for a down-going mass element so that the mass element ultimately encountered a density barrier.

The most striking aspect of the initial development of plume structure was the formation of a single large vortex ring presumably because their initial buoyant element was finite, one diameter in size and was initiated at low Reynolds number. In our experiments we use a short pulsed jet, which produces the same large single vortex, Fig. 3.3, but at sufficient velocity that the boundaries are turbulent. The initial motion of the resulting vortex is coherent similar to the diverging plume in a stratified atmosphere. After a delay, the vortex entrains surrounding matter and decays and expands in radius at the same rate as an entraining plume. We depend upon this same delay in entrainment for our radial plume model, but where we expect radial expansion to occur well before entrainment. Here we simulate this expansion behavior by the radially divergent motion in front of the vortex, induced by the pulsed jet, not by the expansion to pressure equilibrium in a stratified (gaseous) atmosphere.

Although analytic and numerical modeling of convective plumes has received considerable attention in the meteorological and engineering literature, comparatively few applications have been sought in astrophysical contexts. Notable exceptions are Moore (1967), Scalo & Ulrich (1973), Ulrich (1970a, 1970b, 1970c), Schmitt, Rosner & Bohn (1984), Rieutord & Zahn (1995), Lo & Schatzman (1997), and Zahn (2000).

The organization of the remainder of the paper is as follows: In Sec. 3.2

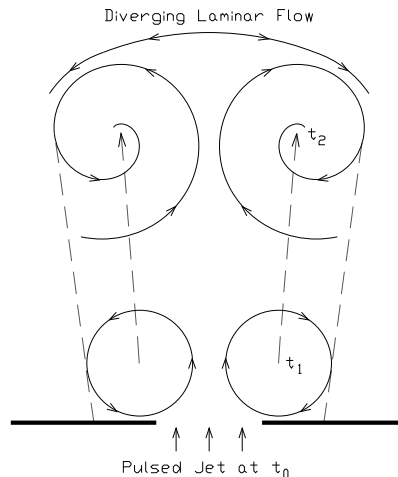


Figure 3.3: Figure 3.3 shows a schematic of the pulsed jet plume. A vortex ring is formed at  $t_0$  like a smoke ring and translates and expands at times  $t_1$  and  $t_2$  until it either dissipates or strikes a boundary.

the plume rotation and its relevance to dynamo theory is discussed. Section 3.3 describes the experimental apparatus and the flow visualization methods used in the experiment. The results of the experiment are discussed in Sec. 3.4 with a conclusion in Sec. 3.5. In Sec. 3.6 are discussions of a geophysical and an astrophysical example of plume rotation in rotating stratified atmospheres.

## 3.2 Plume Rotation and the $\alpha\omega$ Dynamo

### 3.2.1 Plume Rotation

When the background fluid or frame rotates, the expected rotation of the plume is an *untwisting*, or counter-rotation relative to a rotating frame. It occurs because of the transient conservation of angular momentum of the flow *ahead* of the plume (rather than the plume itself) as it expands radially, relative to its own axis. The expansion leads to an increase in moment of inertia of

$$I_{plume} = I_0 (r_{plume}/r_{port})^2, \quad (3.2)$$

where  $r_{port}$  is the initial radius of the plume as it exits the port in the experiment. Therefore, following such an expansion the rotation rate of the plume,  $\omega_{plume}$  relative to the rotation of the frame,  $\Omega_0$  becomes

$$\Omega_0 - \omega_{plume} = \Omega_0(1 - (r_{port}/r_{plume})^2) \quad (3.3)$$

The objective of the experiment is to observe and measure this rotation, or equivalently, the conservation of circulation (Pedlosky 1987).

### 3.2.2 Plume Rotation Damping

Turbulent entrainment of the material at the head of the plume with its surroundings ensures a relatively rapid damping of the differential rotation between this plume material and the background flow. One of the purposes of these experiments was to observe the extent of damping at a relatively high Reynolds number,  $Re \sim 10^5$ . One notes that for  $Re > 10^5$ , the turbulent drag coefficient (AIP Handbook, 3rd Ed. 1972),  $C_D \sim 2 \times 10^{-3}$ , is relatively independent ( $\times 2$ ) for  $10^5 \leq Re \leq 10^9$ . In the Liquid Sodium Dynamo experiment we expect  $Re \sim 10^7$ . We expected and have shown in these experiments that the turbulent entrainment does not destroy the coherence of the twist of the plume. However, simulations in 3D of such high  $Re$  are still beyond the current computational capability. This damping is to be compared to that of a geostrophic or cyclonic vortex where the radial pressure gradient is reversed and conserved angular momentum flow stabilizes the Helmholtz instability, and hence, entrainment at the boundary. The resulting many turns of the cyclonic vortex greatly reduces its effectiveness for generating helicity in the  $\alpha\omega$  dynamo. This is because the many turns of cyclonic flow averages the vector of the rotated magnetic flux. One desires instead that the differential rotation between the plume and the background flow be limited to  $\pi$  radians where  $\pi/2$  is optimal (Ferrière 1994).

### 3.2.3 Plumes in a Rotating Frame: The Origin of Dynamo Helicity

A fundamental and previously puzzling aspect of convectively driven dynamo theory has been the origin of the *helicity* required in the  $\alpha\omega$  dynamo to transform a toroidal field, initially amplified by differential rotation, back into poloidal field. The helicity described by Eq. 3.1 requires both axial and rotational motion. If both motions are axially symmetric, then by Cowling's (1934) theorem (see also Parker 1978) the dynamo generated field must be non-axisymmetric. The variability of the magnetic field associated with such an off-axis field is difficult to reconcile with astrophysical circumstances. Hence, one looks for a non-axisymmetric  $\alpha$ -effect so that a near-axisymmetric field can be generated. Off-axis plumes uniquely satisfy this requirement because they can be convectively driven in the case of stars and even more robustly driven by collisions of stars with the accretion disk (Colgate & Li 1999, 1997, Pariev, Colgate & Finn 2000). (A discussion of Cowling's (1934) theorem is beyond the scope of this paper, but it is fundamental to dynamo theory.)

### 3.2.4 The $\alpha\omega$ Dynamo

For completeness, we briefly describe how the  $\alpha\omega$  dynamo works to place the plume-derived helicity in context (Parker 1978). We use as an example the dynamo that we predict forms in the accretion disk around the central massive black hole of every galaxy. The central black hole is formed by mass flow through this accretion disk. The circumstance of this particular astrophysical dynamo avoids the complexities and uncertainties of the formation of plumes in stellar atmospheres. In this dynamo the plumes creating the helicity are driven by a small fraction of the accreting mass in the form of stars. These stars periodically collide with or plunge through the low mass (thickness) disk many times. Thus these star-disk collisions and the plumes they form make the simplest astrophysical

dynamo to visualize, and plausibly the largest dynamos in the universe. The resulting dynamo mechanism is shown schematically in Fig. 3.4. These same large-scale plumes driven by convection in a star with internal differential rotation should similarly produce a dynamo.

Figure 3.4(A) shows an initial quadrupole magnetic field within a conducting accretion disk. Figure 3.4(B) shows how differential rotation within the conducting accretion disk wraps the radial component of the quadrupole field into a much stronger toroidal field. The differential rotation is derived from the Keplerian rotation of the accretion disk around a central mass. This is the  $\omega$ -deformation. A plume driven by a star-disk collision carries a fraction of this now multiplied toroidal flux above the surface of the disk, Fig. 3.4(C). Figure 3.4(D) shows that as the plume expands into the near vacuum away from the disk, differential rotation of the plume matter takes place. This rotation carries and twists (counter-rotates) the loop of toroidal flux,  $\sim \pi/2$  radians, into the orthogonal, poloidal plane. This is the  $\alpha$ -deformation, or *helicity* of the dynamo process. Reconnection allows this loop of flux to merge with the original quadrupole flux, thereby augmenting the initial quadrupole field. For positive dynamo gain, the rate of adding these increments of poloidal flux must exceed the negative quadrupole resistive decay rate.

### 3.2.5 Consequences of Plume Helicity

The consequence of this complicated sequence of motions (i.e. axial displacement, differential rotation, rapid damping of rotation, and in most cases rapid internal turbulent diffusion) is the creation of the *ideal circumstance for the  $\alpha\omega$  dynamo to reach high gain in both astrophysical circumstances and in the laboratory*. A robust dynamo has long been sought in both theory and experiment, but has eluded very many attempts of proof (e.g. Roberts & Soward 1992). Recently Raedler (1998) and Gailitis (2000) have announced positive gain in laboratory sodium dynamos. These dynamos are of the pure helicity, or  $\alpha^2$  type where the

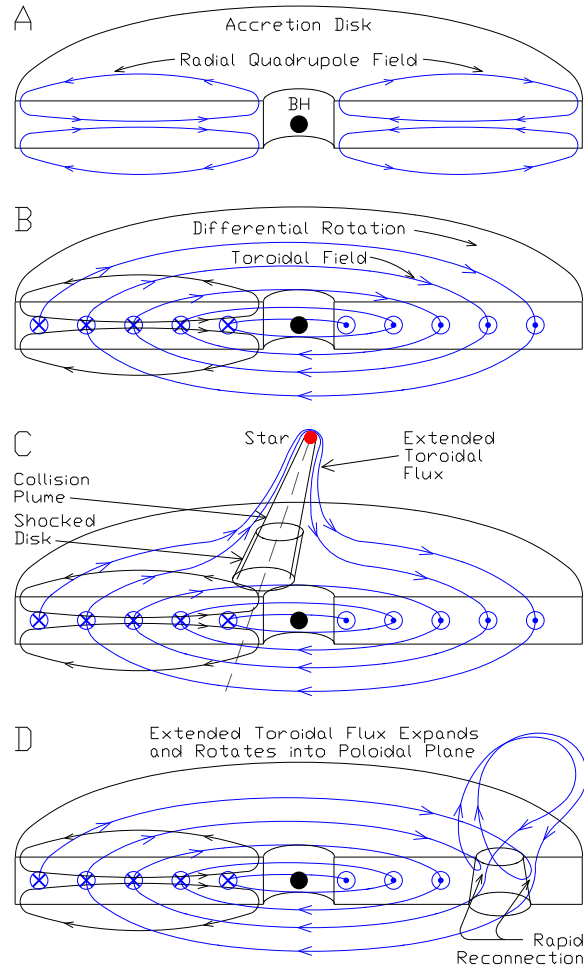


Figure 3.4: The  $\alpha\omega$  dynamo in a galactic black hole accretion disk. A: Initial poloidal quadrupole field. B: Poloidal field wrapped into a stronger toroidal field by differential rotation. C: A star-disk collision extends the toroidal flux above the disk. D: The extended toroidal flux expands and rotates into the poloidal plane and reconnects at the base of the deformation. The loop of expanded flux external to the disk now has the same orientation of magnetic polarity as the original poloidal field, but the loop is external to the disk. Reconnection allows this loop of flux to merge with and augment the original loop of quadrupole field.

helical flow is driven by multiple shaped vanes. An astrophysical dynamo must be much less constrained, it must result from flows occurring naturally without ridged materials.

Most flows in astrophysics as well as the sodium dynamo experiment that

might produce a dynamo, with the exception of the earth's dynamo, occur at very high Reynolds number. The resulting turbulence, especially for the helicity derived from plumes, raises some question concerning damping or perhaps negating the helicity altogether. A consequence of this is the difficulty of numerical modeling of the flow at high fluid Reynolds number necessary to exhibit these motions in 3-D with turbulence. We estimate that in order to demonstrate convincingly the average rotation within the turbulent flow of the plume, that the smallest eddy scale should be no greater than 1/10 the radius of the plume. Hence, with a scale ratio of plume to major radius of an addition factor of 10,  $Re > 10^4$  are necessary for meaningful calculations. Such a high  $Re$  is only now an emerging possibility on the largest parallel computers. As a consequence an experiment was the most feasible way to convincingly demonstrate these plume properties that might later be incorporated into dynamo calculations and dynamo experiments. The crucial point for the laboratory generation of helicity by plumes is that they can be closely simulated by driven pulsed jets where the velocity of the driven jet is comparable to the velocity of rotation. Such pulsed jets using hydraulic pressures of 100 atm will have a velocity of  $10^4$  cm/s compared to a few cm/s for thermal convection driven plumes. It is this large difference that makes a laboratory scale liquid sodium  $\alpha \omega$  Dynamo experiment feasible.

### 3.2.6 Plume Turbulence

The internal turbulence inherent to plume entrainment further aids in the effectiveness of such plumes for dynamo gain. After entraining and rotating toroidal flux to the poloidal plain, it is imperative for dynamo gain that this poloidal flux merges with the original poloidal flux and therefore be released from the plume itself. The strong driven turbulence in the plume enhances the diffusive release and merging of this flux. In other words, one desires a large magnetic Reynolds number for the differential rotation creating the toroidal field, but a



relatively low magnetic Reynolds number for the helicity generating plume deformation.

### 3.2.7 Plume Characteristics

We review the four types of plumes that we believe are simulated by the experiment. The first is the buoyancy driven plume in a stratified atmosphere where the size of the initial buoyant element is comparable to the local pressure scale height. This plume is important to stellar dynamos where the initial buoyant element and the consequential maximum magnetic stress is determined by conditions at the base of the convective zone (Colgate 1978). The convective stress then predicts the limiting strength of solar fields. The second type of plume is a shock driven plume expanding supersonically into a near vacuum. This is the plume that we believe is driven by stellar collisions with the accretion disk. Similarly supernovae will produce such plumes within the galaxy. These plumes are robust in the sense that their dynamic stress is greater than the stress of the differential rotation of the fluid. The third type of plume is the one created in the experiment by a pulsed jet where the time duration of the jet is of the order the traversal time of the diameter of the buoyant element. This produces a plume or vortex ring. The fourth type of plume is the near-steady-state point-source buoyant plume that was discussed earlier. It is typical of convection in a uniform atmosphere. We are not sure in what circumstance such a steady state plume would lead to an astrophysical dynamo because of the inherent stochastic nature of divergent and convergent flows. The negative contribution to the helicity by these convergent flows is demonstrated in the experiment.

Recently Fernando, Chen & Ayotte (1998) have studied buoyancy-driven plumes in a rotating frame, but where the axis of the plume was axially aligned with that of rotation. Under these circumstances no off-axis helicity is generated, but the change in rotation and the modification of convection was observed. Similarly,

Lavelle (1997) studied plumes with rotation and shear from the standpoint of modifying the entrainment. However, both for the liquid sodium experiment and in order to substantiate the astrophysical dynamos we feel we must demonstrate the helicity produced by the off-axis, driven plume.

### 3.3 The Experiment

The Plume Rotation Experiment (PRX) consists of two coaxial, separately rotating, Plexiglas<sup>TM</sup> cylinders having radii  $R_0=15$  cm and  $R_1=7.5$  cm. The radial width of the annular test space is therefore 7.5 cm. The height of the annular test space is the region bounded below by the plume port plate and above by a transparent plastic window, the witness plate, so called because it allows one to view the rising plume through an optically flat surface. For the small port discussed below, this height was 12.5 cm and for the large port it was 10 cm. The apparatus was rotated at 1/2 Hz (revolutions/s). This results in a peripheral fluid velocity of  $\sim 50$  cm/s. The plumes were injected with a velocity of  $\sim 10$  cm/s. Consequently,  $Re \simeq 10^5$  for the  $\Omega_{\text{differential}}$  flow and  $Re \simeq 10^4$  for the plumes. We designed the experiment to have the largest  $Re$  feasible in order to simulate turbulent effects, but also designed for the ease of video recording at 30 Hz. These modest velocities resulted in negligible centrifugal and plume drive pressures. This is in contrast to the liquid sodium experiment where these pressures approach the engineering limit of materials.

Two different diameters of plume ports were used. The small port diameter,  $d_{SP}=3.3$  cm, was chosen such that the entraining plume would not interact with the cylinder walls prior to impinging upon the witness plate. This allowed the plume to fully develop by entrainment and radial divergence independent of wall interference. The large port diameter,  $d_{LP}=4.8$  cm, was chosen such that when the plume impinged on the witness plate, its diameter equaled the width of the annulus.  $d_{LP}$  was the maximum size possible that would allow an entraining



Figure 3.5: The Plume Rotation Experiment apparatus with its camera mounts, electrical communications, air supply, and the cylinder drive systems.

plume to rise symmetrically through the annular space, impinge on the witness plate, and rotate. Since the PRX was designed to simulate the flow fields that we believe are requisite for the sodium dynamo, the plume produced by  $d_{LP}$  would then maximize the magnetic flux displaced and rotated by the plume. Figure 3.5 shows the PRX with its rotational axis vertical so that the free surface of the fluid is axisymmetric. Figure 3.6 is a schematic of the PRX. The plume is driven by a pulse of air exerting pressure on the water within the inner cylinder. The water is then forced out through radial ports at the base of the inner cylinder into the plenum and then through a plume port orifice as a pulsed jet. At the termination of the pressure pulse, gravity forces the water, now at different heights in the annular and inner cylinder volumes, to return through the same ports, reaching equilibrium in a few seconds.

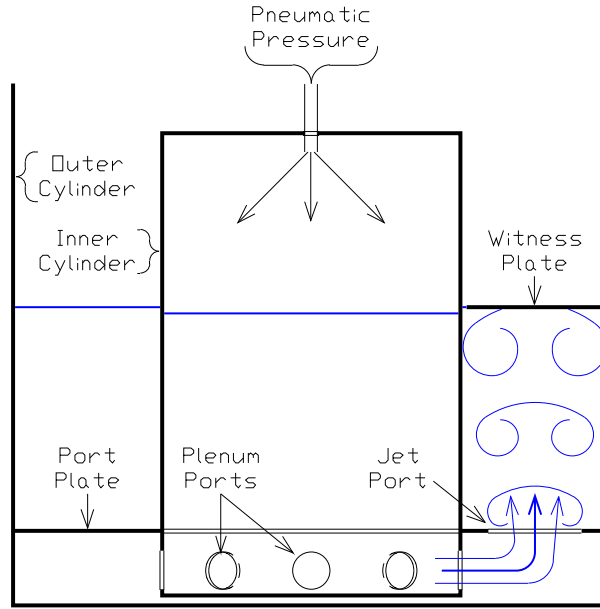


Figure 3.6: Plume Rotation Experiment schematic. An air pressure pulse forces a pulse of water out of the inner cylinder, through the plenum ports and then through the plume port. This forms a rising vortex ring that simulates an expanding plume. The inner and outer cylinder can be rotated together and separately. The plume can be observed from the side and top.

### 3.3.1 Apparatus

The PRX apparatus consists of five assemblies: 1) inner cylinder assembly, 2) outer cylinder assembly, 3) camera mounts, 4) electrical communications and air supply, 5) cylinder drive systems.

The inner cylinder assembly consists of a seal and bearing assembly for the air supply pressure manifold, plenum ports, and a rotating seal. The air supply pressure manifold is a 14 mm i.d. tube that extends into the inner cylinder, and does not rotate with the apparatus. A tube connects the supply manifold to a pressure transducer that measures the pressure of the air applied on the fluid within the inner cylinder. The plenum ports permit the flow of fluid out of the inner cylinder into the annular region beneath the port plate. The fluid seal prevents the flow of fluid through the narrow annular space between the inside

edge of the port plate and the outside of the inner cylinder.

The outer cylinder assembly consists of the port plate and the hydrogen electrolysis anode and cathode. The electrolysis cathode is a 50  $\mu\text{m}$  tungsten wire stretched across the plume port on top of the port plate for the large port and at 2.5 cm above the port for the small port. The distance that the plume travels from the wire to the witness plate was therefore 10 cm in either case. The wire is centered across the plume port and is tangent to a circle about the cylinder's axis. The electrolysis anode is a 2 mm copper wire in the annular space beneath the port plate. The outer cylinder also provides mechanical support for the camera mounts.

There are two camera mounts for the apparatus. The upper mount is a tripod attached to the outer cylinder on which the digital video (DV) camcorder is attached for the vertical (i.e. axially aligned) view. The lower mount is a horizontal platform attached to the outer cylinder, which has an extension for the DV camcorder. It is used for the horizontal (i.e. radially aligned) view.

Electrical communication to and from the rotating apparatus takes place through a 6-channel slip-ring assembly. One pair of channels is used for a video link. 12 VDC for illumination is transmitted through the second pair of channels. The last pair of channels carries the pulsed DC power for hydrogen electrolysis.

The drive system consists of two 90 VDC, 1/27 Hp independent variable speed motors through a multi-stage belt drive. Each cylinder rotates in the clockwise direction as viewed from the top.

### 3.3.2 Subsystems

There are five additional, stationary subsystems of the apparatus: 1) electrical delay circuits for pneumatic and electrolysis timing, 2) constant-pressure air supply, 3) pressure transducer and digital oscilloscope for measuring pressures,

4) DC power supply for hydrogen electrolysis, 5) TV and VHS/VCR system for real-time viewing and secondary image recording.

A pressure transducer output was recorded by a digital oscilloscope and used in conjunction with the low-pressure regulator. A DC voltage supply, 200-400 volts, was used to supply pulsed voltage, of 0.1 and 0.5 second duration, for the hydrogen electrolysis. The short pulse produced a thin sheet,  $\sim 1$  cm in height, of bubbles emitted from aqueous  $\text{Na}_2\text{SO}_4$  solution at the tungsten wire. The long pulse allows a wider range,  $\sim 5$  cm, of plume length to be monitored. The short pulse could be delayed for the same purpose, but in practice, the long pulse best demonstrated the integral behavior of the plume.

A TV and VHS/VCR system for real-time viewing and secondary image recording was used in conjunction with the DV camcorder. The camcorder records a digital image internally, and in addition, the analog output of the DV camcorder was transmitted via the slip rings and a coax cable to a real-time viewing monitor. This system permitted convenient, single-frame replay capability of the studio-quality VHS/VCR and allowed for quantitative analysis of individual plumes.

### 3.3.3 Flow Visualization Methods

Two flow visualization methods were employed in the experiment: pulsed hydrogen electrolysis from a tungsten wire in an aqueous  $\text{Na}_2\text{SO}_4$  solution (Merzkirch 1987) and dispersed guanidine<sup>2</sup> in water. Hydrogen electrolysis creates a thin sheet of  $\sim 50$   $\mu\text{m}$  diameter bubbles. The bubbles emanate from the aqueous  $\text{Na}_2\text{SO}_4$  solution at a  $50$   $\mu\text{m}$  tungsten wire due to pulsed electrolysis. The relative delay

---

<sup>2</sup>Guanidine is a crystalline compound that is formed by the oxidation of guanine. Guanine is a white amorphous substance found in the scales of certain fishes, the guano of sea-birds, and the liver and pancreas of mammals. Another use of the label guanine is that of one of the five nucleotide bases of nucleic acids. The guanidine used in the PRX is derived from fish scales and found under the name of Mearlmaid. The guanine crystals are basically planar with a linear dimension on the surface of  $\sim 1\mu\text{m}$ . The guanidine concentration used was  $\sim 5$  parts in  $10^5$ .

between the plume initiation and the electrolysis pulse allowed for the observation of different plume regions. Hydrogen electrolysis was used primarily to reveal the average behavior of the near laminar flow at the head of the plume. The pattern of these small bubbles that outlines the plume is rapidly lost in the turbulence within the plume. On the other hand, guanidine, a pearlescent material of micron-size platelets, produces an image of the entire plume. The modulation of this image emphasizes the the largest shear in the flow. Since this largest shear occurs primarily at the boundary of the eddies, guanidine outlines the turbulence within the plume and thus it outlines the entrainment boundary of the plume. In addition, it shows the turbulence as the plume strikes the witness plate. The hydrogen bubbles are even more random in pattern in this region. Yet the guanidine images show the further, average differential rotation of the turbulent fluid.

Both methods reveal a coherent counter-rotation of the flow, either within the laminar flow ahead of the rising plume, or in the turbulent divergent flow when the plume strikes the witness plate. The linear array of bubbles produced by the wire remains clearly a line during rotation of the plume when it is embedded in the near-laminar flow at the head of the plume. We will show in forthcoming images the clear sequential rotation of the line of bubbles. In contrast, when the plume strikes the witness plate only the guanidine shows the average behavior of the flow. The average rotation of the turbulence can readily be discerned from an animated sequence.

These two different measurements are important to the sodium dynamo experiment because: The toroidal magnetic flux will be lifted ahead of the plume and will be rotated by a large, but finite angle. The flux embedded in the turbulent plume will also be lifted and rotated coherently upon striking the end wall.

### 3.4 Results

#### 3.4.1 The Rising Plume

Figures 3.7 and 3.8 show the development of rising plumes in static fluid fields. Since the plume pulse is relatively short in time, this produces a single large-scale vortex ring (as in Sánchez et al. 1989). The outermost radius of the vortex ring diverges similarly to the outline of a standard point-source entrainment plume (Morton et al. 1956). In Fig. 3.7 the relatively smooth laminar flow at the head of this vortex ring is evident in the trajectory of the bubble tracers released ahead of it. Figure 3.8 shows the same plume rising at the same times as Fig. 3.7, but in guanidine. In contrast to Fig. 3.7, Fig. 3.8 shows the internal turbulent behavior. Animated sequences show the complete development of the rising plumes shown in Figs. 3.7 and 3.8. One notes that no turbulence is evident in Fig. 3.8(A), compared to the large displacement of the laminar field in Fig. 3.7(A). This is to be compared to the idealized pulsed plume of Fig. 3.3.

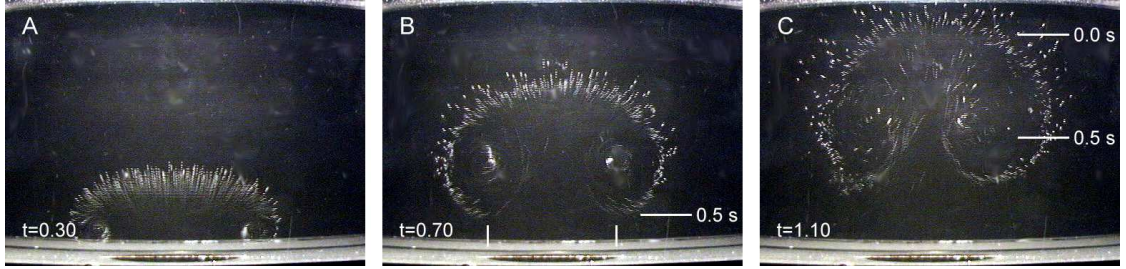


Figure 3.7: Side view showing the laminar flow ahead of the plume in an  $\Omega=0$  static fluid field with a hydrogen electrolysis pulse of 0.1 s duration. The plume velocity is 8.3 cm/s, therefore the height of the sheet of bubbles is  $\sim 0.8$  cm. The large-port diameter of 4.8 cm is delineated in image (B) by the vertical white lines. The 0.5 s line in image (B) shows the equivalent position of the delayed electrolysis pulse exhibited in Fig. 3.14. The 0.0 s and 0.5 s lines in image (C) show the equivalent extent of the extended electrolysis pulse exhibited in Fig. 3.15, where the sheet of bubbles is  $\sim 4.2$  cm in height.



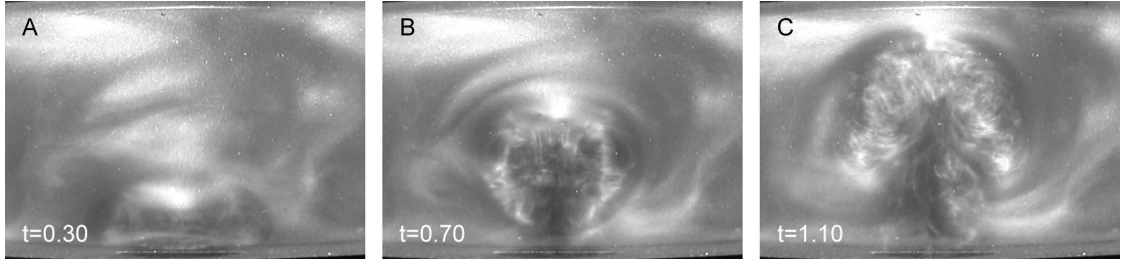


Figure 3.8: Side view of a rising plume showing turbulent entrainment in an  $\Omega=0$  static fluid field with guanidine. The plume has not yet reached the steady state condition of half-angle  $\phi \simeq 1/2\pi$ . The delay in the onset of turbulence is evident between images (A) and (B) as compared to images 3.7(A) and 3.7(B).

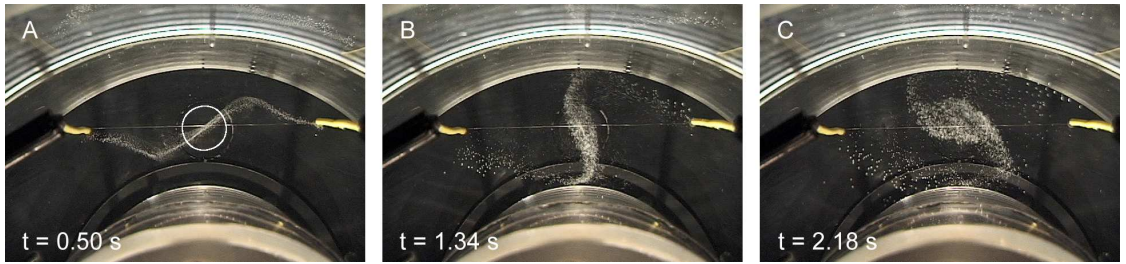


Figure 3.9: Top view showing plume rotation in an  $\Omega = \text{const}$  fluid flow field with 3.3 cm port. The port is outlined in image (A) by white circle.  $v_{R_0} = 48$  cm/s,  $v_{\text{plume},SP} = 7.5$  cm/s. Frame rotation is clockwise.

### 3.4.2 The Rotating Plume

Figures 3.9 and 3.10 show the rotation of the laminar fluid ahead of the plume produced from the small and large ports respectively in  $\Omega = \text{const}$  fluid. Figure 3.11 shows a schematic of the rotation measurements. The vertical position and change in angle of the line of bubble tracers in Fig. 3.10 relative to the solid-body rotation of the reference frame is shown schematically in Fig. 3.11. The top view, Fig. 3.11(B) correlates the angle of rotation with the times and plume size of Fig. 3.10.

Figure 3.12 shows the rotation of the large port plume when striking the witness plate as observed with guanidine. Without animation the rotation is barely discernible, but an animated sequence gives the clear impression of the

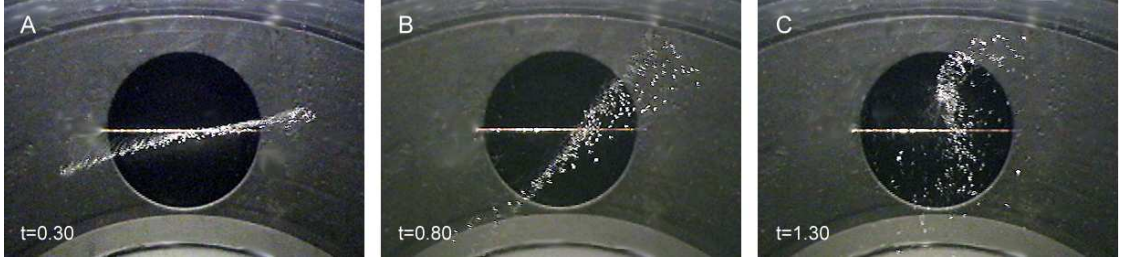


Figure 3.10: Top view shows plume rotation in an  $\Omega = \text{const}$  fluid flow field with 4.8 cm port.  $v_{R_0} = 48 \text{ cm/s}$ ,  $v_{\text{plume},LP} = 8.3 \text{ cm/s}$ . Frame rotation is clockwise.

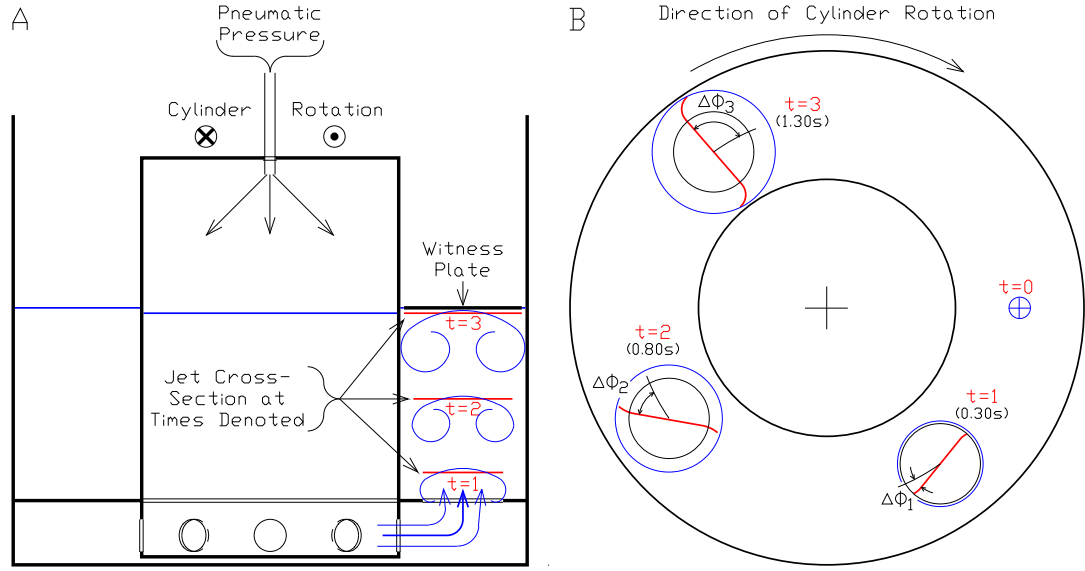


Figure 3.11: The schematic side and top views of Fig. 3.11 show respectively the plume divergence and rotation in an  $\Omega = \text{const}$  rotating frame. A plume is injected into the rotating annulus of water from the port by a pulse of air above the water surface interior to the inner cylinder. As the plume rises, it expands and rotates relative to the surrounding fluid. The parenthetical times denoted in the top view coincide with the times and views shown in the images in Fig. 3.10.

further differential rotation of the turbulent flow at the witness plate following the non-turbulent flow at the head of the plume.

The plume rotation angle data versus the reference frame rotation angle are plotted quantitatively in Fig. 3.13 for both port sizes. The data are from Figs. 3.9, 3.10, and 3.16. Plume rotation angles were measured from every third

image in each 30 Hz series.

In Fig. 3.13, the solid line of  $slope = -1$  represents the maximum possible relative rotation angle in an  $\Omega = const$  fluid flow. This limiting case is where the plume assumes infinite expansion and completely decouples from the rotating reference frame. In this limiting case, with respect to the laboratory reference frame,  $\Delta\omega_{plume} = 0$ .

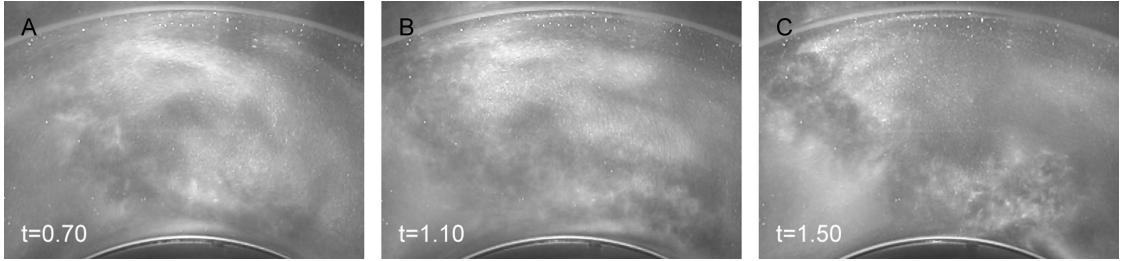


Figure 3.12: Rotation of the large port plume when striking the witness plate as observed with guanidine. Without animation the rotation is barely discernible, but an animated sequence gives the clear impression of the further differential rotation of the turbulent flow at the witness plate following the non-turbulent flow at the head of the plume (Fig. 3.7).

We calculate the expected differential rotation angle  $\Delta\theta_{plume}$  for each of the port sizes using the average measured vertical plume velocities measured from from Figs. 3.9 and 3.10. We assume a radial divergence equal to the entrainment half-angle of  $= 1/2\pi$  as if the laminar flow ahead of the plume diverges at the same rate as would an ideal entrainment plume. The vertical plume velocities remain near constant at 7.5 and 8.3 cm/s for the small and large ports respectively. The approximation for the plume radius is then

$$r_{plume} = r_{port} + (v_{plume}t/2\pi) \quad (3.4)$$

where time  $t$  is measured from when the plume emerges from the port at  $t_0$ . Figure 3.13 also shows the time when the plumes impinge on the witness plate at  $t_{impinge}$  beyond which the radius of Eq. 3.4 no longer applies. We derive the differential

rotation angle,  $\Delta\phi$ , by substituting Eq. 3.4 into Eq. 3.3 for  $r_{plume}$ . By integrating over the plume lifetime from  $t = 0$  to  $t$  we obtain the expected differential rotation angle, measured in radians, as

$$\Delta\phi = \Omega_0 \int_0^t (1 - (r_{port}/r_{plume})^2) dt = \frac{\Omega_0 t^2}{\tau + t} \quad (3.5)$$

where

$$\tau = \frac{2\pi r_{port}}{v_{plume}} \quad (3.6)$$

For  $\Omega_0 = 2\pi \times 1/2 Hz = \pi$  rad/s one has for the small port  $\Omega_0 \tau_{SP} = 4.34$  rad, and for the large port  $\Omega_0 \tau_{LP} = 5.71$  rad. Thus one notes that the frame rotates nearly a full revolution during the rise of the plume.

Figure 3.13 shows the results of the theoretical differential rotation angle, Eq. 3.5, and the measurements of plume differential rotation. The data points are connected by a curve for visual reference. The theoretical curves are shown dash-dot for the small port with the higher rotation rate and long-dash for the large port, slower rotation. We have also plotted a solid straight line as an upper bound on plume rotation where a stationary plume rotates at  $\Omega_0$  relative to the frame. One notes that the actual differential plume rotation is slightly faster than the theory indicating a plume expansion angle slightly greater than the classic plume entrainment half-angle of  $1/2\pi$  and so a slightly greater differential rotation is expected than the ideal of Eq. 3.5.

We expect the drag to become larger due to the enhanced turbulence when the plume strikes the witness plate. The curvature at the upper end of the experimental curves after striking the witness plate is consistent with this explanation. Note the longer time for the small plume to strike the witness plate because of both the slower velocity and the larger distance from the port to the witness plate: 12.5 cm rather than 10 cm. We have also included the data from the differential frame rotation case or partial Couette flow measurements of Fig. 3.16. Here

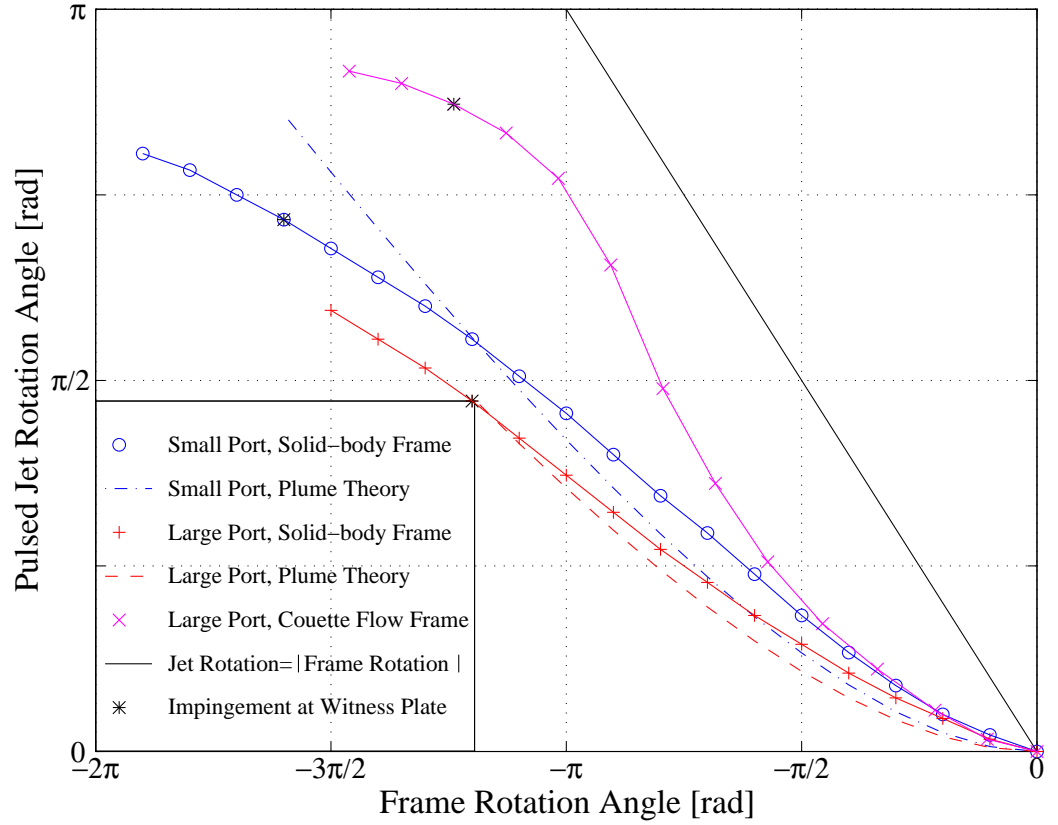


Figure 3.13: Figure 3.13 shows the data for the differential rotation of plumes driven from the small port, "o" points and large port, "+" points. Since the differential angle is negative relative to the rotation of the frame, a positive differential angle corresponds to a negative frame angle. The reference frame for two cases is solid-body rotation. The third data are from the  $\Omega_{\text{differential}}$  flow similar to  $\Omega \propto 1/R$ . The data are derived from the images in Figs. 3.9, 3.10, and 3.16. The magnitude of the measurement error in plume rotation angle is comparable with the size of the data points. The origin is where the plume pulse and the electrolysis pulse coincide. The two theoretical curves are from Eq. 3.5 with the dash-dot using the small port parameters and the long-dash curve using the large port parameters.  $v_{R0} = 48 \text{ cm/s}$ ,  $v_{\text{plume},SP}(\Omega = \text{const}) = 7.5 \text{ cm/s}$ ,  $v_{\text{plume},LP}(\Omega = \text{const}) = 8.3 \text{ cm/s}$ ,  $v_{\text{plume},LP}(\Omega_{\text{differential}}) = 8.2 \text{ cm/s}$ .

the differential rotation angle of the plume is measured ( $+\pi/2$  radians) relative to the radial from the axis to the center of mass of the bubbles outlining the plume. This shift accounts for the shift of the camera axis relative to the plume because

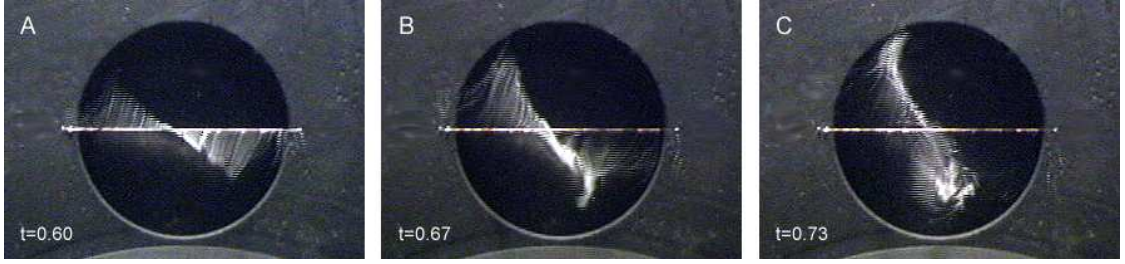


Figure 3.14: Delayed electrolysis pulse shows that the base of the plume is co-rotating with the reference frame. This is due to the convergent flow at the base of the plume. The electrolysis pulse was delayed from the plume pulse by 0.5 s, and the duration of electrolysis pulse was 0.1 s. Frame rotation is clockwise.

of the differential frame rotation. We also note the greater rotation rate of the plume relative to the  $\Omega = \text{const}$  case presumably because of entrainment. Before discussing the differential frame case, we consider the rotation within the plume as compared to the rotation of matter pushed ahead of the plume.

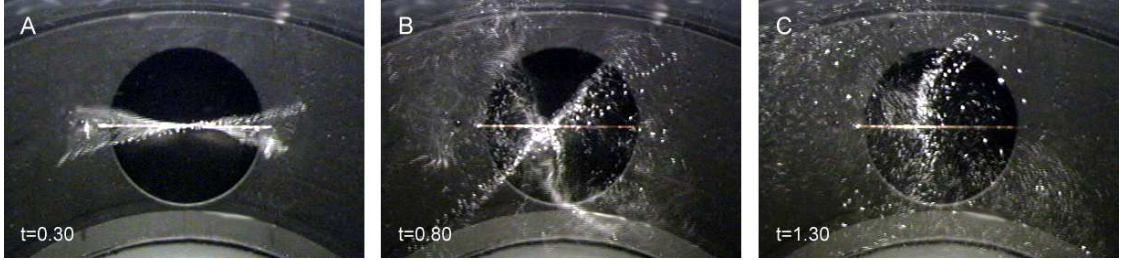


Figure 3.15: Extended electrolysis pulse showing an overlay of the counter-rotation of the plume head and the co-rotation of the plume base. Note that the co-rotation of the plume base loses its initial coherence through turbulent entrainment. The times denoted in each of the images intentionally coincide with those of Fig. 3.10. The duration of electrolysis pulse was 0.5 s. Frame rotation is clockwise.

### 3.4.3 Convergent Flow

We next consider the convergent flow behind the vortex ring forming the head of the plume. This convergent-flow is most clearly evident in Fig. 3.7(C). We expect that this convergent-flow, as compared to the divergent-flow at the head of the plume, will lead to co-rotation of the plume, opposite to the counter-rotation observed in Figs. 3.9 and 3.10. In order to show how the convergent-flow

affects the plume rotation we have used a delayed pulse of electrolysis (0.5 s delay, 0.1 s duration), as well as an extended electrolysis pulse (0.5 s duration). The extended electrolysis pulse superposes the convergent-flow co-rotation beneath the divergent-flow counter-rotation. The equivalent timing of these delayed and extended electrolysis pulses relative to the vertical plume motion are shown in Figs. 3.7(B) and 3.7(C) respectively. Both the delayed and extended pulses demonstrate the expected co-rotation of the convergent-flow behind the vortex ring as being opposite to the counter-rotation of the divergent flow ahead of the pulsed plume. The delayed pulse, Fig. 3.14 shows that the base of the plume is co-rotating with the reference frame. Figure 3.15 shows both rotations superimposed. Note that the convergent flow in Fig. 3.15 loses its initial coherence more rapidly through turbulent entrainment. The opposite rotation of the convergent flow terminates the effective helicity generated by the plume. Hence, dynamo modeling must include this effect.

#### 3.4.4 Differential Frame Rotation

We now consider where the background flow field is in differential rotation,  $\Omega_{differential}$ , as compared to  $\Omega = const$  flow. It is more difficult in this case to obtain accurate visualization images for two reasons: (1) the camera is mounted at  $R_0$  and therefore rotates at  $\Omega = \Omega_0$  whereas the plume, although injected at  $\Omega_0$ , soon is swept with the flow to an intermediate value of  $\Omega$ , and (2) the resulting shear within the flow around the plume and ahead of the plume leads to more rapid entrainment and consequently the dispersal of the "line" of bubbles. As a consequence we chose to use an intermediate flow field where the inner boundary rotates at  $\Omega_1 = \Omega_0(R_0/R_1)$ . Here we expect an inner region from  $R_1$  to  $R_2$ , where  $R_1 < R_2 < R_0$  that rotates as stable Couette flow,  $\Omega = \Omega_1(R/R_1)^2$  matched on to an outer region  $R_2 < R < R_0$  of weakly turbulent flow of  $\Omega = \Omega_0$  (Landau & Lifschitz 1959). However, the Reynolds number is not so high that these dis-



ting regions will exist separately. Consequently an approximation to this flow,  $\Omega_{frame} \propto 1/R$  is an equally likely alternative where the transition is spread out in radius. By way of comparison the maximum stable Couette flow corresponds to  $\Omega_{frame} \propto 1/R^2$  and will be used in the liquid sodium experiment. If the shear were greater, the flow field becomes unstable with resulting turbulence, large drag, and hence, power loss. Keplerian motion in an accretion disk has somewhat less shear,  $\Omega_{disk} \propto 1/R^{3/2}$  and is also stable because of gravity.



Figure 3.16: Top view showing plume rotation in an  $\Omega_{differential}$  fluid flow field. The differential rotation of the plume is faster in this case than in Figs. 3.9 and 3.10. We believe that the shear due to differential rotation enhances the rotation of the plume by partially entraining the shear flow. One notes that the plume drifts out of the field of view. This is because the camera rotation is fixed to the outer boundary at  $\Omega_0$  whereas the centerline of the plume rotates at an intermediate value,  $\Omega(R_2)$ . The duration of electrolysis pulse was 0.1 s.  $v_{R_0} = 48$  cm/s,  $v_{plume,LP} = 8.2$  cm/s. Frame rotation is clockwise.

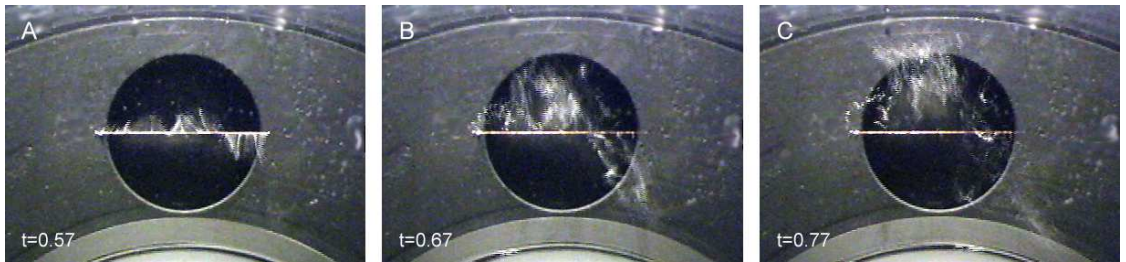


Figure 3.17: Delayed electrolysis pulse in an  $\Omega_{differential}$  flow field. This shows that the base of the plume has no further rotation with respect to the reference frame because of the convergent flow at the base of the plume. The electrolysis pulse was delayed from the plume pulse by 0.5 s, and the duration of electrolysis pulse was 0.1 s. Frame rotation is clockwise.

Figure 3.16 shows the effect on plume rotation through entrainment with



the  $\Omega_{differential}$  background flow. Compared to Figs. 3.9 and 3.10, Fig. 3.16 shows the differential rotation rate of the plume relative to the frame is higher, although the bubble line disperses more rapidly. The quantitative analysis of the plume for this case is shown in Fig. 3.13. This greater angular rotation is due to the entrainment with the differential rotation of the background flow. If the entrainment were instantaneous in the solid-body rotation case, then no plume rotation would be observed. Conversely, in the shear flow full entrainment without expansion would lead to a rotation of the plume approximately the same as the solid line corresponding to infinite expansion and no shear of Fig. 3.13. Hence entrainment plays an important, but not dominant role in determining the rotation of the plume.

Figure 3.17 shows how the convergent flow affects the plume rotation in the  $\Omega_{differential}$  case. We used an electrolysis pulse with 0.5 s delay and 0.1 s duration. Figure 3.17 shows that the converging flow at the base of the plume in the differentially rotating background flow has no further rotation. Since the  $\Omega_{differential}$  flow field enhances the divergent flow counter-rotation characteristic of the plume, it should reduce the co-rotation of the converging flow.

### 3.5 Conclusions

We have experimentally demonstrated the differential rotation of a plume that radially expands in a rotating frame. We have done so at high enough Reynolds number such that the scaling to much higher Reynolds number should be approximately invariant. The partial entrainment of the plumes with the background flow leads to a drag on differential rotation in the case of  $\Omega = const$  flow and to an acceleration of differential rotation of the plume in a differentially rotating frame. The basic understanding of Eq. 3.5 is substantiated. We therefore expect that our observed flows are a good match to the expected flow in the subsequent sodium dynamo experiment.

### 3.6 Geophysical and Astrophysical Examples

Large scale buoyant plumes originating in rotating stratified atmospheres should display similar rotation. Thunderstorms observed from a geostationary satellite should display this rotation. However, the differential rotation should be small since the duration of the plume is small,  $\sim 2\%$ , of the period of rotation of the earth. The largest scale plumes of the sun leading to supergranulation, on the other hand, rise in a week, a time comparable to the equatorial rotation period of  $\sim 27$  days. We note by way of confirmation that the leading sun spot of a pair always rotates toward the equator (Priest 1982). This is what we would expect if such plumes (not at the equator or poles) behaved and rotated as observed in these experiments. This assumes that such plumes lift and rotate a loop of toroidal magnetic flux from the base of the convection zone. The plumes rotate more slowly than the fluid of either hemisphere, i.e. *untwists* relative to the general rotation, and so the leading edge rotates toward the equator. The footprints of a loop of entrained magnetic flux emerging above the photosphere should track the rotation of the plume. Hence these footprints, or active regions should drift toward the equator as a function of rotation of the sun.

### Acknowledgments

We are particularly indebted to many colleagues who have helped and encouraged this work, particularly Dave Westpfahl, Dave Raymond, and James Weatherall of the New Mexico Institute of Mining and Technology (NMIMT) and Greg Willet, Marc Herant, Vladimir Pariev, and Hui Li of Los Alamos National Laboratory (LANL). We are appreciative of the help provided by the staff of the NMIMT Energetic Materials Research and Testing Center (EMRTC). In particular, Bill Shell, EMRTC Edit Studio, lent us the studio-quality TV and VHS/VCR system and the DV camcorder for the duration of the experiment and helped considerably with the downloading and editing of the digital images used for the experiment and this publication. Jerry Johnson built the first model which was subsequently greatly improved by John Simmons of EMRTC. We also wish to thank the City of Socorro, Gas Department for donating the low-pressure, high-volume regulator used on the apparatus. We are particularly indebted to IGPP of LANL for initial funding and to EMRTC and NMIMT for additional fund-

ing. Subsequently this work has been supported by NSF through grant number 99-00661. One of us, S.A. Colgate, receives funding through the DOE, under contract W-7405-ENG-36.

## CHAPTER 4

### DESIGN OF THE LIQUID SODIUM $\alpha\omega$ DYNAMO

#### 4.1 Introduction

The experiment consists of two coaxial cylinders rotating with different angular velocities,  $\Omega_0$  at  $R_0$ , the outer radius and  $\Omega_1$  at  $R_1$ , the inner radius, where  $R_0/R_1 = 2$ . The space between cylinders will be filled with liquid sodium with a small "topping" of mineral oil. The volume of sodium between the cylinders is limited by two end plates. One of the plates is solid while the other plate (referred to as the port plate) has two circular openings symmetric with respect to the rotation axis of the apparatus and of diameter  $R_{port} = (1/3)R_0$ . These ports are in turn connected to a plenum, supplied with pulsed pressurized liquid sodium, that forms the pulsed jets. There is also an annular space between the outer cylinder and the plenum. These periodic pulses of sodium flow are driven through the ports by a piston inside the plenum. Sodium flows out of the circular ports and returns back to the plenum volume through the annular space between the plenum cylinder and the outer cylinder. During injection of the jets, the resulting plume expands. Due to the Coriolis force acting on the expanding plume in the rotating frame, the plume rotates in the direction opposite to the direction of the rotation of the vessel in the same fashion as shown in Fig. 3.11. Such a rotating motion of the plume in the rotating frame and its axial translation corresponds to an unwinding helical motion. This helical motion produces the poloidal magnetic flux out of toroidal magnetic flux or  $\alpha$ -effect. The design drawings of the experiment are shown in Fig. 4.1.

In both figures the magneto-active volume with fluid sodium is the annu-

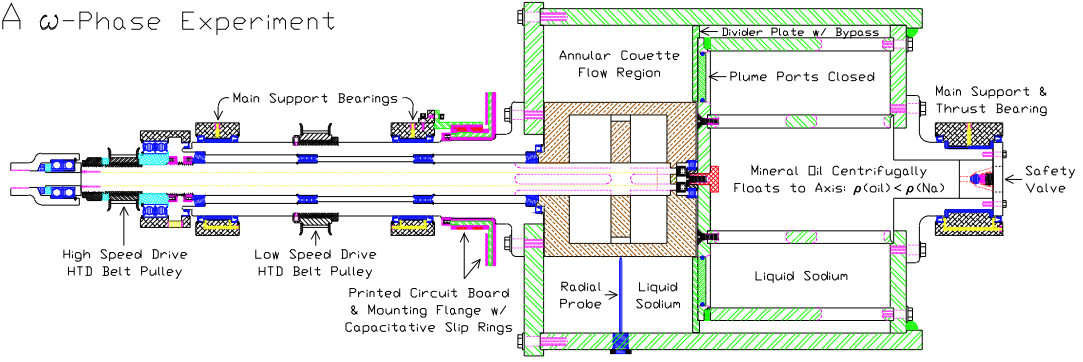
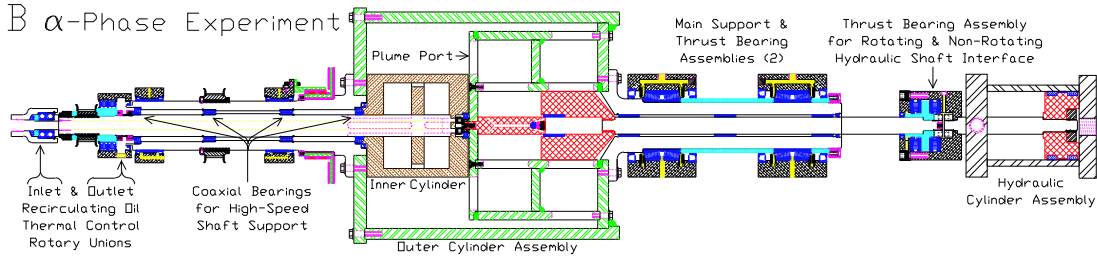
A  $\omega$ -Phase ExperimentB  $\alpha$ -Phase Experiment

Figure 4.1: Figure 4.1(A) shows a drawing of the rotating components of the  $\omega$ -Phase of the experiment. The inner cylinder is rotated at  $4\Omega$  of the outer or main cylinder of radius,  $R_0 = 30.5$  cm. In the  $\omega$ -Phase no plume piston, or hydraulic drive is shown, even though the constructed aluminum parts of Fig. 4.1(A) show the port plate and two ported reservoir plenum cylinders. The closed ports define the plume end of the Couette flow annular space. Figure 4.1(B) includes the plume drive mechanism. The external magnetic field coils are not shown but are designed and will be added later.

lar space between the differentially rotating inner and outer cylinders and between the left hand end plate and the middle port plate. Figure 4.1(A) is the first stage, the  $\omega$ -Phase of the experiment and is fully constructed. The plume generating mechanism or  $\alpha$ -Phase will be added in the second stage, Fig. 4.1(B). The purpose of first stage, without the plumes, is to demonstrate the production of the toroidal field from the velocity shear and the applied poloidal field. In addition some experiments will be performed to investigate the magneto rotation instability (MRI) using an axial applied field rather than a poloidal field with a radial component.

The second stage of the experiment will add the drive mechanism to produce the plumes and possibly lead to positive dynamo gain. Here the mid-plate has two ports for producing the pulsed jets from pressure generated in the plenum by a driven piston on the right. The port plate, plenum and drive mechanism are rigidly connected and rotate at  $\Omega_0$ . The inner cylinder will be rotating faster,  $\Omega_1$ , than the outer cylinder in order to create the differential rotation. It is driven by its own high speed shaft. The secondary drive shaft, belts and motor are not shown. Initially a 50 kW motor, pulsed to 100 kW will be used. Greater power can be applied if needed, but the basic limitation is the mechanical strength of the outer cylinder which contains the centrifugal pressure of the sodium. We have used aluminum for the construction contrary to the usual practice of stainless steel in reactor coolant technology. Here the temperatures are very much less and water vapor is excluded by mineral oil. In addition the useful experimental life of the apparatus is short such that the aluminum corrosion by NaOH will be negligible.

Since the end walls rotate at a different rate from the sodium in Couette flow, the velocity shear at the walls would produce eddy currents between the sodium and the conducting aluminum walls whenever an axial field component penetrates both. Thus in this case, no conduction is desired between the end walls and sodium and so this interface is insulated. This condition particularly applies when the field is made purely axial as for the MRI measurements. On the other hand, electrical conduction between the sodium and the inner and outer conducting aluminum cylinders is desired in order to maximize the magnetic shear for the production of the enhanced toroidal field. Finally we recognize that the Ekman layer flow at the end walls, a fast radial flow in a thickness  $\delta_{Ekman} \simeq R_0 Re y^{-1/2}$ , is so thin,  $\delta_{Ekman} \simeq 3 \times 10^{-4} R_0$ , that its electrical conduction current is negligible compared to the primary currents induced by the Couette flow.

The sodium will be heated and liquefied by the hot mineral oil driven

by a recirculating system through the space inside the inner cylinder. This oil flow also serves to maintain the thermal balance of the sodium, slightly above the melting temperature and also to prevent the further heating of the sodium due to the friction heat produced primarily in the Ekman layers. In addition, the non-recirculating mineral oil, used to “top” the sodium metal in the apparatus, isolates the liquid sodium from the rotating seals and the one internal bearing. This isolation of liquid sodium from the seals and bearing takes place because the density of oil is 0.86 of the density of the sodium at 110° C, and so the oil will float to the central axis of the rotating device.

The experiment will also have current coils to produce an external magnetic field within the magneto-active volume. These fields will be both with primarily radial (poloidal) or primarily axial components depending upon the emphasis of the the experiment, i.e., toroidal gain or MRI. All three components of the magnetic field will be measured by miniature Hall-effect detectors placed at a various radii inside a hydrodynamically shaped probe inside the sodium. In the second stage, with driven plumes, we hope to measure the flux and its orientation transported by the plumes or  $\alpha$ -effect. These measurements will be performed by an array of magnetic detectors placed on the surface of the end plate opposite a plume. The fast response time of the Hall-effect detectors, micro seconds, will allow one to record the detailed time evolution of the magnetic field produced by a single plume. A radial array of 5 pressure transducers will allow an accurate measurement of the pressure profile and thus a measurement of the Couette profile.

#### **4.1.1 Background Science and Engineering Parameters**

The maximum shear is desired in the rotational flow between the cylinders, yet maintaining stable flow. Therefore, in order to maximize the shear and maintain minimum fluid drag, (or minimize the torque with the walls and

hence, power) one should use Couette flow at the margin of stability, i.e. when  $\Omega_1 R_1^2 = \Omega_0 R_0^2$ . The New Mexico Dynamo Experiment is designed to have this marginally stable ratio of angular velocities of the cylinders. Namely,  $R_0/R_1 = 2$  and  $\Omega_1/\Omega_0 = 4$ . In the case of marginally stable Couette flow the angular velocity profile becomes

$$\Omega = \frac{\Omega_1 R_1^2}{r^2} = \frac{\Omega_0 R_0^2}{r^2}. \quad (4.1)$$

The geometrical parameters of the experiment are: inside radius of the outer cylinder is  $R_0 = 30.5$  cm, wall thickness of the outer cylinder is  $\Delta R = 3.2$  cm, length of the test-volume is  $L = 30.5$  cm, wall thickness of the port and end plates is  $\Delta L = 3.2$  cm, radius of the inner cylinder is  $R_1 = 15.25$  cm, the length of the space filled with liquid sodium in the plenum behind the port plate is  $L_1 = 35.6$  cm, radius of the plume ports is  $r_p = 4.9$  cm, the radial distance from the center of the plume port to the rotation axis of the cylinder is  $r_0 = R_1 + r_p = 20.15$  cm, the width of the annular space between the outer cylinder and the plenum is  $s = 2.6$  cm. One desires a size as large as possible, but is limited by the costs implied by available standard bearings, drive belts, material handling and machine tools.

The material for both cylinders, port and end plates, and the two ported reservoir plenum cylinders is aluminum alloy 5083-H3. This alloy has the necessary strength to sustain the centrifugal pressure of rotating sodium at the required temperatures. It is widely used in industry and properties well known. The high- and low-speed drive shafts, left and right flanges are made of steel. The kinematic viscosity coefficient of liquid sodium at  $110^\circ\text{C}$  is  $\nu = 7.1 \cdot 10^{-3} \text{ cm}^2 \text{ s}^{-1}$ . The magnetic diffusivity of liquid sodium is  $\eta = 810 \text{ cm}^2 \text{ s}^{-1}$ , the magnetic diffusivity of the aluminum alloy walls is  $\eta_{Al} = 650 \text{ cm}^2 \text{ s}^{-1}$ .

The analysis of stresses and energy dissipation in the experiment indicates that the maximum frequency of rotation of the outer cylinder is limited by the yield strength due to the centrifugal pressure and is  $\leq 33$  Hz. This corresponds



to  $\Omega_0 \leq 207 \text{ s}^{-1}$ . The angular velocity of the inner cylinder is always four times larger than the rest of the device and is limited by  $\Omega_1 \leq 828 \text{ s}^{-1}$ . At this angular velocity the average wall stress in the outer wall,  $\Delta R$  at  $R_0$  is  $\sim 1/4$  of the yield strength.

We define the global hydrodynamic Reynolds number of the Couette flow in the experiment as

$$\text{Re}_\Omega = \frac{\Omega_0 R_0 (R_0 - R_1)}{\nu}. \quad (4.2)$$

The magnetic Reynolds number for the rotational Couette flow is defined in a similar way as

$$\text{Rm}_\Omega = \frac{\Omega_0 R_0 (R_0 - R_1)}{\eta}. \quad (4.3)$$

Then, the ratio  $\text{Re}_\Omega / \text{Rm}_\Omega = \nu / \eta = \text{Pm}$  is a magnetic Prandtl number. For sodium at  $110^\circ \text{ C}$  one has  $\text{Pm} = 8.8 \cdot 10^{-6}$ . The maximum Reynolds numbers corresponding to the maximum possible frequency of rotation are  $\text{Re}_\Omega \approx 1.3 \cdot 10^7$  and  $\text{Rm}_\Omega \approx 120$ . This magnetic Reynolds number is higher than the one achieved in the successful dynamo experiments carried out so far, and we hope that this will allow us to investigate a wider spectrum of the behavior of conducting liquids. Particularly, the observations of MHD turbulence may be possible. At the same time, slower rotation rates can produce flows with as low magnetic Reynolds number as desired.

## 4.2 Design of the Experiment

This section shows the detailed engineering calculations of the strength of the vessel and the power to drive it to the necessary magnetic Reynolds number. Consequently we calculate the pressure and power as a function of  $\text{Rm}_\alpha$  &  $\text{Rm}_\Omega$  and then use an engineering stress analysis to demonstrate that our constructed experiment, Fig. 4.2, meets the criteria of the kinematic dynamo calculations above. These criteria are  $\text{Rm}_\alpha = 20$  and  $\text{Rm}_\Omega = 120$  with one pair of plumes per three

turns. The size, power and cost of the experiment are related to these desired values of  $Rm$ .

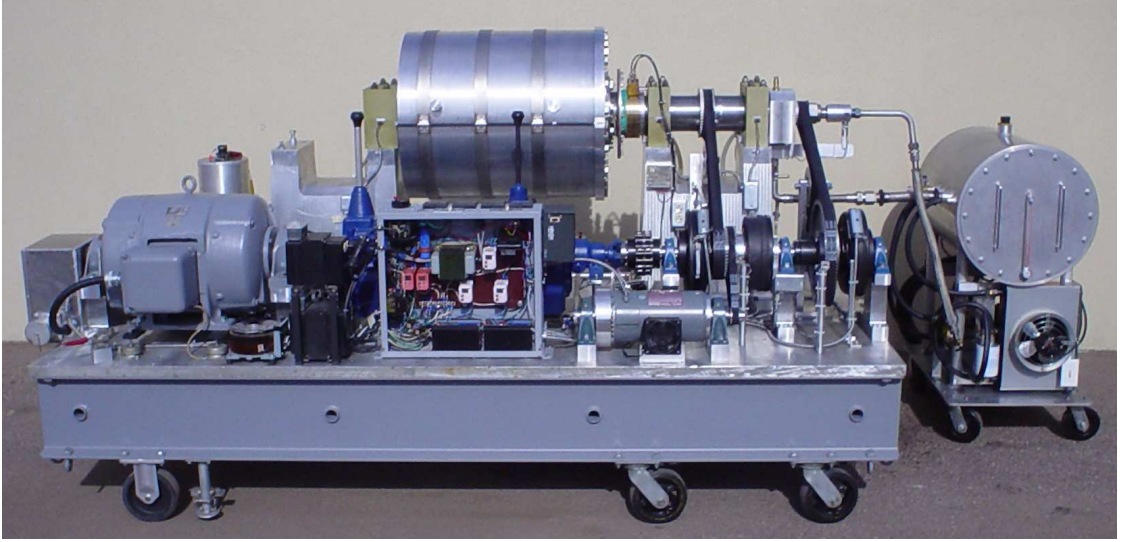


Figure 4.2: Figure 4.2 shows a photograph of the completed mechanical construction of the  $\omega$ -Phase of the experiment. For dynamo operation, the inner and outer cylinders are rotated by the 50 kW drive motor, shown on the left. The 1.5 kW DC motor/generator used for torque measurements is located immediately to the right of the electrical cabinet. For torque measurements, the apparatus can be differentially rotated by using both the AC motor and the DC motor/generator. The belt drives are driven from an intermediate shaft through two transmissions for variable speed. The recirculating thermal oil system is visible to the right. The electrical cabinet houses all the relays and controls for the main AC motor, electro clutches and DC brake used for safety. The variacs, isolation transformers and step-up transformers used for the DC motor/generator are shown immediately to the left of the electrical cabinet.

We have chosen cylindrical geometry as the closest approximation to the accretion disk geometry and the most convenient for construction. Spherical geometry would simulate stellar dynamos and make easier the calculation of resistive boundary conditions. We have also chosen Couette flow to minimize the fluid flow dissipation rate and maximize the shear or differential rotation for the  $\Omega$  flow. For a given desired  $Rm$  we will calculate how the pressure and power varies as a function of  $R_0$ , namely the choice of a size.

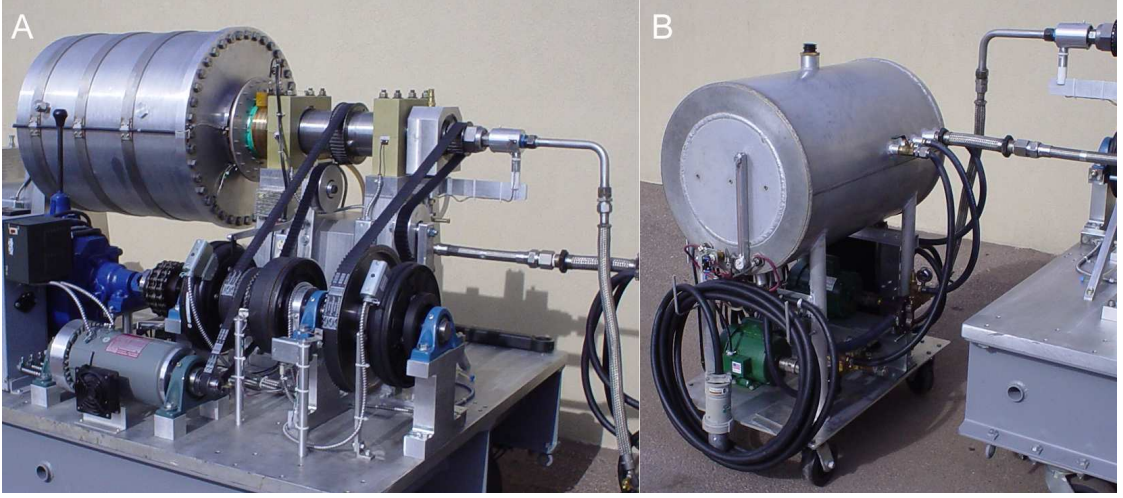


Figure 4.3: Figure 4.3(A) shows the drive system for the dynamo apparatus. The drive system consists of a 50 kW AC motor, two truck transmissions, an intermediate shaft, two electro-clutches, three belt drives, a DC brake for safety, and the DC motor/generator used for torque measurements. The outer cylinder is driven via the 1:1 belt drive on the left. It can be driven by either the AC motor via the electro-clutch on the 1:1 drive, or directly by the DC motor/generator via a 3.4:1 belt drive. The inner cylinder is rotated at  $4\Omega$  by a second electro-clutch and a 1:4 serpentine belt drive, shown on the right. The DC brake is directly mounted on the hub of 1:1 drive electro-clutch. It can thus always be used to stop the rotation of the outer cylinder which has an order of magnitude more mass than the inner cylinder. The recirculating thermal oil system is shown in 4.3(B). It is designed to provide 20 kW of thermal heating to the apparatus for sodium liquefaction and 4 kW of cooling for thermal control. Mineral oil flows at 1 liter/s and 1 atm pressure through the high-speed rotary union mounted on the high-speed shaft for the inner cylinder. The oil circulates into the cavity of the inner cylinder (shown in Fig. 4.1) and flows back through the annular space between the high-speed & low-speed shafts. The waste heating oil rotary union interfaces between the high-speed & low-speed shafts and returns the oil to the reservoir.

#### 4.2.1 Centrifugal Pressure

The centrifugal pressure in the fluid sodium determines the required strength of the vessel wall. For Couette flow,  $\Omega \propto 1/R^2$  or  $v \propto 1/R$  and the fluid pressure becomes:

$$P_{Na} = \rho_{Na}(v_0^2/2) \int_{R_0}^{R_1} \frac{v^2}{R} dR = \rho_{Na}(v_0^2/2) \left( \frac{R_0^2}{R_1^2} - 1 \right) = (3/2) \rho_{Na} v_0^2 \propto R_{m,\Omega}^2 / R_0^2 \quad (4.4)$$

when  $R_1/R_0 = 1/2$ . This ratio is chosen to maximize the annular space,  $R_0 - R_1$  for the dynamo and hence maximize  $Rm_\Omega = (R_0 - R_1)v_0/\eta_{Na}$ , yet minimize the acceleration and hence the wall stress at  $R_1$ . For rigid-body rotation and the thin-wall approximation, the inner wall stress becomes

$$\tau_1 = a_1 \rho_1 = \rho_1 v_1^2 / R_1 = \rho_1 (v_0^2 / R_0) (R_0 / R_1)^3. \quad (4.5)$$

Therefore for the ratio  $R_1/R_0 = 1/2$ , the inner wall stress will be  $\times 8$  the outer wall stress without fluid pressure. This then allows the outer wall to support primarily the fluid centrifugal pressure rather than its own centrifugal stress, whereas the inner cylinder supports just its own centrifugal stress. Thus for a limiting wall stress or pressure and a desired  $Rm_\Omega$ , the stress decreases as  $1/R_0^2$  and so there is a large advantage to size. With this in mind we chose the largest size for which there exists standard bearings, drive belts, mounts, surplus materials, materials handling, and local machine tools for finishing. This size is  $R_0 = 30$  cm, and  $Z_0 = R_0 = 30$  cm. We next calculate the achievable  $Rm_\Omega$  and  $Rm_\alpha$  within the envelope of wall stress and power and compare the results with dynamo calculations.

#### 4.2.2 Power Requirements

The power required to drive the  $\Omega$  flow is more complicated to estimate because the process of fluid dissipation is less well known in the particular limits of this experiment. We assume the Couette flow is absolutely stable and so the dissipation within the bulk of the fluid depends only on departures from ideal Couette flow. The primary departure is at the end walls where an Ekman layer forms (Batchelor 1999) of thickness  $\Delta Z \simeq R_0/2 Re_{fluid,\Omega}^{-1/2}$ . In our experiment the fluid Reynolds number is  $Re_{fluid,\Omega} = (R_0 - R_1)v_{Couette}/\mu_{Na} = Rm_\Omega(\eta_{Na}/\mu_{Na}) = 9 \times 10^6$ , where  $Rm_\Omega = 120$ ,  $\eta_{Na} = 750 \text{ cm}^2\text{s}^{-1}$  and  $\mu_{Na} = 10^{-2} \text{ cm}^2\text{s}^{-1}$ . The Ekman layer thickness becomes  $\Delta_{Ekman} = (R_0/2)Re_{fluid,\Omega}^{-1/2} \simeq 2.7 \times 10^{-4}$ . The radial flow velocity within the Ekman layers will be  $v_{Ekman} \simeq v_\Omega/2$  because the

flow is dissipative. Thus the Reynolds number of the flow within the Ekman layer becomes  $Re_{fluid,Ekman} = Re_{fluid,\Omega}^{1/2}/2 \simeq 1.8 \times 10^3$ . The flow at this Reynolds number is within the transition to turbulence and so we expect a larger effective viscosity than  $\mu_{Na} = 0.01$  and thus a larger thickness,  $Re_{turbulent,Ekman} > Re_{fluid,Ekman}$ . Recognizing this uncertainty, the power becomes the kinetic energy dissipated in the fluid flow in a cross-sectional area of  $2\pi R \Delta_{Ekman}$ . The change in specific kinetic energy occurs between the Couette flow,  $v_{Couette}^2/2$  and the wall at  $v_0^2(R/R_0)^2/2$ . Then the energy loss in two layers becomes

$$\begin{aligned} \dot{W}_\Omega &= \rho_{Na} \int_{R_1}^{R_0} \Delta_{Ekman} 2\pi R (v_\Omega^2 - v_0^2 (R/R_0)^2) (v_\Omega/2) dR = \\ &\rho_{Na} \pi v_0^3 \Delta_{Ekman} R_0 = 1.5 kW. \end{aligned} \quad (4.6)$$

This power is unrealistically small. It implies a spin-down time of

$$\tau_{spindown} = \frac{\rho_{Na} \int_{R_1}^{R_0} 2\pi R (v_\Omega^2/2 - v_0^2/2) Z_0 dR}{\dot{W}_\Omega} = \frac{\rho_{Na} \pi v_0^2 R_0^3 (9/8)}{\dot{W}_\Omega} = \frac{(9/8) R_0^2}{v_0 \Delta_{Ekman}} \quad (4.7)$$

Thus the spin down time corresponds to a number of turns of

$$N_{turns} = \tau_{spindown} \Omega_0 / 2\pi = (0.86 R_{fluid,\Omega_0}^{1/2} / 2\pi) \simeq 200. \quad (4.8)$$

The power predicted is unrealistically small and the number of turns for spin down is similarly unrealistically large. The Ekman flow will be broken up in a complicated fashion by the jet ports in one of the end plates, and so a more realistic estimate of the power required is times ten larger, or 12 kW, which in turn is modest. The scaling with  $R_{m,\Omega}$  of Eq. (4.6) becomes power  $\dot{W}_\Omega \propto R_{m,\Omega}^3 / R_0$  so that, again for minimizing power, there is a significant advantage in large size. Thus the initial fluid torque measurement becomes a critical determinant of the feasibility of the design.

Similarly the plume power is small. The area of two plumes is  $A_{plume} = 2\pi r_{plume,0}^2 = 2\pi R_0^2 (r_{plume,0}^2 / R_0^2)$ , and so the plume power becomes

$$\dot{W}_\alpha = A_{plume} (v_{plume}^2/2) L_{plume} (\Omega_0/2\pi) n_{plumes/turn} =$$

$$2\pi R_0^3 (r_{plume,0}^2/R_0^2) (v_{plume}^2/2) (\Omega_0/2\pi) n_{plumes/turn}. \quad (4.9)$$

For  $v_{plume} = v_0/2$ ,  $n_{plumes/turn} = 1/3$ , and  $r_{plume,0}/R_0 = 1/6$ , we have  $\dot{W}_\alpha = 20$  kW. This too is modest and well within a feasible design limit of 50 kW. We expect the plumes and the  $\Omega$  flow to interact adding to the dissipation of the  $\Omega$  flow, but this should be proportional to the volume ratio, well within the factor of ten additional dissipation allowed for. Thus we don't see power as the limitation, but instead pressure and the strength of the vessel.

### 4.3 Engineering of the Experimental Apparatus

#### 4.3.1 The Cylindrical Vessel

The actual design parameters are: an outer cylinder of  $R_0 = 30.5$  cm (12 in) with a wall thickness of  $\Delta R_0 = 3.2$  cm (1.25 in) and test-space length of  $Z_0 = 30.5$  cm (28 in). Since  $R_{m,\Omega} = 120$  and  $\eta_{Na} = 750 \text{ cm}^2 \text{ s}^{-1}$ ,  $v_0 = 6 \times 10^3 \text{ cm s}^{-1}$ . Consequently the pressure of the liquid sodium at the wall from Eq. (4.4) is  $P_0 = 72 \text{ atm}$  (1100 psi).

The thin wall cylindrical vessel under pressure is the simplest stress analysis,  $\sigma_{hoop,Al} = P_{Na}(R_0/\Delta R_0) = 544 \text{ atm}$  (8,000 psi), (Formula (1b), Table (29), p. 448, "Formulas for Stress and Strain", Roark & Young 1975). Similarly there is an additional stress due to the centrifugal acceleration of the cylindrical vessel itself. In this case for aluminum with density 2.7 and again in the thin wall limit  $\sigma_{hoop,Al} \simeq \rho_{Al} v_0^2 ((R_0 + \Delta R_0)/R_0) = 107 \text{ atm}$  (1,570 psi) (p. 566, "Formulas for Stress and Strain", Roark & Young 1975). Since this stress is also a hoop stress, it can be directly added to that from the liquid sodium to give a total hoop stress in the aluminum cylinder of 651 atm (9,570 psi). The aluminum of the cylinder is 5083H3, which at a temperature of 110C, has a yield strength of 2,177 atm (32 ksi). Thus we feel that the wall stress at the maximum conditions will be 1/3 the yield strength. As an additional safety measure the vessel is banded with stainless

steel, pre-compressing the vessel by 136 atm (2000 psi) at an internal stress of the banding of half the yield strength of the banding.

The axial stress in the cylinder is determined by the integral of the end wall pressure, Eq. (4.4), the force  $F_{end}$  divided by the circumference and the thickness,

$$F_{end} = \int_{R_0}^{R_1} (2\pi R) P_{Na} dR = 2\pi \rho_{Na} (v_0^2/2) \int_{R_0}^{R_1} R \left( \frac{R_0^2}{R^2} - 1 \right) dR = \pi R_0^2 v_0^2 \left( \frac{R_0^2}{2R_1^2} - \ln(R_1/R_0) \right) = 1.31\pi R_0^2 v_0^2. \quad (4.10)$$

For  $\rho_{Na} = 1$  and  $R_1/R_0 = 1/2$ , the axial stress becomes

$$\sigma_{axial,Al} = \frac{F_{end}}{2\pi R_0 \Delta R_0} = 0.65 v_0^2 (R_0/\Delta R_0) \quad (4.11)$$

For the desired value  $v_0 = 6000$  cm/s, the axial stress becomes 220 atm (3,300 psi). This adds vectorally to the hoop stress a small  $\simeq 10\%$  addition. We will initially perform the tests with the thrust end-plate welded and the driven end-plate bolted using 40, grade 316SS, 3/4 - 10  $\times$  3 bolts on a 32 cm (12.62 in) bolt circle. The resulting bolt stress becomes 2,721 atm (40 ksi), an acceptable value.

### 4.3.2 The End Plates

The thrust end-plate is 6061T651 aluminum of thickness  $\Delta Z_{end} = 3.2$  cm (1.25 in), 61 cm (24 in) o.d. with an i.d. of 20.3 cm (8 in). The driven end-plate is 5083H3 aluminum of thickness of  $\Delta Z_{end} = 3.2$  cm (1.25 in), 70 cm (27.5 in) o.d. with an i.d. of 17.8 cm (7 in).

The maximum centrifugal stress in these annular plates is given by Formula (6), p. 567, "Formulas for Stress and Strain", Roark & Young 1975 as

$$\sigma_{end,centrif} = \rho_{Al} \frac{3+\nu}{8} v_{0,end}^2 (1 - (R_{hole}/R_{outer})^2) \simeq v_{0,end}^2 = 17.5 \text{ atm (250 psi)} \quad (4.12)$$

for the conditions  $R_{hole}/R_{outer} = 1/4$  and the desired velocity of  $v_0 = 6000$  cm/s. Thus the centrifugal stress in the end plates is negligible.

The bending stress due to the fluid pressure is more significant. We must consider a circular plate of outer radius  $R_{end,outer}$ , fixed by the cylinder and loaded with the pressure distribution of Eq. (4.4) from  $R_0$  to just inside  $R_1$  with the inner edge guided. The bolting or welding to the cylinder serves the purpose of "fixing" the outer radius with the inner radius guided by the flanges and no axial confinement by the bearings. Formula (3<sub>f</sub>) of Table (24), p. 345 of "Formulas for Stress and Strain", Roark & Young (1975), best fits this circumstance of outer edge fixed and inner edge guided with a linearly increasing pressure distribution extending from  $R_1$  to  $R_0$ . This approximation is conservative relative to the quadratic distribution. The actual case is between these limits. The maximum stress in the plate then becomes

$$\sigma_{end,max} = 6P_0(R_0/\Delta Z)^2 K_{MR} = 600P_0 K_{MR} \quad (4.13)$$

for both the driven and thrust plates where  $R_0/\Delta Z_{end} \simeq 10$ . Then for  $R_0/R_1 = 2$ , Formula (3<sub>f</sub>) gives  $K_{MR_0} = 0.025$  and  $K_{MR_1} = 0.011$ . The corresponding stresses become  $\sigma_{end,R_0} = 15P_0$  and  $\sigma_{end,R_1} = 6.6P_0$ . At our desired velocity of 6000 cm/s, these become  $\sigma_{end,R_0} = 544$  atm (8000 psi) and  $\sigma_{end,R_1} = 238$  atm (3500 psi). Both of these stresses are modest compared to the strength of 6061T651 Al at 110 C of 2,177 atm (32 ksi). The deflection of the plates under this load is given by

$$\delta Z_{end} = K_{y,R_1} \frac{\frac{F_{end}}{2\pi R_0} R_0^3}{D} \quad (4.14)$$

Where the plate constant,  $D = E_{Al} \Delta Z_{end}^3 / (12(1 - \nu^2)) = 1.8 \times 10^6$ . Then for  $K_{y,R_1} = 7 \times 10^{-4}$ , the deflection on axis  $\delta Z_{end} = 8 \times 10^{-3}$  cm ( $3 \times 10^{-3}$  in). This is a negligible axial deflection considering the end play in the thrust bearing and the much larger thermal expansion of  $\Delta Z_{thermal} = \Delta T L_0 K_{thermal} \simeq 0.04$  cm (0.016 in).



We recognize that this analysis is not exact, but have hydrostatically tested the vessel, measured the deflections, and compared the deflections to these estimates. The measured values were within 5% of the calculated values. Additional strength can be added to weak points in the design later if necessary, but the major fraction of the physics is accessible at one half the planned maximum velocity and therefore at 1/4 the stress.

### 4.3.3 Dynamic Balance and Bearings

The rotating mass of the vessel and shafts is  $M_{rotating,R_0} \simeq 500$  kg. We have designed the primary support bearings of nominal size 12.7 cm (5 in), to operate for a "normal" lifetime of  $10^8$  revolutions (4 months at 30 Hz) with a load of  $\times 100$  the rotating mass. Since the acceleration at  $R_0$  is  $a(R_0) = 10^3$  g, then we can expect the bearings to support an out-of-balance rotating load of 1/10 the static mass at  $R = R_0$ . This is conservatively large. The mass of the base and mounts is  $\simeq \times 3$  the mass of the rotating apparatus or 1500 kg, so that without additional restraint, the static support and mounts will restrain an out-of-balance mass of  $\simeq 150$  kg at  $R = R_0$ . This also is a conservatively large out-of-balance error. Our electronic sensors weigh  $\simeq 100$  g and we expect to balance the rotating mass to  $\simeq 10$  g corresponding to an out-of-balance load of 10 kg at  $R = R_0$ . Automotive crank shafts are routinely balanced to 0.01 g at  $R = 5$  cm. The lubrication system for the primary support bearings is shown in Fig. 4.4.

For Couette flow the inner cylinder rotates at  $\Omega_1 = 4\Omega_0$  and so the acceleration becomes  $a(R_1) = 8 \times 10^3$  g. This larger acceleration requires a more careful balancing, but since the inner cylinder is a single part whose mass  $M_{rotating,R_1} \simeq 20$  kg or  $\simeq 0.06M_{rotating,R_0}$ , the degree of balance, 0.1 g at  $R = R_1$ , is also feasible on an automotive crank shaft balance system. With this degree of out-of-balance mass of 10 and 0.1 g respectively and thus with an out-of-balance load of  $M_{load} = 10$  kg, we expect a vibration amplitude of  $\Delta R = 2M_{load}g/(M_{mount}\Omega_{0,1}^2) \simeq 2 \times 10^{-4}$  cm.



Figure 4.4: Figure 4.4 shows a photograph of the completed mechanical construction of the  $\omega$ -Phase of the experiment. The lubricating oil system is visible in the foreground. The electrical control system for the 50 kW drive motor, shown to the right, is electrically interlocked to the lubrication system. This is so that the AC motor cannot be started unless the lubrication system is on and operating at the design pressure of 2 atm.

Since this is much smaller than the bearing clearances, we expect the vibration amplitude to be that of the rotating mass itself resulting in an amplitude of  $\times 10$  larger or  $\Delta R = 2 \times 10^{-3}$  cm. Again this amplitude of vibration is minor.

#### 4.3.4 Seals

We next consider the rotating seals. We plan to operate the experiment with a small quantity of mineral oil,  $\sim 100$  to  $1000 \text{ cm}^3$  in contact and floating above the liquid sodium. The density of oil is  $\rho_{oil} \simeq 0.96 \rho_{Na}$  and consequently floats above liquid sodium. We have performed MHD experiments in the past taking advantage of this small density difference (Colgate 1960) and the oil coating avoids

the requirement for using an inert gas in the handling of liquid sodium. Thus, in the rotating frame of the the experiment, the oil "floats" to the axis. We expect to adjust the quantity of oil such that the shaft seals are always bathed in oil, not sodium. This ensures that the industrial problem of seals and liquid sodium is avoided.

#### 4.3.5 Thermal Properties

Solid sodium is an excellent thermal conductor,  $\simeq 1/2$  that of copper. Hence, the thermal time constant of the entire mass, heated or cooled from inside the inner cylinder by hot oil is  $t_{heat} = R_0^2/D_{thermal} \simeq 600$  s. Once the sodium is hot enough to liquefy, at 100 C, convection is rapid and the experimental mass becomes isothermal. For example, the heating of 20 kW of heat or power dissipation is  $t_{heat} = (heat/power) = 2000$  s or 1/2 hour. Similarly an experimental run lasting 10 seconds at high power, e.g. 50 kW, will heat the whole apparatus by 1 deg C without cooling, an acceptable small value. Cooling by windage will be comparable. Figure 4.3(B) shows the recirculating thermal oil system used for sodium liquefaction and cooling for thermal control.

#### 4.4 Torque Measurement Equipment and Instrumentation

The measurement of torque for the apparatus is performed by a gimbaled DC motor/generator connected to the outer cylinder belt drive. Gimbaling the 1.5 kW DC motor/generator housing allows it co-rotate or counter-rotate in reaction to electromagnetic force developed between the DC armature and field. The housing is constrained from rotating by a lever arm extending from one of the gimbal bearing trunnions out to force sensors which capture it. Thus torque can be directly measured from the cross product of the lever arm length at a fixed radius and the perpendicular force induced at that point as  $\tau = R \times F$ . This system of force sensors and gimbaled DC motor/generator is shown in Fig. 4.5.

Figure 4.5(A) shows the force sensors and lever arm used to measure torque in the apparatus. For the sensor configuration shown in Fig. 4.5(A), the length of the lever arm from the DC motor/generator rotation axis centerline to the counter-rotation force sensor is 125.00 cm. The distance between sensors is 6.00 cm. Thus the length of the lever arm from the DC motor/generator rotation axis centerline to the co-rotation force sensor is 131.00 cm.

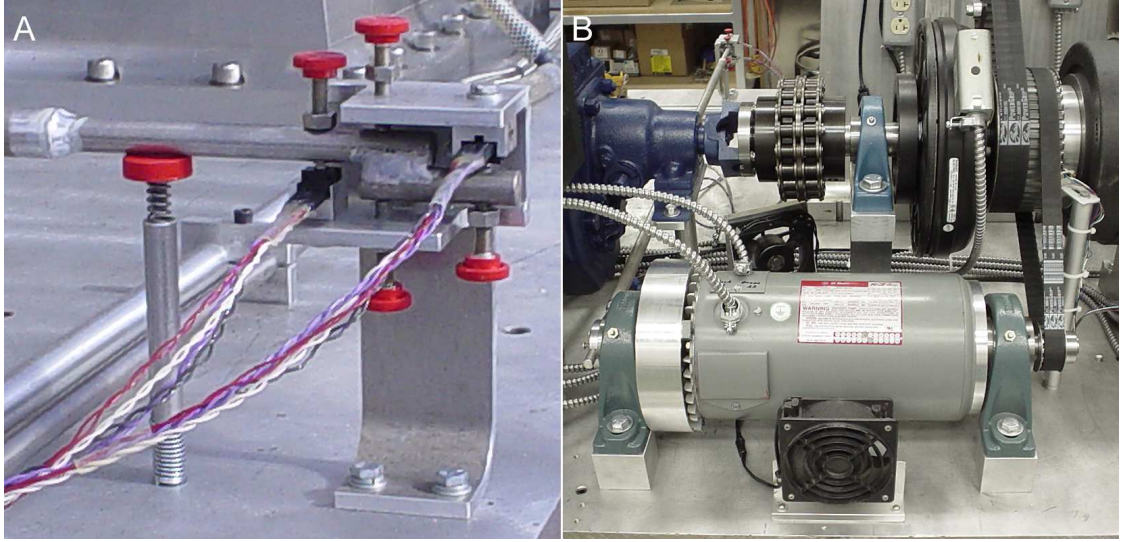


Figure 4.5: Figure 4.5(A) shows a photograph of the force sensors and lever arm used to measure torque in the apparatus. The bottom surface of the lever arm coincides with the centerline axis of the DC motor/generator. The offset in the end of the lever arm allows each sensor to measure force produced about the rotational axis of the motor without having to correct for angular offset. The sensor on the left (under the lever arm) measures the motor reaction counter-rotation force. The sensor on the right (over the lever arm) measures the generator reaction co-rotation force. This instrumentation provides  $\tau-$ , the background drag of the rotating mass in its support bearings, including its drives, and  $\tau+$ , the torque dissipated by the annular rotational Couette flow. Figure 4.5(B) shows the 1.5 kW DC motor/generator and its 3.4:1 ratio belt drive to the drive pulley for the outer cylinder. The DC motor/generator has bearing trunnions mounted on each end so that the housing itself is gimbaled, i.e. the housing is able to rotate about armature rotational axis, constrained by the lever arm captured between the force sensors. The lever arm extending to the mount for the force sensors can be seen in the left of Fig. 4.5(B).

#### 4.4.1 Configuration for Background Torque Measurements

Measurements of the background torque required to rotate the apparatus in solid body rotation are made by using the DC motor to drive the outer cylinder. For these measurements the AC motor is driving the intermediate shaft at a constant rate of 2.9 Hz so that the bearing friction in the outer cylinder drive electro clutch hub is minimized. Also for these measurements, the 1:4 ratio serpentine belt is on and tensioned, but the electro clutch for the inner cylinder is not engaged. The annular space in the coaxial drive for the inner and outer cylinders is filled with mineral oil as a closed system so that the coaxial drive bearings and seals are lubricated. Background torque measurements are made with the annular test space of the apparatus both empty of any fluid and filled with deionized  $H_2O$ . The apparatus has an internal volume of  $\sim 150$  liters. Thus the increase in mass when filled is  $\sim 150$  kg (320 lb). These measurements indicate a change in kinetic friction and associated drag in the primary support bearings of the apparatus. The data from the solid body rotation background torque measurements are presented in Table 6.2 and are graphically displayed in Fig. 6.1.

#### 4.4.2 Configuration for Torque Transmitted by the Fluid Measurements

Measurements of the torque transmitted by the fluid in annular rotational Couette flow established during differential rotation of the apparatus are made using the DC motor/generator to both drive and brake the outer cylinder. For these measurements the AC motor is used to drive the inner cylinder at a constant rate via the electro clutch and 1:4 ratio serpentine belt drive. The inner cylinder constant rate is determined by the test parameters desired. These rates are presented in Table 6.1. Measurements of the torque transmitted by the fluid are made with the annular test space of the apparatus both empty of any fluid and filled with deionized  $H_2O$ . The torque transmitted by the fluid is the difference

between the torque required to differentially rotate the apparatus when empty and when filled. Measuring the force at the sensors as a function of  $\Omega_0$  frequency for a fixed  $\Omega_1$  frequency allows the direct calculation of torque for each empty and filled configuration. The data from the force measurements of differential rotation for the outer cylinder when the apparatus was empty and filled are presented in Tables 6.3-5. The calculated and graphically displayed values of torque as a function of outer cylinder frequency for differential rotation are presented in Figs. 6.2-4. Based on the ability of the fluid to transmit torque between the inner and outer cylinders, the DC generator can be used to control co-rotation for high  $\Omega$  ratios. As required by the ability of the fluid to transmit torque, for measurements approaching the limiting stable Couette flow  $\Omega$  ratio of 4:1, the DC motor can be used to differentially drive the outer cylinder.

#### 4.5 Safety

The fear of sodium may have been fueled by youthful indiscretions in the chemistry lab, yet metallic sodium is a major industrial chemical. Industry has used millions of tons of metallic sodium, shipped in thousands of railroad tank cars of greater than 50 tons each. These tank cars are surrounded by an oil jacket for heating. This is accomplished with negligible risk to the public as determined by DOT. The mass of sodium in each tank car is more than several hundred times the mass of sodium used in our experiment. Sodium is also shipped in barrel size containers where the container is non-returnable. Liquid sodium is the lowest density, high conductivity fluid that is biologically benign. There is a vast difference between using sodium at 600 deg C as a fast reactor coolant and using sodium at 110 C as in this experiment. Much of the high end technology of liquid sodium was developed for the high temperature coolant purpose. Those facilities, built on a massive scale and now surplus, have been used for two recent successful sodium dynamo experiments in East Germany and Latvia, Gailitis et

al. (2000), Busse et al. (1996) and Rädler et al. (1998). These experiments were performed in immense halls for full containment of a liquid sodium equipment failure. We believe that this scale, cost, and the equipment is an unnecessary burden. We expect to test a different dynamo flow field in more modern and modest equipment, developed in the laboratory and easily moved periodically to and from an adjacent, proven testing facility for high-energy materials (whenever testing with liquid sodium). These tests will be performed remotely. This facility, the Energetic Material Research and Testing Center (EMRTC) has a 60 year history of tens of thousands of accident free high explosive tests. Finally one of us, Colgate (1955), has had extensive hands-on use of liquid sodium in laboratory experiments for determining MHD stability for fusion confinement.

The experiment will be performed in compliance with Federal, State, Industry and Institutional safety practices and procedures involving the receipt, storage, handling, disposition and use of sodium metal. The *Safety Practices, Procedures and Compliance* are presented at the web-site for the project:

<http://physics.nmt.edu/~dynamo/>.

A removable, electrically heated, safety shield will surround the cylindrical vessel and will be used whenever the apparatus is rotated and filled with either oil or sodium. This will confine any dynamic sodium loss and absorb the kinetic energy and containment of disrupted parts should a mechanical failure occur.

Operating procedures will include: safety training, hydrostatic pressure testing, pressure deflection checks, calibration of pressure sensors, relief-valve testing and setting, and thermal controls. These *Operating Procedures* are presented at the web-site for the project: <http://physics.nmt.edu/~dynamo/>

## 4.6 Electronic Instrumentation

The electronic instrumentation has been designed and constructed by graduate student Rocky Ginanni with the help of NMIMT faculty members William Rison and Richard Sonnenfeld, and undergraduate students, Clint Ayler, Manuel Jaramillo, Ian Bentley, and Robert Koegler. Figures 4.6 and 4.7 show the rotating (Fig. 4.6(A)) and stationary (Fig. 4.7(A)) instrumentation circuit boards along with the computer interface board (Fig. 4.7(B)) used for bi-directional control of the sensor systems.

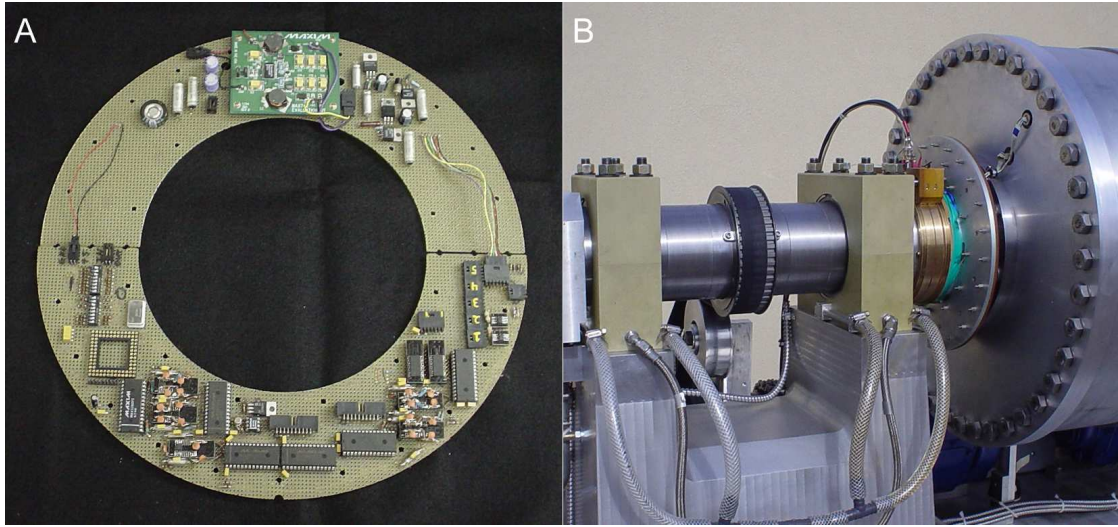


Figure 4.6: The electronic circuit board for acquisition, conversion and transmission of the rotating data is shown in Fig. 4.6(A). The two halves of the annular circuit board are mounted on the apparatus as denoted in Fig. 4.1(A). The mounting flange for the annular circuit board can be seen in Fig. 4.6(B) along with the capacitatively coupled slip rings and pick-up shoe. Two of the five radially positioned, axially oriented pressure transducers can be seen mounted in the drive end plate. The annular circuit board assembly utilizes real-time digital control of the power to and signals from the analog magnetic field, conductivity, pressure and temperature sensors.

The rotating circuit board has been designed to measure the pressures at 5 radii at the end plate, temperatures (at 10 locations) and magnetic fields at various locations. The primary measurement of either the turbulent fields from the



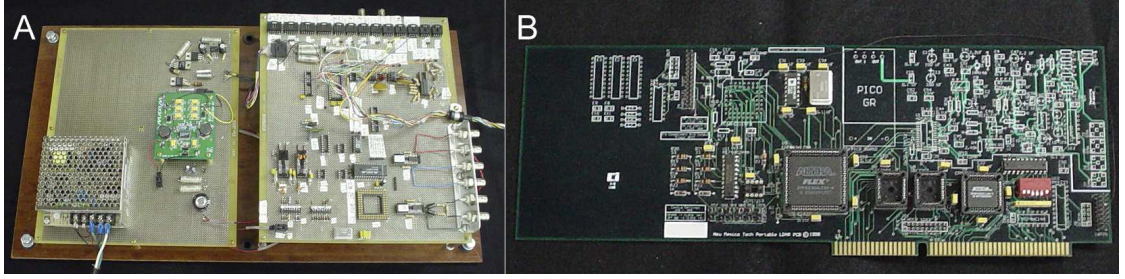


Figure 4.7: The circuit board shown in Fig. 4.7(A) is the stationary board used to interface the long-line transmission of bi-directional digital data from the remote operations van to the apparatus ( $\sim 100$  m). It also controls and acquires non-rotating sensor data. Non-rotating sensor data includes force sensors for apparatus torques, AC motor torque, AC motor current, DC motor field and armature voltages & currents, lubrication and recirculating oil temperatures & pressures. The printed circuit board shown in Fig. 4.7(B) is the computer interface board used for real-time control, acquisition and storage of the digitized analog sensor signals. This printed circuit board was provided to the New Mexico Dynamo Experiment by the New Mexico Tech Lightning Mapping Array project, courtesy of Dr. William Rison, NMIMT Electrical Engineering faculty.

MRI, the toroidal gain due to the shear or possible dynamo gain will all depend primarily upon 6 (3-D) Hall detectors (18 single-axis, 0.2 G to  $\sim 10$  kG detectors) mounted within a radial probe, Fig. 4.8.

In Phase II, the  $\alpha$ -Phase, there will be an additional array of 30 (3D) Hall detectors on the outside of the end plate to measure the fields induced by the plumes for the  $\alpha$ -helicity generation. A property of the plume-generated,  $\alpha$ -helicity is that the resulting poloidal flux appears external to the vessel and so can be diagnosed externally. A fraction of the magnetic signal induced by MRI turbulence will also be observable from outside the vessel, but not in Phase I. The detector signals are converted for digital transmission to the computer. In total, 128 sensors (fields, conductivity, pressures and temperatures) are designed to be monitored at  $\sim 10$  MHz data rate from a rotating system with a centrifugal acceleration of  $\sim 1000$  g at the sensors and  $\sim 300$  g at the electronics. The sensors for the first phase have been tested and mounted.



Figure 4.8: Figure 4.8 shows a photograph of the hydrodynamically shaped aluminum housing of the radial probe for the six, 3D Hall magnetic field detectors. The radial probe housing has an chord to thickness aspect ratio of 5:1. The thickness of the probe is 6 mm. It is hollow nearly to the nose with a wall thickness of 0.6 mm. It threads into the outer cylinder and is sealed externally.

### Acknowledgments

We would like to express our gratitude to Dr. William Rison, NMIMT Electrical Engineering faculty, and the New Mexico Tech Lightning Mapping Array Project. Dr. Rison provided the New Mexico Dynamo Experiment with the computer interface board used for real-time control, acquisition and storage of the digitized analog sensor signals.

## CHAPTER 5

# HYDRODYNAMIC THEORY OF COUETTE FLOW AND THE EKMAN LAYER

### 5.1 Introduction

Prior to demonstrating the  $\Omega$ -deformation, the experimental apparatus will be used to investigate two important fluid dynamic areas of interest: Couette flow and Ekman layers at high Reynolds number. Given the size  $l = \Delta r = 15$  cm and peripheral tangential velocity  $u = 5.7 \times 10^3$  cm/s of the fluid annulus, and liquid viscosity of the sodium  $\nu = 0.68$  cP, the maximum fluid Reynolds number for the experiment is  $Re = lu/\nu = 12.6 \times 10^6$ . For investigations independent of the use of sodium, e.g. water or oil,  $Re \sim 10^7$ . The investigation of Couette flow at  $Re \simeq 10^7$  will surpass previous laboratory experiments where  $Re$  is significantly less,  $Re < 10^6$ . Given the Reynolds number for the Ekman layer  $Re_E$  scales as  $Re^{1/2}/2$  (derived in Sec. 5.2.2),  $Re_E = 1775$ . With  $Re_E > 1000$ , turbulence in the boundary layer at the end of the differentially rotating annular region should dominate. The configuration of the experiment with  $Re_E \simeq 1.8 \times 10^3$  indicates that a turbulent Ekman layer exists. This is the first experiment to investigate the probable existence of Ekman layer turbulence using this configuration.

### 5.2 Couette Flow and the Ekman Layer

Couette flows are generally classified as fluid motion generated by the movement of one surface of a channel or confined region. Conventionally these flows are utilized for the measurement of viscosity. Pressure gradients that result from these flows are an artifact of the system's response or are induced by the system internally. Couette-Poiseuille flows are fluid motions generated jointly by a

moving surface and an applied pressure gradient. The various types of Couette flow are planar, longitudinal annular, planar rotational, annular rotational (Churchill 1988). Annular rotational Couette flow is applicable to the fluid flow field within the apparatus where the  $\Omega$ -deformation will be established. Annular rotational Couette flow is also known as circulating Couette flow. Planar rotational Couette flow is applicable to the fluid flow field at the end plates.

Figure 5.1 shows a schematic of the annular region in the experimental apparatus where Couette flow will be established. Annular rotational Couette flow will make up the preponderance of the fluid flow in the annulus. For reasons discussed below, the velocity profile of the annular rotational Couette flow will be such that the tangential velocity of the fluid is inversely proportional to the radius, i.e.  $u \propto 1/r$ . The rigid end plates rotate with a solid-body rotation profile where  $u \propto r$ . Planar rotational Couette flow is developed between these two velocity profiles. It is the interface region between the  $u \propto 1/r$  flow and the  $u \propto r$  flow where the Ekman layer develops and is of interest and importance.

The reason for using the annular rotational Couette flow velocity profile of  $u \propto 1/r$  is because the angular momentum is constant, i.e. independent of radius, and the flow field is stable (Chandrasekhar 1961, Churchill 1988). Stable Couette flow is where the shear stress in the adjacent layers of fluid sliding over one another is laminar throughout the flow field, with no-slip boundary conditions. Couette flow is stable essentially only within the regime  $u \propto r \rightarrow u \propto 1/r$ . Turbulent instability results from flows outside of this regime. The dynamo experiment needs as large a velocity shear in the fluid as possible. Couette flow with  $u \propto 1/r$  represents the unique circumstance of large velocity shear where the fluid flow is stable, and therefore believed to represent the minimum power required to obtain the maximum velocity shear.

The forthcoming applications and solutions of fluid dynamic theory first

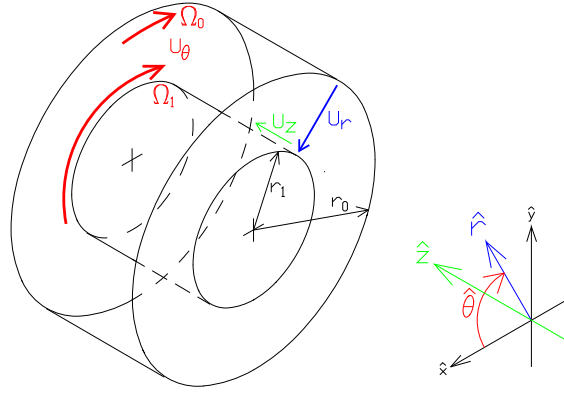


Figure 5.1: Schematic of the annular region in the New Mexico Liquid Sodium  $\alpha - \Omega$  Dynamo Experiment apparatus where Couette flow will be established. The outer cylindrical surface at  $R_0$  and end-walls of the annulus rotate at 30 Hz. The inner cylindrical surface at  $R_1$  rotates at 120 Hz. Stable, vorticity-free, annular rotational Couette flow is established in the bulk of the fluid annulus away from the immediate surfaces of the end-walls. Planar rotational Couette flow takes place at each of the end-walls. This is where the differentially rotating fluid annulus interacts with the solid-body rotating end-plate surfaces through the Ekman layer.

develop the annular rotational Couette flow characteristics and then those of planar rotational Couette flow. The reason being that if the annular rotational flow is representative of solid-body rotation, then no planar rotational flow will be developed in the annulus. It is because the annular rotational flow is differential with respect to radius that the planar rotational flow exists and the Ekman layer develops. The Navier-Stokes equation can be used to couple the two flows together and relatively completely describe the annular flow field expected in the apparatus.

In vector notation, the Navier-Stokes equation is

$$\rho \frac{\partial \vec{u}}{\partial t} + \rho(\vec{u} \cdot \nabla) \vec{u} + \nabla p = \rho \vec{g} + \rho \nu \nabla^2 \vec{u} + (\rho \nu_b + \rho \nu/3) \nabla(\nabla \cdot \vec{u}) \quad (5.1)$$

The terms in the above equation of motion for a viscous Newtonian fluid represent acceleration, convective acceleration, pressure gradient, body forces, viscosity, and compressibility (Thompson 1988, Hughes & Brighton 1991). Bulk viscosity is denoted by  $\nu_b$  and kinematic viscosity by  $\nu$ . The case of constant density, negligible

body forces, constant viscosity, and an incompressible fluid is pertinent to the experiment. In cylindrical coordinates, the  $r$ ,  $\theta$  and  $z$  components of the Navier-Stokes equation used to describe the fluid dynamic aspects of the rotational flow fields are

$$\begin{aligned} \frac{\partial u_r}{\partial t} + u_r \frac{\partial u_r}{\partial r} + \frac{u_\theta}{r} \frac{\partial u_r}{\partial \theta} + u_z \frac{\partial u_r}{\partial z} - \frac{u_\theta^2}{r} = \\ -\frac{1}{\rho} \frac{\partial p}{\partial r} + \nu \left[ \frac{\partial^2 u_r}{\partial r^2} + \frac{1}{r} \frac{\partial u_r}{\partial r} + \frac{1}{r^2} \frac{\partial^2 u_r}{\partial \theta^2} + \frac{\partial^2 u_r}{\partial z^2} - \frac{u_r}{r^2} - \frac{2}{r^2} \frac{\partial u_\theta}{\partial \theta} \right] \end{aligned} \quad (5.2)$$

$$\begin{aligned} \frac{\partial u_\theta}{\partial t} + u_r \frac{\partial u_\theta}{\partial r} + \frac{u_\theta}{r} \frac{\partial u_\theta}{\partial \theta} + u_z \frac{\partial u_\theta}{\partial z} + \frac{u_r u_\theta}{r} = \\ -\frac{1}{\rho r} \frac{\partial p}{\partial \theta} + \nu \left[ \frac{\partial^2 u_\theta}{\partial r^2} + \frac{1}{r} \frac{\partial u_\theta}{\partial r} + \frac{1}{r^2} \frac{\partial^2 u_\theta}{\partial \theta^2} + \frac{\partial^2 u_\theta}{\partial z^2} + \frac{2}{r^2} \frac{\partial u_r}{\partial \theta} - \frac{u_\theta}{r^2} \right] \end{aligned} \quad (5.3)$$

$$\begin{aligned} \frac{\partial u_z}{\partial t} + u_r \frac{\partial u_z}{\partial r} + \frac{u_\theta}{r} \frac{\partial u_z}{\partial \theta} + u_z \frac{\partial u_z}{\partial z} = \\ -\frac{1}{\rho} \frac{\partial p}{\partial z} + \nu \left[ \frac{\partial^2 u_z}{\partial r^2} + \frac{1}{r} \frac{\partial u_z}{\partial r} + \frac{1}{r^2} \frac{\partial^2 u_z}{\partial \theta^2} + \frac{\partial^2 u_z}{\partial z^2} \right] \end{aligned} \quad (5.4)$$

It is also necessary to analyze the pressure stress in the fluid and its response to shear stress in order to understand the internal torque that is developed in the fluid. The viscous torque experienced by the fluid is a measurable quantity within the experiment. In cylindrical coordinates the general stress tensor describing normal forces and shear forces on a three-dimensional parcel of fluid is

$$\sigma_{ij} = - \begin{pmatrix} \sigma_{rr} & \sigma_{r\theta} & \sigma_{rz} \\ \sigma_{\theta r} & \sigma_{\theta\theta} & \sigma_{\theta z} \\ \sigma_{zr} & \sigma_{z\theta} & \sigma_{zz} \end{pmatrix} \quad (5.5)$$

Analysis of pressure and shear stress for annular rotational Couette flow follows in Sec. 5.2.1. Results of the stress tensor analysis for annular rotational Couette flow will be used for approximations in planar rotational Couette flow and the Ekman

layer of Sec. 5.2.2. Figure 5.2 shows each of the stress tensor components in a volumetric parcel of fluid  $dr\,rd\theta\,dz$  in size. The vectors in Fig. 5.2 represent each of the normal and shear forces as  $f_i = \sigma_{ji}\partial_j$ .

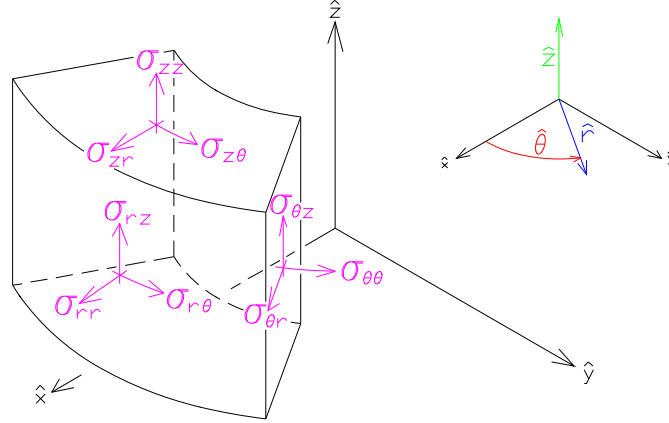


Figure 5.2: Schematic representation of a differential parcel of fluid in cylindrical coordinates showing the pressure stress and shear stress components. The vectors represent each of the normal and shear forces as  $f_i = \sigma_{ji}\partial_j$ . For reasons of clarity, the differential dimensions of the parcel,  $dr$ ,  $r d\theta$ ,  $dz$  were not included.

### 5.2.1 Annular Rotational Couette Flow

Annular rotational Couette flow is established between two coaxial cylinders where either one or both cylinders can rotate about a common longitudinal axis. There are two basic patterns of circulation which correspond to steady flow. The first circulation pattern is where the fluid tangential velocity  $u$  is proportional to radius  $r$ . This corresponds to solid-body rotation with uniform angular velocity. The second circulation pattern is where  $u$  is inversely proportional to  $r$ . This corresponds to circulation which is vorticity-free. The pattern that will be established in the experiment is the vorticity-free circulation of  $u \propto 1/r$ .

The following work for the fluid dynamic description of the annular rotational Couette flow is idealized in the sense that it does not involve any interaction with the end-walls of the annular region. This is as if the annular flow field were

of infinite length or completely decoupled from the ends. The validity of this idealized assertion will be shown when the the annular and planar flows are coupled together in the Navier-Stokes equation. For the most part, the effect of the planar rotational flow on the annular rotational flow becomes a diffusive perturbation, and the bulk of the annular rotational Couette flow will be accurately described by the following derivations. In all following discussion and derivation,  $\rho$  is the fluid density and  $\nu$  is the shear, or kinematic viscosity. The dynamic viscosity  $\mu$  is the product of  $\rho$  and  $\nu$  as  $\mu = \rho \nu$ .

In the design of the experiment, the outer and inner cylinders, of radii  $R_0$  and  $R_1$  respectively, co-directionally rotate about a common axis at tangential velocities  $u_0$  and  $u_1$ . In the experiment,  $R_1 = (1/2) R_0$  and  $u_1 = 2 u_0$ . Since  $u = \Omega r$ ,  $\Omega_1 = 4 \Omega_0$ . Figure 5.1 depicts this configuration.

It is necessary to initially solve for the tangential velocity distribution as function of radius in order to solve the pressure, shear stress, and torque distributions as functions of radius. In cylindrical coordinates, the fluid circulating about the  $z$  axis is described by the equations

$$u_\theta(r) = A r + B/r, \quad u_r = u_z = 0 \quad (5.6)$$

where  $A$  and  $B$  are constants.

The steady flow pattern where  $u \propto 1/r$ , which satisfies the no-slip boundary conditions  $u_\theta(r) = R_0 \Omega_0$  at  $r = R_0$  and  $u_\theta(r) = R_1 \Omega_1$  at  $r = R_1$ , gives the two equations to be solved as

$$\begin{aligned} u_\theta(r = R_0) &= A R_0 + B/R_0 = R_0 \Omega_0 \\ u_\theta(r = R_1) &= A R_1 + B/R_1 = R_1 \Omega_1 \end{aligned} \quad (5.7)$$

The solution for the fluid tangential velocity as a function of radius is

$$u_\theta(r) = \frac{(R_0^2 \Omega_0 - R_1^2 \Omega_1) r - R_0^2 R_1^2 (\Omega_0 - \Omega_1) r^{-1}}{R_0^2 - R_1^2}. \quad (5.8)$$



Substituting in  $R_1 = R_0/2$  and  $\Omega_1 = 4\Omega_0$  the fluid tangential velocity as a function of radius in terms of  $R_0$  and  $\Omega_0$ ,  $R_0$  and  $u_0$ ,  $R_1$  and  $\Omega_1$ , or  $R_1$  and  $u_1$  becomes

$$u_\theta(r) = \frac{R_0^2}{r}\Omega_0 = \frac{R_0}{r}u_0 = \frac{R_1^2}{r}\Omega_1 = \frac{R_1}{r}u_1 \quad (5.9)$$

From Eq. (5.2), the pressure is calculated from the pressure gradient due to centrifugal acceleration of the fluid as

$$\frac{dp}{dr} = \rho a = \rho u_\theta^2/r. \quad (5.10)$$

From Eq. (5.9)  $u_\theta(r) = u_1 R_1/r \Rightarrow u_\theta^2 = u_1^2 R_1^2/r^2$ . The pressure is calculated from the tangential velocity integrated over radius as

$$p = \rho \int_{r_1}^{r_0} \frac{u_\theta^2}{r} dr = \rho u_1^2 R_1^2 \int_{R_1}^{R_0} \frac{dr}{r^3}. \quad (5.11)$$

The solution for pressure due to annular rotational Couette flow is

$$p = -\frac{\rho u_1^2}{2} \left( \left( \frac{R_1}{R_0} \right)^2 - 1 \right) = \frac{\rho u_1^2}{2} \left( 1 - \left( \frac{R_1}{R_0} \right)^2 \right) \quad (5.12)$$

The non-zero components of the stress tensor, Eq. (5.5), are the pressure stress, described by the trace as  $\sigma_{rr}$ ,  $\sigma_{\theta\theta}$ ,  $\sigma_{zz}$ , and the viscous stress elements  $\sigma_{r\theta}$ ,  $\sigma_{\theta r}$ .

As shown below, the stress elements  $\sigma_{rr}$ ,  $\sigma_{\theta\theta}$ ,  $\sigma_{zz}$ , are equal and represent the pressure of the fluid.

$$\begin{aligned} \sigma_{rr} &= -p + 2\rho\nu\frac{\partial u_r}{\partial r} & \sigma_{\theta\theta} &= -p + \rho\nu\left(\frac{2}{r}\frac{\partial u_\theta}{\partial\theta} + \frac{2}{r}u_r\right) & \sigma_{zz} &= -p + 2\rho\nu\frac{\partial u_z}{\partial z} \\ u_r &= 0 \Rightarrow \frac{\partial u_r}{\partial r} = 0 & u_\theta &\neq \theta \Rightarrow \frac{\partial u_\theta}{\partial\theta} = 0 & u_z &= 0 \Rightarrow \frac{\partial u_z}{\partial z} = 0 \end{aligned} \quad (5.13)$$

$$\sigma_{rr} = -p \qquad \sigma_{\theta\theta} = -p \qquad \sigma_{zz} = -p$$

The significance of  $\sigma_{ii} = -p$  is the result of convention where the normal components are defined as positive when they act outward and tend to decrease the local density.

The non-zero viscous, or shear stress elements  $\sigma_{r\theta}$  and  $\sigma_{\theta r}$  are equal, otherwise there would be a net torque on the parcel of fluid. These elements are solved as

$$\begin{aligned}\sigma_{r\theta} = \sigma_{\theta r} &= \rho \nu \left[ r \frac{\partial}{\partial r} \left( \frac{u_\theta}{r} \right) + \frac{2}{r} \frac{\partial u_r}{\partial \theta} \right] \\ u_r &= 0 \Rightarrow \frac{\partial u_r}{\partial r} = 0 \\ \sigma_{r\theta} = \sigma_{\theta r} &= \rho \nu r \frac{\partial}{\partial r} \left( \frac{u_\theta}{r} \right) \\ \sigma_{r\theta} = \sigma_{\theta r} &= -2\rho \nu u_1 \frac{R_1}{r^2}\end{aligned}\tag{5.14}$$

Thus the general stress tensor describing the pressure and shear stress on the fluid in annular rotational Couette flow is

$$\sigma_{ij} = \begin{pmatrix} \rho u_1^2((R_1/R_0)^2 - 1)/2 & 2\rho \nu u_1 R_1/r^2 & 0 \\ 2\rho \nu u_1 R_1/r^2 & \rho u_1^2((R_1/R_0)^2 - 1)/2 & 0 \\ 0 & 0 & \rho u_1^2((R_1/R_0)^2 - 1)/2 \end{pmatrix}\tag{5.15}$$

In Fig. 5.2, symmetry is such that  $\sigma_{r\theta}$  must take the same value at all points about any circle upon which a point would lie. Shear stress is to be expected only when adjacent layers of fluid slide over one another. There is no shear in solid-body rotation.

Due to the shear stress, the fluid inside a cylinder of radius  $r$  experiences a viscous torque per unit length about the  $z$  axis given by

$$\begin{aligned}\vec{\tau} &= r \hat{r} \times \sigma_{r\theta} A \hat{z} \\ \vec{\tau} &= r \hat{r} \times (-2\rho \nu u_1 R_1/r^2)(2\pi r) \hat{z} \\ \vec{\tau} &= 4\pi \rho \nu u_1 R_1 \hat{\theta} = 4\pi \rho \nu u_0 R_0 \hat{\theta}\end{aligned}\tag{5.16}$$

This shows that the torque in the annular rotational flow is independent of radius, and in the rotational direction of the cylinders. This says that the gradient of torque in the annulus is zero, as is verified by the solution

$$\frac{d\tau}{dr} = 2\pi \rho \nu \frac{\partial}{\partial r} \left[ r^3 \frac{\partial}{\partial r} \left( \frac{u_\theta}{r} \right) \right] = 2\pi \rho \nu \frac{\partial}{\partial r} \left[ r^3 \frac{\partial}{\partial r} \left( \frac{u_1 R_1}{r^2} \right) \right] =$$

$$-4 \pi \rho \nu u_1 R_1 \frac{\partial}{\partial r} (1) = 0 \quad (5.17)$$

The importance of this result is twofold. This says that there is no torque in a cylindrical shell of thickness  $dr$ , thus intuitively verifying vorticity-free circulation of  $u \propto 1/r$ . Also this says that the rate of change of angular momentum is zero, as to be expected where angular momentum is constant, i.e. independent of radius. Both of these important results are proved below.

Vorticity is the curl of the velocity field:

$$\vec{w} = \nabla \times \hat{u} = \left[ \frac{1}{r} \frac{\partial u_z}{\partial \theta} - \frac{\partial u_\theta}{\partial z} \right] \hat{r} + \left[ \frac{\partial u_r}{\partial z} - \frac{\partial u_z}{\partial r} \right] \hat{\theta} + \frac{1}{r} \left[ \frac{\partial}{\partial r} (r u_\theta) - \frac{\partial u_r}{\partial \theta} \right] \hat{z} \quad (5.18)$$

All components are immediately seen to be zero except for

$$\vec{w} = \frac{1}{r} \left[ \frac{\partial}{\partial r} (r u_\theta) \right] \hat{z} \quad (5.19)$$

With  $u_\theta = u_1 R_1 / r \rightarrow r u_\theta = u_1 R_1 \Rightarrow$ , vorticity becomes

$$\vec{w} = \frac{u_1 R_1}{r} \left[ \frac{\partial}{\partial r} (1) \right] \hat{z} = 0 \quad (5.20)$$

The rate of change of angular momentum is shown to be zero by equating it to the net torque as

$$\rho r^2 \frac{\partial u_\theta}{\partial t} = \rho \nu \frac{\partial}{\partial r} \left[ r^3 \frac{\partial}{\partial r} \left( \frac{u_\theta}{r} \right) \right] = \rho \nu \frac{\partial}{\partial r} \left[ r^3 \frac{\partial}{\partial r} \left( \frac{u_1 R_1}{r^2} \right) \right] = \rho \nu u_1 R_1 \frac{\partial}{\partial r} (1) = 0 \quad (5.21)$$

### 5.2.2 Planar Rotational Couette Flow and the Ekman Layer

Planar rotational Couette flow is developed at the interface region between the  $u \propto 1/r$  annular rotational Couette flow in the annulus and the  $u \propto r$  surface of the end plates. Since the fluid velocity relative to the end-plate surface must be zero, a boundary layer develops where the fluid velocity continuously scales up from zero at the end-plate surface to the tangential fluid velocity of the

annular flow. With respect to the experiment, the Ekman layer is the boundary layer between a fluid in motion relative to a rigid surface. The differential rotation between the  $u \propto 1/r$  annular flow and the end plate causes an enhanced circulation of the fluid in the boundary layer. The relative centrifugal force between fluid in viscous contact with the end-plate and the annular flow causes a more rapid circulation of the fluid in the boundary layer than would have been the case without the centrifugal force due to the rotation of the apparatus. This secondary, forced circulation decreases the width of the boundary layer and hence enhances the fluid friction with the end plates.

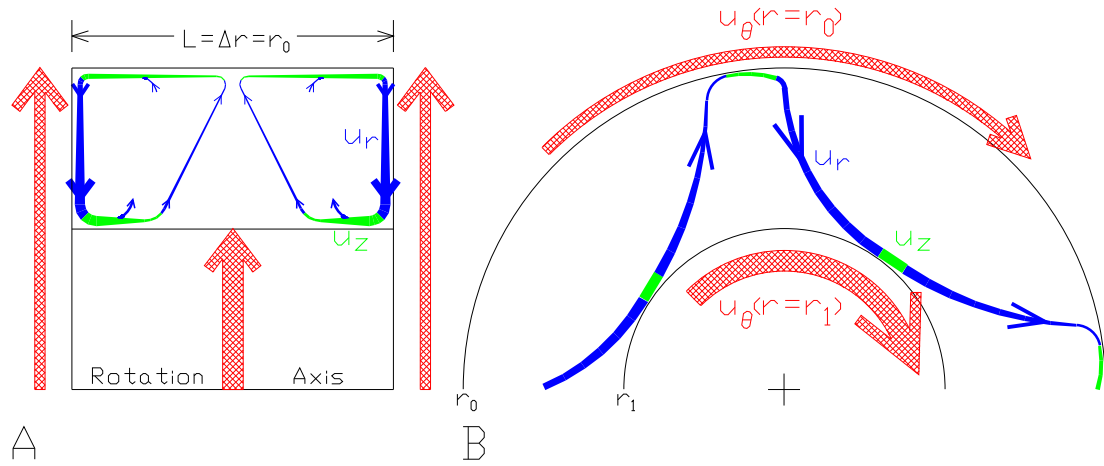


Figure 5.3: Figures 5.3(A) & 5.3(B) show side and end views respectively of the Ekman layer induced circulation in the apparatus. The relative widths of the velocity vectors  $u_r$ ,  $u_\theta$  and  $u_z$  represent the relative magnitude of each of the velocity components. It is asserted from applying continuity to mass conservation that the length over which the velocity appreciably changes in the  $z$ -direction due to influence from Ekman layer flow extends out to  $r/2$  for any radius in the annular region. It is shown from Eq. (5.33) that after the flow in the Ekman layer has progressed a distance of the order of the radius, its velocity due to the differential rotation becomes equal to half the differential rotation velocity itself. The Ekman layer thickness  $\delta$  in which  $u_r \Rightarrow u_\theta/2$  is  $\sim 1/6000$  of the radius (Eq. (5.32)).

Figure 5.3 shows a fluid with kinematic viscosity  $\nu$  rotating about the axis and bounded by the rotating end plate. There will be a boundary layer of

thickness  $\delta$ , which is a function of radius. It is assumed that the axial dimension of the flow  $\delta$ , perpendicular to the end plate, is small enough so that the radial flow parallel to the wall  $u_r$  is viscous and inertial forces can be neglected. Then the shear force per unit area of the wall due to the viscous drag on the radial flow is

$$F = \mu u_r / \delta \quad (5.22)$$

This drag force on the fluid, in the thickness  $\delta$ , corresponds to a pressure gradient within the fluid of

$$dp/dr = F/\delta = \mu u_r / \delta^2 \quad (5.23)$$

This pressure gradient must be balanced by the differential buoyancy in the fluid within the layer  $\delta$  thick. This is due to the differential rotation between the fluid in viscous contact with the end plate and the rotation within the annular flow. This buoyancy is the radial pressure gradient. Thus from Eq. (5.10)

$$dp/dr = \rho u_\theta^2 / r \quad (5.24)$$

Equating Eq. (5.23) and Eq. (5.24), the radial velocity of the flow in the Ekman layer is found to be

$$u_r = \frac{\rho u_\theta^2}{\mu} \delta^2 = \frac{u_\theta^2 \delta^2}{\nu r} \quad (5.25)$$

The following work represents an approximation for the analysis of the boundary layer thickness, and ultimately the radial flow velocity. Due to several approximations and assertions, the following work is of first order accuracy.

The boundary layer thickness  $\delta$  can be found by the relationship between convective acceleration within the layer and viscous diffusion across the layer. From Eq. (5.2), the order-of-magnitude relation is

$$O\left(u_r \frac{\partial u_r}{\partial r} \div \nu \frac{\partial^2 u_r}{\partial z^2}\right) = 1 \quad (5.26)$$

If the magnitude of the velocity in the flow field is represented by  $U$ , and the distance over which the velocity appreciably changes in the  $r$ -direction is  $L$ , then  $U^2/L$  is a measure of the magnitude of  $u_r \partial u_r / \partial r$ . Similarly,  $\nu U / \delta^2$  is a measure of the magnitude of  $\nu \partial^2 u_r / \partial z^2$ , provided  $\delta$  is a small length indicative of the boundary layer thickness. Thus Eq. (5.26) becomes

$$O\left(\frac{U^2/L}{\nu U/\delta^2}\right) = O\left(\frac{U\delta^2}{\nu L}\right) = O\left(\frac{\delta^2}{L^2} Re\right) = 1 \quad (5.27)$$

where  $Re = UL/\nu$  is the Reynolds number of the flow as a whole. The approximations improve as  $Re$  becomes very large, and as such

$$\delta \approx \frac{L}{\sqrt{Re}} = \sqrt{\frac{L\nu}{U}} \quad (5.28)$$

The dimensional size of  $L$  can be found from the shear stress in the fluid and on the end-plate surface from

$$\sigma_{z\theta} = \mu U/L \rightarrow L = \mu U/\sigma \quad (5.29)$$

Two assertions must be made to solve for  $L$  and thus ultimately for  $\delta$  and  $u_r$ . First is that  $U$ , the magnitude of the velocity in the flow field is of the order  $u_\theta$ . I have in fact chosen to use  $U = u_\theta = u_1 R_1/r$ . Second, for any radius in the annulus, the magnitude of the shear stress in the boundary-layer-influenced region is of the order of the shear stress in the annular flow at that radius. For analytical closure I have chosen to use the exact value of  $\sigma_{r\theta}$  from Eq. (5.14) for  $\sigma_{z\theta}$ . Inserting the asserted values for  $U$  and  $\sigma_{z\theta}$  into Eq. (5.29) gives

$$L = \mu \left( \frac{u_1 R_1/r}{2\mu u_1 R_1/r^2} \right) = \frac{r}{2} \quad (5.30)$$

Substituting  $L = r/2$  into Eq. (5.28),  $\delta$  is solved as

$$\delta = \sqrt{\frac{(r/2)\nu}{u_1 R_1/r}} = \sqrt{\frac{r^2 \nu}{2u_1 R_1}} = r \sqrt{\frac{\nu}{2u_1 R_1}} \quad (5.31)$$

Comparison of this result to the analysis of Prandtl (1952) is discussed in Sec. 5.3.1. Solving  $\delta(r)$  for the conditions of limiting stable Couette flow at the maximum differential rotation rates of 120 Hz & 40 Hz, where  $\nu = 10^{-2}$  cP,  $u_1 = 11,490$  cm/s, and  $R_1 = 15.24$  cm, gives

$$\delta(r = R_0) = 5.2 \times 10^{-3} \text{ cm} , \quad \delta(r = R_1) = 2.6 \times 10^{-3} \text{ cm} \quad (5.32)$$

Based on Eq. (5.31), these values represent the minimum Ekman layer thickness.

Applying continuity to mass conservation, the Ekman layer radial flow must be balanced by an axial flow near  $R_1$ . I assert that the appreciable velocity change in the  $z$ -direction is equal to that in the  $r$ -direction because of shear stress. Thus the length over which the velocity in the axial direction appreciably changes is  $Z = L = r/2$ . This says that the length over which the velocity changes in the  $z$ -direction due to influence from the boundary layer flow extends out to  $r/2$  for any radius in the annular region. This is depicted in Fig. 5.3(A). Near  $R_1$  where the azimuthal circulation from  $u_\theta$  is strongest, the effect of the Ekman layer radial flow, and the associated mass-conserving axial flow, is dominated at a distance  $z = R_1/2$ . Similarly, near  $R_0$  where  $u_\theta$  is the weakest, the effects of mass-conserving Ekman layer flow extend farther in  $z$  out to  $R_0/2$ . The apparatus is designed such that the total axial length is  $l = 2\Delta r = 2(R_0 - R_1) = 2R_1 = R_0$ . Thus the Ekman layer influence and resulting circulation will extend from each end to the center at  $r = R_0$ .

Substituting  $\delta = r \sqrt{\nu/2u_1 R_1}$  into Eq. (5.25), the radial velocity of the flow in the Ekman layer is found to be

$$u_r = \frac{(u_1 R_1/r)^2 \left( r \sqrt{\nu/2u_1 R_1} \right)^2}{\nu r} = \frac{u_1 R_1}{2r} = \frac{u_\theta}{2} \quad (5.33)$$

This means that after the flow in the Ekman layer has progressed a distance of the order of the radius, its velocity due to the differential rotation becomes equal

to half the differential rotation velocity itself. This is depicted in Fig. 5.3(B) where the width of the stream lines indicate relative velocity. This is a large flow orthogonal to the primary shear flow, but in absolute magnitude it does not significantly increase the shear velocity. However, the flow in the radial direction does make the layer thinner than would be the case without it.

The question is whether the resulting thickness of the shear layer increases the frictional dissipation significantly. This is determined by calculating the Reynolds number of the shear layer. The Reynolds number of the flow  $\delta$  wide is given by

$$Re(\delta) = \frac{u_r \delta}{\nu} = \frac{u_\theta \delta}{2\nu} = \frac{1}{2} \frac{u_1 R_1}{\nu r} r \sqrt{\frac{\nu}{2u_1 R_1}} = \frac{1}{2} \frac{u_0 R_0}{\nu r} r \sqrt{\frac{\nu}{2u_0 R_0}} = \frac{1}{2} \sqrt{\frac{u_0 R_0}{2\nu}} \quad (5.34)$$

Since the flow  $\delta$  wide is the Ekman layer flow width,  $Re(\delta) = Re_E$ . With  $R_0/2 = \Delta r = l$

$$Re_E = \frac{1}{2} \sqrt{\frac{u_0 l}{\nu}} = \frac{\sqrt{Re}}{2} \quad (5.35)$$

Thus the Reynolds number of the flow in the Ekman layer is smaller by one half of the square root of the bulk Reynolds number. For the experiment  $Re = 12.6 \times 10^6$  so that  $Re_E = 1775$ . The value of  $Re_E > 1000$  is large enough that the layer may be turbulent. The Ekman layer may then be thicker due to the increase in turbulent friction. Also the width of the layer is small enough,  $\sim 1/6000$  of the radius, so that the electrical conductivity of the Ekman flow will not distort the expected dynamo magnetic fields.

### 5.3 Annular Rotational Couette Flow and the Ekman Layer: Application to Experimental Operation

#### 5.3.1 Prediction of Torque from Ekman Layer Turbulence

Though a full analytical treatment of the Ekman layer in annular rotational Couette flow is not apparently available, the previous analysis of the Ekman



layer thickness closely agrees with that of Prandtl (1952). In the particular case of limiting stable Couette flow,  $\Omega \propto 1/r^2$  one notes that the Reynolds number calculated on the basis of a local  $r$  &  $v$  alone is constant independent of radius. This allows one therefore to make the approximation of Ekman layer thickness  $\delta$  is near constant. The analysis of Prandtl showed that  $\delta \simeq r/\sqrt{Re}$ , similar to Eq. (5.28), and within a factor of  $1/\sqrt{2}$  of Eq. (5.31) if  $u_1 R_1/\nu$  is taken as the upper limit Reynolds number.

However, in the fluid dynamic experiments, the departure from limiting stable Couette flow is the subject of the investigations and measurements. Since the inner cylinder is driven at the fixed rate of  $\Omega_1$ , and the outer cylinder is held to a lower rotation rate  $0 \leq \Omega_0 \leq \Omega_1$ , the velocity shear we have chosen to use is

$$v_{avg} = (\Omega_1 - \Omega_0)R_1 \quad (5.36)$$

We feel this velocity shear accurately represents the dynamic nature of the annular Couette flow established in the experiment due to the spectrum of  $\Omega$  ratios achieved during operation. The velocity shear, and consequently the Reynolds number, is maximum when  $\Omega_0 = 0$ , and conversely  $v_{avg} = 0$  when  $\Omega_0 = \Omega_1$ , i.e. when the apparatus is in solid body rotation.

Using the analysis of Prandtl, the estimate of the Ekman layer thickness as  $\delta = r/\sqrt{Re}$ , rather than from Eq. (5.31) will be less conservative in its estimate by  $1/\sqrt{2}$ . This would result in a slightly thicker Ekman layer, and thus possibly more turbulence in the Ekman layer flow. From Prandtl, the Ekman layer thickness is

$$\delta_{Prandtl} = \frac{r}{\sqrt{Re}} = \frac{r}{\sqrt{\frac{vl}{\nu}}} \quad (5.37)$$

Since the Ekman layer is primarily determined by the shear with the end walls near the surface of the inner cylinder, we set  $r = R_1$ ,  $v = v_{avg}$  and  $l = R_1$ .

$$\delta_{Prandtl} = \frac{R_1}{\sqrt{\frac{(\Omega_1 - \Omega_0)R_1 R_1}{\nu}}} = \sqrt{\frac{\nu}{\Omega_1 - \Omega_0}} \quad (5.38)$$

Thus  $\delta_{Prandtl}$  can be calculated as a function of only  $\Omega_0$  for fixed values of  $\Omega_1$  in the experiment.

The more conservative estimate of Ekman layer thickness can be derived from Eq. (5.31) by applying the conditions  $r = R_1$  and  $u_1 \rightarrow v_{avg}$ . Thus from the author, the Ekman layer thickness is

$$\delta_{Beckley} = \frac{R_1}{\sqrt{\frac{2(\Omega_1 - \Omega_0)R_1 R_1}{\nu}}} = \sqrt{\frac{\nu}{2(\Omega_1 - \Omega_0)}} \quad (5.39)$$

Thus, in an equivalent fashion to  $\delta_{Prandtl}$ ,  $\delta_{Beckley}$  can be calculated as a function of only  $\Omega_0$  for fixed values of  $\Omega_1$  in the experiment.

We estimate the torque from Ekman layer flow, and possible turbulence, with an approximation from Noguchi (2002). An inward radial flux,  $F_r$ , flows of order

$$F_r \simeq -\delta \rho (2\pi R_1) v_{avg} / 2 (\times 2 ends) = -\delta (2\pi R_1) (\Omega_1 - \Omega_0) R_1 g s^{-1} \quad (5.40)$$

This inward flux at both end walls toward the axis must be balanced by a slower outward radial flow throughout the central region. The Ekman flow merges with the central flow by a boundary layer at the inner cylinder surface. This results in a circulation within the Couette flow volume driven by the Ekman layers at each end. Since this flow represents a flux of angular momentum from the inner radius,  $R_1$ , to the outer radius,  $R_0$ , there must be a torque. This torque,  $\tau_{Ekman}$ , is transmitted by the fluid corresponding to the difference in the flux of angular momentum between the inner and outer surfaces. We calculate the Ekman torque as  $\tau_{Ekman} = flux \cdot velocity \cdot lever\ arm$ . Taking the absolute value of the flux, the lever arm as  $R_0 - R_1 = R_1$ , and  $\rho = 1 g\ cm^{-3}$ ,

$$\begin{aligned} \tau_{Ekman} &= \delta \rho (2\pi R_1) (\Omega_1 - \Omega_0) R_1 \cdot (\Omega_1 - \Omega_0) R_1 \cdot R_1 \\ &= \delta 2\pi R_1^4 (\Omega_1 - \Omega_0)^2\ dyne\ cm \end{aligned} \quad (5.41)$$

This calculation of Ekman layer torque as a function of  $\Omega_0$  for fixed values of  $\Omega_1$  is presented along with the data from the experiment in Chap. 6.

This torque requires weak turbulence within the so-called stable Couette flow in order to transmit this torque between  $R_1$  and  $R_0$ . Also, this torque between  $R_1$  and  $R_0$  determines the power required to drive the flow.

### 5.3.2 Prediction of Torque from Couette Flow Turbulence: An Approximation to Turbulent Pipe Flow

We approximate the possible turbulence in annular rotational Couette flow to that of axial pipe flow. This has the advantage that in our estimate of turbulent friction, we can emphasize the analogous condition of shear-driven turbulence in pipe flow. The analogy of annular rotational Couette flow to pipe flow is with regard to the boundary layer profile and turbulent shear stress. In pipe flow, the boundary layer profile follows the 'law of the walls', i.e. a logarithmic profile from the surface of the pipe wall to the bulk flow in the pipe itself. For our approximation of turbulence in annular rotational Couette flow, we assess that the boundary layer at  $R_1$  has a similar profile out to the bulk flow that has the velocity shear of Eq. (5.36). Thus, the turbulent shear stress with the inner cylinder and the bulk of the annular flow is analogous to that of pipe flow. The application of this analogy stems from the need to have an accurate coefficient of friction for turbulent shear stress for the spectrum of Reynolds numbers achieved in the experiment.

Applying the analogy of turbulent flow through pipes from AIP Handbook (2rd Ed. 1963, p. 2-250), the force due to turbulent shear stress is  $F_{turb} = 1/2 \rho v^2 C_f \cdot Area$ . The skin-friction coefficient  $C_f$  is a function of Reynolds number for smooth pipes. For  $10^5 \leq Re \leq 10^7$ ,  $6 \times 10^{-3} \geq C_f \geq 3 \times 10^{-3}$ . Since the Reynolds numbers achieved in the experiment are  $Re \simeq 10^6$ , we chose to use the fixed value of  $C_f = 0.0045$ . Taking  $\rho(H_2O) = 1 \text{ g cm}^{-3}$ , using the velocity shear

of Eq. (5.36), and the area of the inner cylinder, the force due to turbulent shear stress is

$$F_{turb} = C_f/2 (\Omega_1 - \Omega_0)^2 R_1^2 2\pi R_1 L \text{ dyne} \quad (5.42)$$

Where the length of the inner cylinder is  $L = 2R_1$

$$F_{turb} = C_f 2\pi R_1^4 (\Omega_1 - \Omega_0)^2 \text{ dyne} \quad (5.43)$$

The turbulent torque,  $\tau_{turb}$ , is cross product of the radial lever arm length and the force due to turbulent shear stress of the azimuthal circulation at the surface of the inner cylinder. The radial lever arm length is  $R_1$ , therefore

$$\tau_{turb} = R_1 \times F_{turb} = C_f 2\pi R_1^5 (\Omega_1 - \Omega_0)^2 \text{ dyne cm} \quad (5.44)$$

This calculation of turbulent shear stress torque as a function of  $\Omega_0$  for fixed values of  $\Omega_1$  is presented along with the data from the experiment in Chap. 6.

#### 5.4 Consequences of Hydrodynamic Conditions to the $\alpha\omega$ Dynamo

The fluid tangential velocity  $u$  of the annular flow field undergoing differential rotation in the experiment scales as  $1/r$ , and will be marginally stable. Thus the angular velocity  $\Omega$  should scale as  $1/r^2$ , since  $u = \Omega r$ . The angular velocity of a Keplerian disc scales as  $\Omega \propto 1/r^{3/2}$ . This difference in the flow pattern should not affect the dynamo as it is within the stable range of Couette flow. However, the shear is less;

$$\frac{d\Omega_{Kep}}{dr} = \frac{3}{4} \frac{d\Omega_{exp}}{dr} \quad (5.45)$$

We can achieve the Keplerian condition in the experiment by using the DC motor as a brake. However, with less shear the dynamo gain will be less. The experiment is optimized for maximum possible gain within the limit of power and material strengths. Reduced gain with reduced conditions can be explored later. The

increased value of angular velocity scale in the experiment helps to increase the  $\Omega$ -deformation efficiency for the poloidal to toroidal gain ratio while staying within the bounds of stable Couette flow.

## CHAPTER 6

### DATA AND ANALYSIS FROM HYDRODYNAMIC OPERATION OF THE NEW MEXICO DYNAMO EXPERIMENT

#### 6.1 Introduction

The data presented in tabular form in this chapter represent the uncorrected original values obtained during operation of the hydrodynamic experiments for determining the background torque of the experimental apparatus and the torque transmitted by the fluid. The data was obtained using digital multimeters hooked up to the stationary electronic board (Fig. 4.7(A)) and typewritten into a spreadsheet.

During differential rotation operation of the apparatus, the AC motor was used to drive the inner cylinder at a constant  $\Omega_1$  rotation rate. Table 6.1 indicates the specific gearing selected in the two transmissions for driving the intermediate shaft and electro-clutch for the 1:4 ratio serpentine drive for the high-speed shaft of the inner cylinder.

#### 6.2 Data Tables

Measured data values in Tables 6.2-6.5 are those of the Low Speed Tachometer, + Force Sensor and - Force Sensor. Low-Speed Frequency and  $\Omega_1 : \Omega_0$  Ratio values are the calculated data shown in the tables. The calibration value for the Low Speed Tachometer, as shown in the table is  $601[rpm] / 1.000[V]$ . The Low Speed Tachometer values are in units of volts [V]. Low Speed Frequency is

Table 6.1: Gear selection and rpm values for differential rotation operation of the hydrodynamic experiments. The values in bold type indicate the intermediate shaft rotation rate in revolutions per minute (rpm), as driven by the AC motor operating at 1760 rpm. The parenthetical values in bold type indicate the high-speed shaft rotation rate in rpm.

| Transmission<br>Gear | 1st           | 2nd                        | 3rd                         | 4th            |
|----------------------|---------------|----------------------------|-----------------------------|----------------|
| 1st                  | 41<br>(164)   | 83<br>(332)                | 162<br>(648)                | 275<br>(1100)  |
| 2nd                  | 85<br>(340)   | <b>174</b><br><b>(696)</b> | <b>347</b><br><b>(1388)</b> | 568<br>(2272)  |
| 3rd                  | 155<br>(620)  | 314<br>(1256)              | <b>601</b><br><b>(2404)</b> | 1050<br>(4200) |
| 4th                  | 263<br>(1052) | 533<br>(2132)              | 1035<br>(4140)              | 1760<br>(7040) |

calculated from the Low Speed Tachometer values as

$$Low\ Speed\ Frequency\ [Hz] = Low\ Speed\ Tachometer\ [V] \cdot \frac{601rpm/V}{60sec/min} \quad (6.1)$$

The  $\Omega_1 : \Omega_0$  Ratio values shown in Tables 6.3-6.5 are unitless and equivalent to frequency ratios due to the symmetric cancellation of the factors of  $2\pi$ , as  $\Omega = 2\pi f$ . Therefore the  $\Omega_1 : \Omega_0$  Ratio values are calculated from the inner cylinder frequency, where the inner cylinder frequency is its rpm divided by 60 sec/min. Thus  $\Omega_1 : \Omega_0$  Ratio values are calculated as

$$\Omega_1 : \Omega_0\ Ratio = \frac{Inner\ Cylinder\ Frequency\ [Hz]}{Low\ Speed\ Frequency\ [Hz]} \quad (6.2)$$

During all torque measurements the coaxial space between the high-speed and low-speed shafts was filled with mineral oil for bearing and seal lubrication. Hydrodynamic measurements were performed with the annular test space of the apparatus filled with deionized  $H_2O$ .

As discussed in Sec. 4.4. the torque measurement system can determine the background torque required to rotate the apparatus as a solid body through-

out the  $\Omega_0$  range. The torque measurement system can also measure the torque transmitted by the fluid by establishing differential rotation when the apparatus is empty and filled. Thus the torque measurement instrumentation provides the background drag of the rotating mass in its support bearings, including its drives, and the torque transmitted by the fluid in annular rotational Couette flow.



Table 6.2: Force measurements of solid body rotation taken with the apparatus empty and with the apparatus filled with deionized  $H_2O$ . AC motor is rotating the intermediate shaft at fixed rotation rate of 174 rpm = 2.900 Hz. The 1:4 serpentine drive belt is on and tensioned. The high-speed clutch is not engaged.

| Low Speed<br>Tachometer<br>601 [rpm]<br>$\frac{1.000[V]}{1.000[V]}$ | Low Speed<br>Frequency<br>[Hz] | + Force Sensor<br>$\frac{1000 [g]}{0.204[V]}$ | - Force Sensor<br>$\frac{1000 [g]}{0.201[V]}$ |
|---|--------------------------------|---|---|
| <b>Empty</b>  |                                |   |   |
| 0.100   | 1.002                          |   | 0.047   |
| 0.150   | 1.503                          |   | 0.057   |
| 0.200   | 2.003                          |   | 0.068   |
| 0.300   | 3.005                          |   | 0.089   |
| 0.400   | 4.007                          |   | 0.104   |
| 0.500   | 5.008                          |   | 0.116   |
| 0.600   | 6.010                          |   | 0.126   |
| 0.700   | 7.012                          |   | 0.133   |
| 0.800   | 8.013                          |   | 0.139   |
| 0.900   | 9.015                          |   | 0.144   |
| 1.000   | 10.017                         |   | 0.149   |
| <b><math>H_2O</math> Filled</b>                                     |                                |   |   |
| 0.100   | 1.002                          |   | 0.073   |
| 0.150   | 1.503                          |   | 0.085   |
| 0.200   | 2.003                          |   | 0.096   |
| 0.300   | 3.005                          |   | 0.112   |
| 0.400   | 4.007                          |   | 0.124   |
| 0.500   | 5.008                          |   | 0.133   |
| 0.600   | 6.010                          |   | 0.141   |
| 0.700   | 7.012                          |   | 0.149   |
| 0.800   | 8.013                          |   | 0.157   |
| 0.900   | 9.015                          |   | 0.164   |
| 1.000   | 10.017                         |   | 0.172   |

Table 6.3: Force measurements of differential rotation for the outer cylinder where  $\Omega_1/2\pi = 40.067$  Hz. Measurements were taken with the apparatus empty and with the apparatus filled with deionized  $H_2O$ . The AC motor is rotating the intermediate shaft at fixed rotation rate of 601 rpm = 10.017 Hz. The inner cylinder is driven via the 1:4 serpentine drive belt and rotating at 2404 rpm = 40.067 Hz.

| Low Speed<br>Tachometer<br>601 [rpm]<br>$\frac{1.000[V]}{1.000[V]}$ | Low Speed<br>Frequency<br>[Hz] | $\Omega_1 : \Omega_0$<br>Ratio | + Force Sensor<br>$\frac{1000 [g]}{0.204[V]}$ | - Force Sensor<br>$\frac{1000 [g]}{0.201[V]}$ |
|---|--------------------------------|--------------------------------|---|---|
| <b>Empty</b>  |                                |                                |   |   |
| 0.296   | 2.965                          | 13.51                          |   | 0.056   |
| 0.329   | 3.295                          | 12.16                          |   | 0.062   |
| 0.401   | 4.017                          | 9.97                           |   | 0.071   |
| 0.438   | 4.387                          | 9.13                           |   | 0.074   |
| 0.500   | 5.008                          | 8.00                           |   | 0.080   |
| 0.569   | 5.699                          | 7.03                           |   | 0.085   |
| 0.664   | 6.651                          | 6.02                           |   | 0.092   |
| 0.795   | 7.963                          | 5.03                           |   | 0.101   |
| 0.824   | 8.254                          | 4.85                           |   | 0.102   |
| 0.890   | 8.915                          | 4.49                           |   | 0.105   |
| 0.994   | 9.957                          | 4.02                           |   | 0.108   |
| <b><math>H_2O</math> Filled</b>                                     |                                |                                |   |   |
| 0.296   | 2.965                          | 13.51                          | 0.117   |   |
| 0.331   | 3.316                          | 12.08                          | 0.107   |   |
| 0.402   | 4.027                          | 9.95                           | 0.087   |   |
| 0.442   | 4.427                          | 9.05                           | 0.074   |   |
| 0.502   | 5.028                          | 7.97                           | 0.060   |   |
| 0.572   | 5.730                          | 6.99                           | 0.044   |   |
| 0.667   | 6.681                          | 6.00                           | 0.024   |   |
| 0.800   | 8.013                          | 5.00                           | 0.003   |   |
| 0.828   | 8.294                          | 4.83                           | 0.000   | 0.000   |
| 0.896   | 8.975                          | 4.46                           |   | 0.013   |
| 1.001   | 10.027                         | 4.00                           |   | 0.028   |

Table 6.4: Force measurements of differential rotation for the outer cylinder where  $\Omega_1/2\pi = 23.133$  Hz. Measurements were taken with the apparatus empty and with the apparatus filled with deionized  $H_2O$ . The AC motor is rotating the intermediate shaft at fixed rotation rate of 347 rpm = 5.783 Hz. The inner cylinder is driven via the 1:4 serpentine drive belt and rotating at 1388 rpm = 23.133 Hz.

| Low Speed<br>Tachometer<br>601 [rpm]<br>$\frac{1.000[V]}{1.000[V]}$ | Low Speed<br>Frequency<br>[Hz] | $\Omega_1 : \Omega_0$<br>Ratio | + Force Sensor<br>$\frac{1000 [g]}{0.204[V]}$ | - Force Sensor<br>$\frac{1000 [g]}{0.201[V]}$ |
|---|--------------------------------|--------------------------------|---|---|
| <b>Empty</b>  |                                |                                |   |   |
| 0.100   | 1.002                          | 23.09                          |   | 0.022   |
| 0.150   | 1.503                          | 15.39                          |   | 0.032   |
| 0.200   | 2.003                          | 11.55                          |   | 0.040   |
| 0.300   | 3.005                          | 7.70                           |   | 0.054   |
| 0.400   | 4.007                          | 5.77                           |   | 0.064   |
| 0.500   | 5.008                          | 4.62                           |   | 0.077   |
| 0.600   | 6.010                          | 3.85                           |   | 0.091   |
| 0.700   | 7.012                          | 3.30                           |   | 0.103   |
| 0.800   | 8.013                          | 2.89                           |   | 0.112   |
| 0.900   | 9.015                          | 2.57                           |   | 0.118   |
| 1.000   | 10.017                         | 2.31                           |   | 0.123   |
| 1.100   | 11.018                         | 2.10                           |   | 0.126   |
| <b><math>H_2O</math> Filled</b>                                     |                                |                                |   |   |
| 0.110   | 1.102                          | 21.00                          | 0.028   |   |
| 0.153   | 1.533                          | 15.09                          | 0.020   |   |
| 0.194   | 1.943                          | 11.91                          | 0.009   |   |
| 0.257   | 2.574                          | 8.99                           | 0.000   | 0.000   |
| 0.300   | 3.005                          | 7.70                           |   | 0.011   |
| 0.334   | 3.346                          | 6.91                           |   | 0.019   |
| 0.385   | 3.856                          | 6.00                           |   | 0.029   |
| 0.464   | 4.648                          | 4.98                           |   | 0.046   |
| 0.579   | 5.800                          | 3.99                           |   | 0.062   |
| 0.770   | 7.713                          | 3.00                           |   | 0.092   |
| 0.903   | 9.045                          | 2.56                           |   | 0.102   |
| 1.000   | 10.017                         | 2.31                           |   | 0.108   |
| 1.144   | 11.459                         | 2.02                           |   | 0.112   |

Table 6.5: Force measurements of differential rotation for the outer cylinder where  $\Omega_1/2\pi = 11.600$  Hz. Measurements were taken with the apparatus empty and with the apparatus filled with deionized  $H_2O$ . AC motor is rotating the intermediate shaft at fixed rotation rate of 174 rpm = 2.900 Hz. The inner cylinder is driven via the 1:4 serpentine drive belt and rotating at 696 rpm = 11.600 Hz.

| Low Speed<br>Tachometer<br>601 [rpm]<br>1.000[V] | Low Speed<br>Frequency<br>[Hz] | $\Omega_1 : \Omega_0$<br>Ratio | + Force Sensor<br><br>1000 [g]<br>0.204[V] | - Force Sensor<br><br>1000 [g]<br>0.201[V] |
|--|--------------------------------|--------------------------------|--|--|
| <b>Empty</b>                                     |                                |                                |  |  |
| 0.100  | 1.002                          | 11.60                          |  | 0.027                                      |
| 0.150  | 1.503                          | 7.73                           |  | 0.038                                      |
| 0.200  | 2.003                          | 5.80                           |  | 0.049                                      |
| 0.300  | 3.005                          | 3.87                           |  | 0.070                                      |
| 0.400  | 4.007                          | 2.89                           |  | 0.085                                      |
| 0.500  | 5.008                          | 2.32                           |  | 0.096                                      |
| 0.600  | 6.010                          | 1.93                           |  | 0.106                                      |
| 0.700  | 7.012                          | 1.66                           |  | 0.112                                      |
| 0.800  | 8.013                          | 1.45                           |  | 0.117                                      |
| 0.900  | 9.015                          | 1.29                           |  | 0.122                                      |
| 1.000  | 10.017                         | 1.16                           |  | 0.126                                      |
| <b><math>H_2O</math> Filled</b>                  |                                |                                |  |  |
| 0.069  | 0.691                          | 16.79                          |  | 0.004                                      |
| 0.104  | 1.002                          | 11.60                          |  | 0.011                                      |
| 0.130  | 1.302                          | 8.91                           |  | 0.018                                      |
| 0.164  | 1.643                          | 7.06                           |  | 0.028                                      |
| 0.234  | 2.344                          | 4.95                           |  | 0.048                                      |
| 0.291  | 2.915                          | 3.98                           |  | 0.060                                      |
| 0.387  | 3.877                          | 2.99                           |  | 0.081                                      |
| 0.580  | 5.810                          | 2.00                           |  | 0.103                                      |
| 0.703  | 7.042                          | 1.65                           |  | 0.112                                      |
| 0.804  | 8.053                          | 1.44                           |  | 0.117                                      |
| 0.902  | 9.035                          | 1.28                           |  | 0.123                                      |
| 1.002  | 10.037                         | 1.16                           |  | 0.126                                      |
| 1.149  | 11.509                         | 1.01                           |  | 0.131                                      |

### 6.3 Analysis of Torque Measurement Data

Calculation and graphical display of the data shown in Figs. 6.1-7 was processed using MATLAB<sup>R</sup>.

Processing the Low Speed Tachometer data was performed using Eq. (6.1). Thus the indicated frequencies for  $\Omega_0/2\pi$  [Hz] were calculated.

Processing the Force Sensor data was performed using the noted calibration factors for the (+) and (-) force sensors respectively. Initially the Force Sensor value in volts is converted to grams via the calibration factor as

$$Force\ Sensor\ Value\ [g] = Force\ Sensor\ value\ [V] \cdot Calibration\ Value\ [g]/[V] \quad (6.3)$$

The torque, in units of  $[g \cdot cm]$ , is calculated as

$$Torque\ [g \cdot cm] = Force\ Sensor\ Value\ [g] \cdot Lever\ Arm\ Length\ [cm] \quad (6.4)$$

The conversion of torque to units of  $[dyne \cdot cm]$  is performed using the conversion factor of 980.6652  $[dyne/cm]$ . Thus the calculated and displayed values of torque are

$$Torque\ [dyne \cdot cm] = Torque\ [g \cdot cm] \cdot 980.6652\ [dyne/g] \quad (6.5)$$

#### 6.3.1 Error Analysis

The primary error in the measurements of force is due to the uncertainty in the values displayed at the multimeters. The uncertainty in the values indicated at the multimeters is  $\pm 0.002$  [V]. When calculated using Eqs. (6.3-5), the error in measurement due to uncertainty is  $1.26 \times 10^6$   $[dyne \cdot cm]$  for the (+) Force Sensor and  $1.22 \times 10^6$   $[dyne \cdot cm]$  for the (-) Force Sensor, with an average value of  $1.24 \times 10^6$   $[dyne \cdot cm]$ .

The detection threshold of the force sensors is 0.001 [V/g] over a dynamic range of 1,500 [g] force. In this sense, the force sensors are considered absolute and compensated. Since the error due to uncertainty is greater than the considered detection threshold, for the data analysis presented, the detection threshold is shifted to the level of uncertainty at the value of  $1.24 \times 10^6$  [*dyne* · *cm*].

### 6.3.2 Graphical Analysis of Torque Measurement Data

Figure 6.1(A) shows torque as a function of frequency for solid body rotation. The data presented is from Table 6.2. Note that it requires more torque to rotate the apparatus when filled with  $H_2O$ . This is due to the increase of mass that the primary bearings must support. Thus there is higher kinetic friction and associated drag in the bearings and consequently more torque required to rotate the apparatus.

Figure 6.1(B) represents the background torque of the apparatus. The background torque is the difference in torque required to rotate the apparatus as a solid body when empty and when filled with  $H_2O$ . The calculated and graphically displayed measurement error bars indicate that a mean value of background torque could be justifiably calculated and applied to the forthcoming data analysis of torque transmitted by the fluid. This was not done because it is more accurate to manipulate the data before smoothing. Therefore, background torque as a function of  $\Omega_0$ , as applied to the calculated values of torque transmitted by the fluid, is the data presented in Fig. 6.1(B).

Solid body rotation measurements were made with the intermediate shaft rotating at the fixed rotation rate of 174 rpm = 2.900 Hz, the 1:4 serpentine drive belt on and tensioned, yet without the high-speed clutch engaged. This effectively accounts for most of the torque losses through bearing friction in the electro clutches and belt friction in both primary drives. When in differential

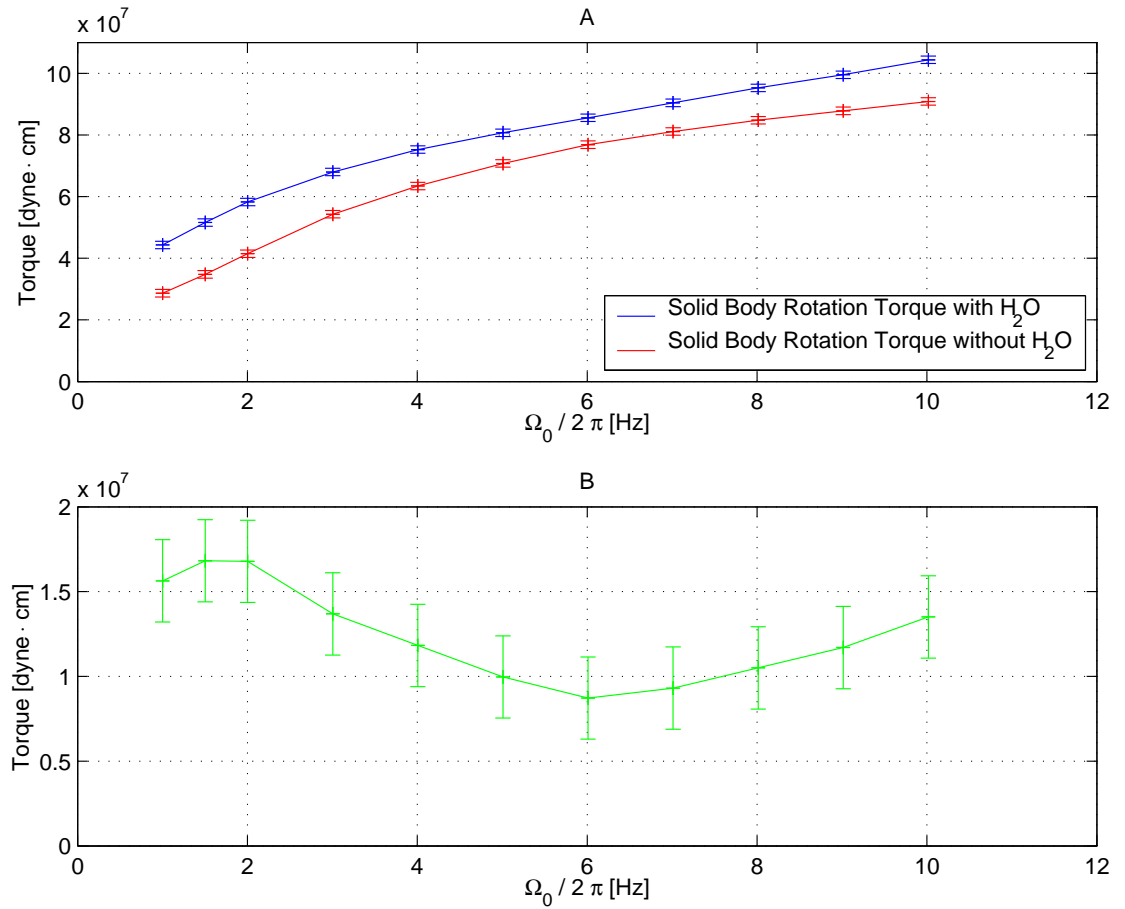


Figure 6.1: Figure 6.1(A) shows torque as a function of frequency for solid body rotation. The data presented is from Table 6.2. Note that it requires more torque to rotate the apparatus when filled with  $H_2O$ . This is due to the increase of mass that the primary bearings must support. Thus there is higher kinetic friction and associated drag in the bearings and consequently more torque required to rotate the apparatus. Figure 6.1(B) represents the background torque of the apparatus. The background torque is the difference in torque required to rotate the apparatus as a solid body when empty and when filled with  $H_2O$ .

rotation, the other sources and sinks of torque, such as outer cylinder windage and coaxial bearings and seals, are common and therefore cancel.

Figure 6.2 shows torque as a function of outer cylinder frequency for differential rotation where  $\Omega_1/2\pi = 40.067$  Hz. The data presented is from Table 6.3. Note that when the apparatus is filled with water that the torque transmitted

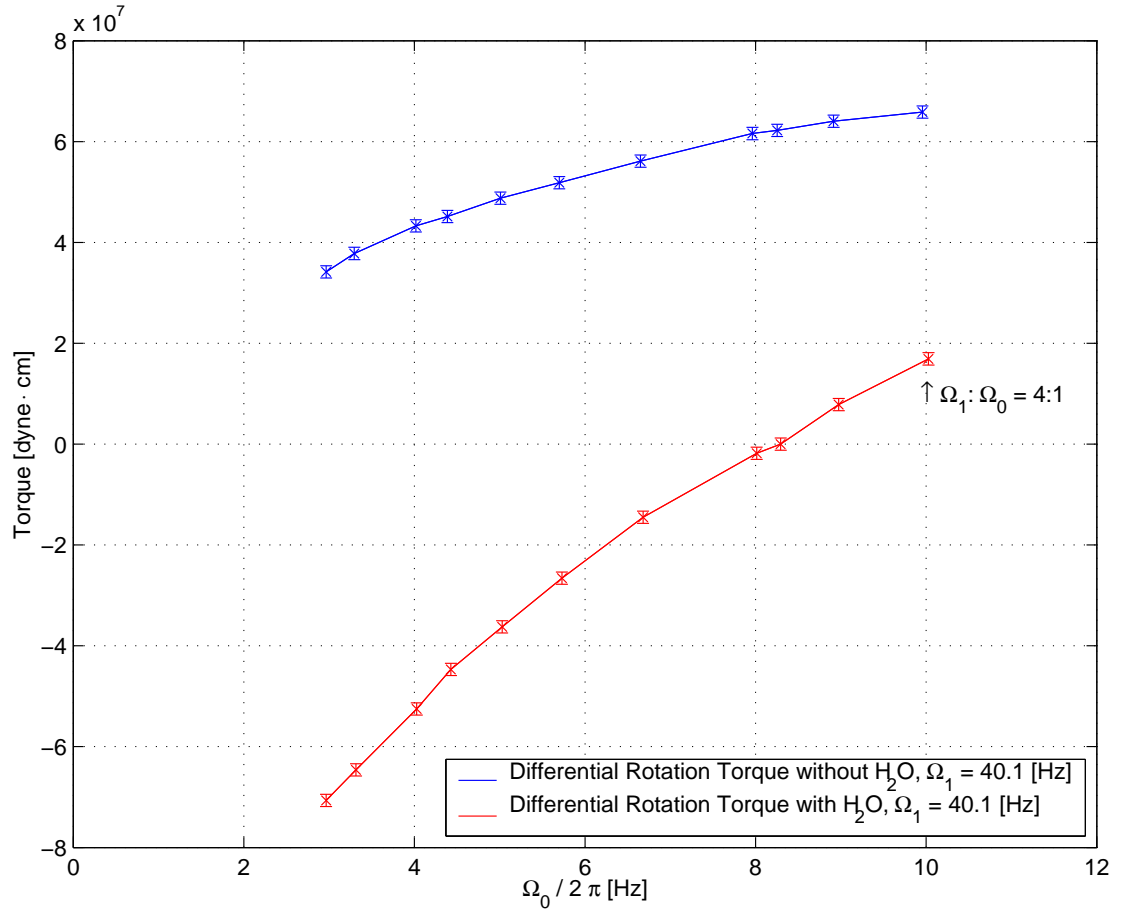


Figure 6.2: Torque as a function of outer cylinder frequency for differential rotation where  $\Omega_1/2\pi = 40.067$  Hz. The data presented is from Table 6.3. Note that when the apparatus is filled with water that the torque transmitted by the fluid is great enough to overcome the background torque requirements of the apparatus and induce outer cylinder rotation. In this case, the DC generator was utilized to control outer cylinder rotation up to the  $\Omega_1 : \Omega_0$  ratio of 4.83:1. The DC motor was used to drive the outer cylinder up to the value of limiting stable Couette flow at the  $\Omega_1 : \Omega_0$  ratio of 4:1. The region of stable annular rotational Couette flow is to the right of the point indicated by the arrow at  $\Omega_1 : \Omega_0 = 4 : 1$ .

by the fluid is great enough to overcome the background torque requirements of the apparatus and induce outer cylinder rotation. In this case, the DC generator was utilized to control outer cylinder rotation up to the  $\Omega_1 : \Omega_0$  ratio of 4.83:1. The DC motor was used to drive the outer cylinder up to the value of limiting stable Couette



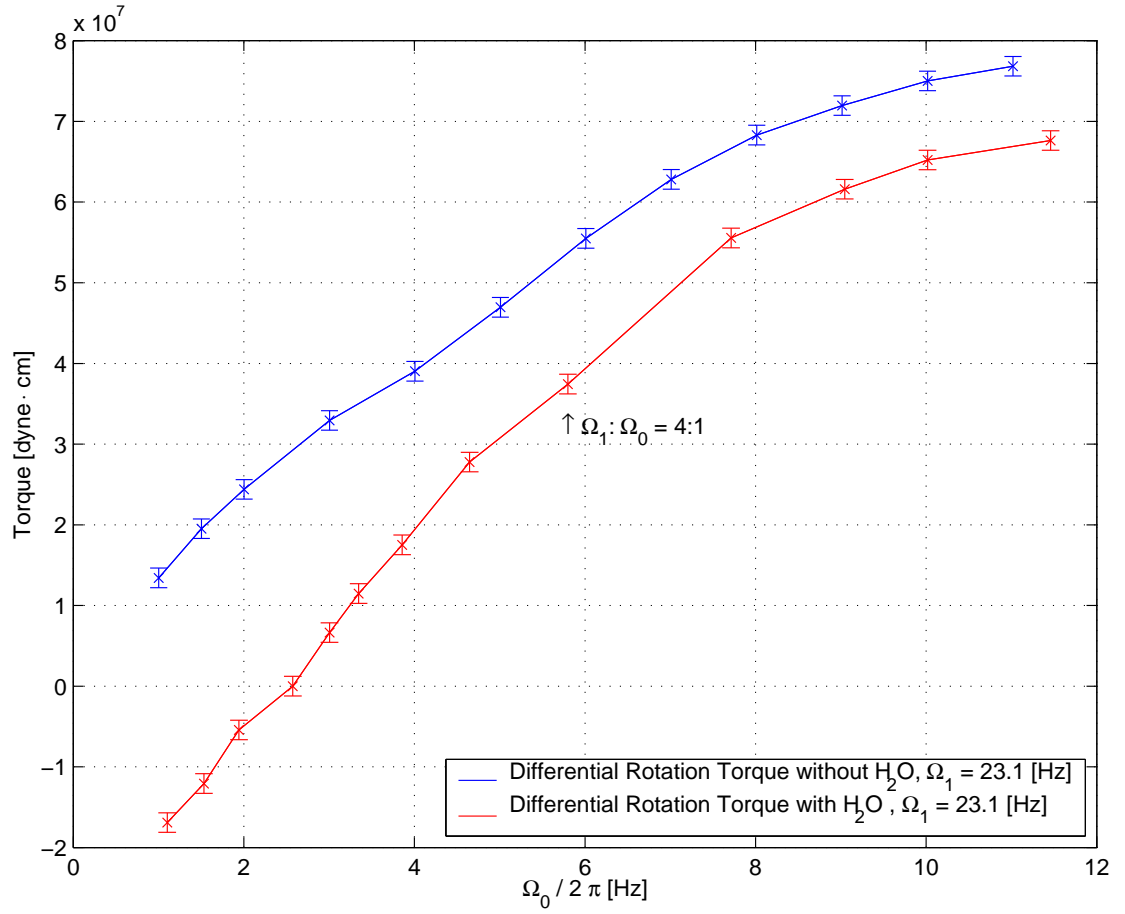


Figure 6.3: Torque as a function of outer cylinder frequency for differential rotation where  $\Omega_1/2\pi = 23.133$  Hz. The data presented is from Table 6.4. Note that when the apparatus is filled with water that the torque transmitted by the fluid is great enough to overcome the background torque requirements of the apparatus and induce outer cylinder rotation. In this case, the DC generator was utilized to control outer cylinder rotation up to the  $\Omega_1 : \Omega_0$  ratio of  $\sim 9:1$ . The DC motor was used to drive the outer cylinder up to the value of stable Couette flow at the  $\Omega_1 : \Omega_0$  ratio of  $\sim 2:1$ . The region of stable annular rotational Couette flow is to the right of the point indicated by the arrow at  $\Omega_1 : \Omega_0 = 4 : 1$ .

flow at the  $\Omega_1 : \Omega_0$  ratio of 4:1. The region of stable annular rotational Couette flow is to the right of the point indicated by the arrow at  $\Omega_1 : \Omega_0 = 4 : 1$ . Though the achievement of  $\Omega_1 : \Omega_0$  ratios further into the stability region is apparently possible given the low torque requirements at  $\Omega_1 : \Omega_0 = 4 : 1$ , doing so would have

taken the apparatus into an operational region not considered safe in the confines of the laboratory environment. Tests achieving lower  $\Omega_1 : \Omega_0$  ratios at high speed will be performed when the experiment is moved to the remote operations site.

Figure 6.3 shows torque as a function of outer cylinder frequency for differential rotation where  $\Omega_1/2\pi = 23.133$  Hz. The data presented is from Table 6.3. Note that when the apparatus is filled with water that the torque transmitted by the fluid is great enough to overcome the background torque requirements of the apparatus and induce outer cylinder rotation. In this case, the DC generator was utilized to control outer cylinder rotation up to the  $\Omega_1 : \Omega_0$  ratio of  $\sim 9:1$ . The DC motor was used to drive the outer cylinder up to the value of stable Couette flow at the  $\Omega_1 : \Omega_0$  ratio of  $\sim 2:1$ . The region of stable annular rotational Couette flow is to the right of the point indicated by the arrow at  $\Omega_1 : \Omega_0 = 4 : 1$ .

Figure 6.4 shows torque as a function of outer cylinder frequency for differential rotation where  $\Omega_1/2\pi = 11.600$  Hz. The data presented is from Table 6.5. It is apparent in Fig. 6.4 that the torque curves are converging to an equivalent value as the apparatus approaches solid body rotation. This is because the viscous drag of the internal fluid becomes zero when the angular frequency differential rotation becomes zero; i.e. when  $\Omega_0 = \Omega_1$ ,  $\Delta\Omega = 0$ . The point at which limiting stable Couette flow is occurring is indicated by the arrow at  $\Omega_1 : \Omega_0 = 4 : 1$ . Solid body rotation is indicated by the arrow at  $\Omega_1 : \Omega_0 = 1 : 1$ . At the  $\Omega_0/2\pi$  frequency of  $\sim 4$  Hz, the error due to uncertainty causes resulting calculations of torque transmitted by the fluid to come into question.

It must be noted that the apparatus was not intended to investigate Couette flow characteristics at such low speeds as indicated in Fig. 6.4. The interest in hydrodynamic investigations with the apparatus are in the higher speed and higher Reynolds number region where it will ultimately be used for magnetodynamic and magnetohydrodynamic experiments.

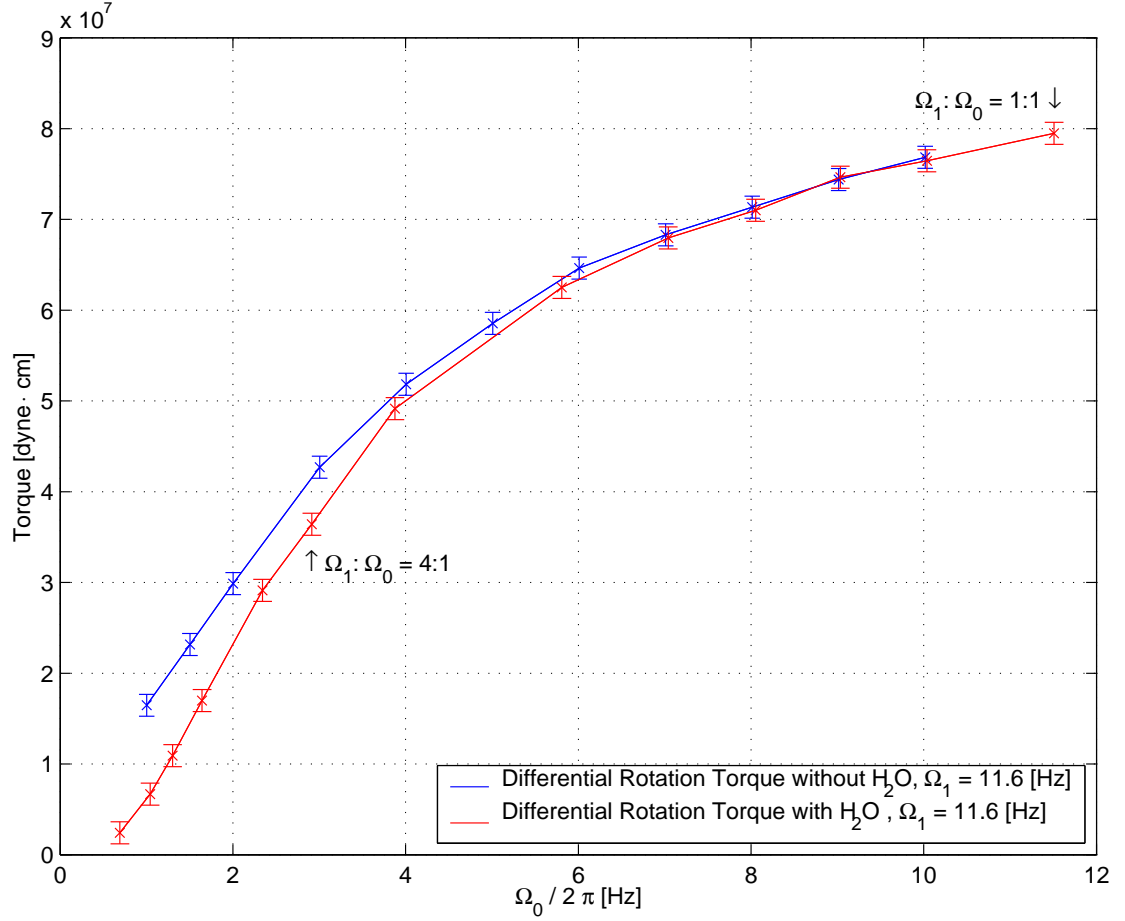


Figure 6.4: Torque as a function of outer cylinder frequency for differential rotation where  $\Omega_1/2\pi = 11.600$  Hz. The data presented is from Table 6.5. It is apparent in Fig. 6.4 that the torque curves are converging to an equivalent value as the apparatus approaches solid body rotation. This is because the viscous drag of the internal fluid becomes zero when the angular frequency differential rotation becomes zero; i.e. when  $\Omega_0 = \Omega_1$ ,  $\Delta\Omega = 0$ . The point at which limiting stable Couette flow is occurring is indicated by the arrow at  $\Omega_1 : \Omega_0 = 4 : 1$ . Solid body rotation is indicated by the arrow at  $\Omega_1 : \Omega_0 = 1 : 1$ .

#### 6.4 Analysis of Torque Transmitted by Fluid

The torque transmitted by the fluid for each of the three differential rotation cases, presented in Figs. 6.2, 6.3 and 6.4, is initially calculated as the difference in torque required to differentially rotate the apparatus when empty and filled as a function of  $\Omega_0$ . The addition to this torque value of the background torque as a function of  $\Omega_0$  is presented for each of the three cases graphically in Figs. 6.5, 6.6 and 6.7. Included in these figures are the torque curves from the theories developed in Sec. 5.3.

The hydrodynamic theories of torque from Ekman layer flow and turbulent shear stress torque are developed in Sec. 5.3. For the Ekman layer thickness, two equations were derived, Eqs. (5.38) and (5.39). Repeated here for clarity of analysis, they are

$$\delta_{Prandtl} = \frac{R_1}{\sqrt{\frac{(\Omega_1 - \Omega_0) R_1 R_1}{\nu}}} = \sqrt{\frac{\nu}{\Omega_1 - \Omega_0}} \quad (6.6)$$

$$\delta_{Beckley} = \frac{R_1}{\sqrt{\frac{2(\Omega_1 - \Omega_0) R_1 R_1}{\nu}}} = \sqrt{\frac{\nu}{2(\Omega_1 - \Omega_0)}} \quad (6.7)$$

The calculation of torque from Ekman layer flow was developed in Eq. (5.41). Repeated here in a shortened form,

$$\tau_{Ekman} = \delta \rho 2\pi R_1^4 (\Omega_1 - \Omega_0)^2 \text{ dyne cm} \quad (6.8)$$

Individually substituting Eqs. (6.6) and (6.7) for  $\delta$  into Eq. (6.8), two different curves can be calculated for torque from Ekman layer flow as a function of  $\Omega_0$  for fixed a fixed  $\Omega_1$ . These curves are presented in each of the following figures, Figs. 6.5, 6.6 and 6.7.

The calculation of turbulent shear stress torque was developed in Eq. (5.44). Repeated here in a shortened form,

$$\tau_{turb} = C_f 2\pi R_1^5 (\Omega_1 - \Omega_0)^2 \text{ dyne cm} \quad (6.9)$$

The curve for turbulent shear stress torque as a function of  $\Omega_0$  for a fixed  $\Omega_1$ , for each of the three cases, is presented in each of the following figures, Figs. 6.5, 6.6 and 6.7. Turbulent shear stress torque is presented as an extreme upper limit to the torque that could exist in a highly unstable, turbulent flow.

The Reynolds number for each of the data cases presented is calculated from  $Re = vl/\nu$  at the point of limiting stable annular rotational Couette flow. Where, from Eq. (5.36),  $v \rightarrow v_{avg}$ ,  $l \rightarrow R_1$ , and  $\nu = 1 \text{ cSt} = 1 \times 10^{-2} \text{ cm}^2 \text{ s}^{-1}$ , the Reynolds number is calculated as

$$Re = \frac{(\Omega_1 - \Omega_0)R_1 \cdot R_1}{0.01} = \frac{(\Omega_1 - \Omega_0) R_1^2}{0.01} \quad (6.10)$$

At the point of limiting stable annular rotational Couette flow,  $\Omega_1 : \Omega_0 = 4 : 1$ . Therefore  $(\Omega_1 - \Omega_0) = 3/4\Omega_1$ . Thus the Reynolds number for each of the data cases presented is

$$Re(\Omega_1/2\pi = 40.067 \text{ Hz}) = 3/4(2\pi \cdot 40.067) \cdot 15.25^2 \cdot 10^2 = 4.38 \times 10^6$$

$$Re(\Omega_1/2\pi = 23.133 \text{ Hz}) = 3/4(2\pi \cdot 23.133) \cdot 15.25^2 \cdot 10^2 = 2.54 \times 10^6$$

$$Re(\Omega_1/2\pi = 11.600 \text{ Hz}) = 3/4(2\pi \cdot 11.600) \cdot 15.25^2 \cdot 10^2 = 1.27 \times 10^6$$

Figure 6.5 shows the torque transmitted by fluid as a function of  $\Omega_0$  for differential rotation where  $\Omega_1/2\pi = 40.067 \text{ Hz}$ . The data presented is from Table 6.3 and Fig. 6.2. The torque transmitted by the fluid (+) represents the difference between the torque required rotate the outer cylinder, as a function of  $\Omega_0$ , when the apparatus is empty and full, plus the background torque as a function of  $\Omega_0$ . The point of limiting stable Couette flow is indicated by the arrow at  $\Omega_1 : \Omega_0 = 4 : 1$ . The region of unstable Couette flow is to the left of this point, and the stable Couette flow region, up to  $\Omega_1 : \Omega_0 = 1 : 1$ , is to the right of this point. Note that the trend in the data indicates decreasing instability, i.e. increasing stability as the annular rotational Couette flow profile approaches limiting stable Couette

flow. This is the singular most important hydrodynamic result from operation of the experiment. The fluid Reynolds number at the point  $\Omega_1 : \Omega_0 = 4 : 1$  is  $4.4 \times 10^6$ .

Figure 6.6 shows the torque transmitted by fluid as a function of outer cylinder frequency for differential rotation where  $\Omega_1/2\pi = 23.133$  Hz. The data presented is from Table 6.4 and Fig. 6.3. The torque transmitted by the fluid (+) represents the difference between the torque required rotate the outer cylinder, as a function of  $\Omega_0$ , when the apparatus is empty and full, plus the background torque as a function of  $\Omega_0$ . The point of limiting stable Couette flow is indicated by the arrow at  $\Omega_1 : \Omega_0 = 4 : 1$ . The region of unstable Couette flow is to the left of this point, and the stable Couette flow region, up to  $\Omega_1 : \Omega_0 = 1 : 1$ , is to the right of this point. Note that the general trend in the data indicates increasing stability as the annular rotational Couette flow profile approaches limiting stable Couette flow and passes into the stable Couette flow region. The slight divergence of the data from continued stability as  $\Omega_1 : \Omega_0$  ratios approach 2:1 is not understood at this time.

Figure 6.7 shows the torque transmitted by fluid as a function of outer cylinder frequency for differential rotation where  $\Omega_1/2\pi = 11.600$  Hz. The data presented is from Table 6.5 and Fig. 6.4. The torque transmitted by the fluid (x) represents the difference between the torque required rotate the outer cylinder, as a function of  $\Omega_0$ , when the apparatus is empty and full, plus the background torque as a function of  $\Omega_0$ . The region of stable Couette flow is between the arrow at  $\Omega_1 : \Omega_0 = 4 : 1$  and the arrow at  $\Omega_1 : \Omega_0 = 1 : 1$ . The divergence of the data from the theoretical curves indicates that the apparatus and/or the sensor system used is not well suited to investigate Couette flow characteristics at such low speeds and Reynolds number.

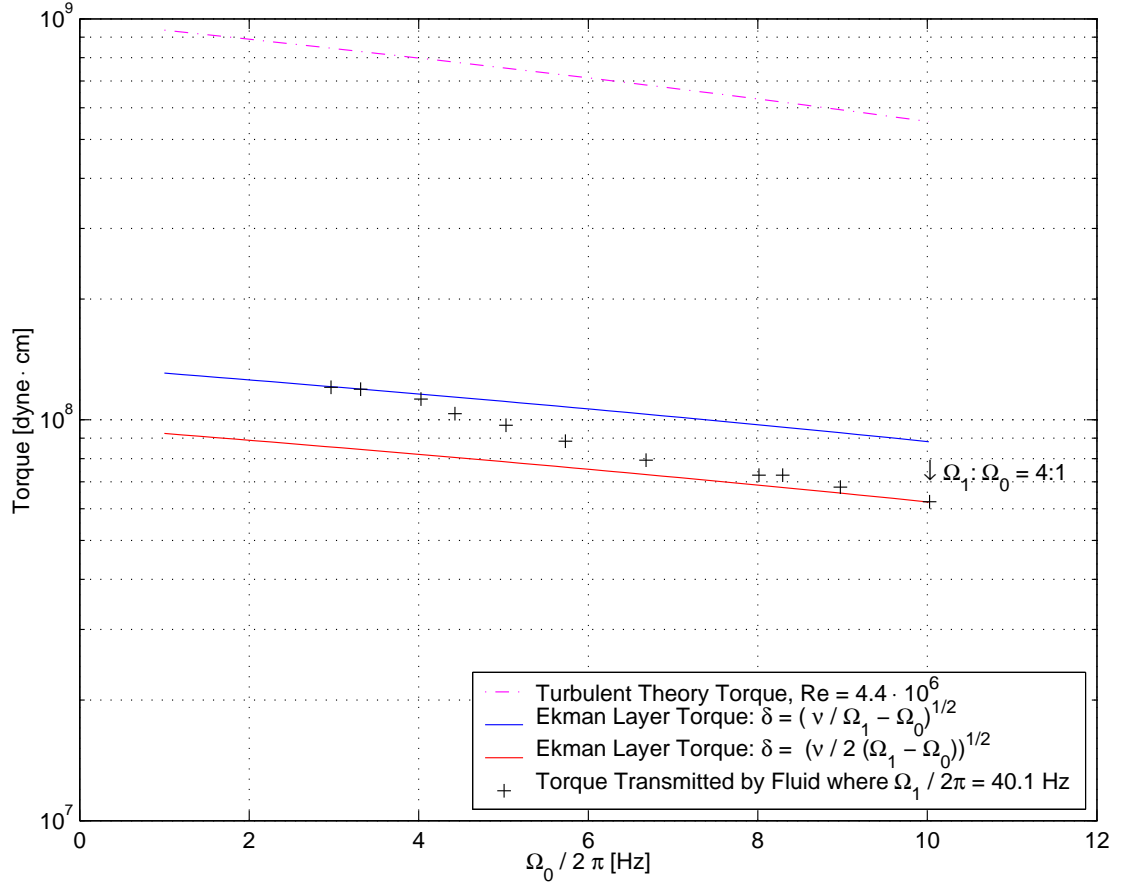


Figure 6.5: Torque transmitted by fluid as a function of outer cylinder frequency for differential rotation where  $\Omega_1/2\pi = 40.067$  Hz. The data presented is from Table 6.3 and Fig. 6.2. The torque transmitted by the fluid (+) represents the difference between the torque required rotate the outer cylinder, as a function of  $\Omega_0$ , when the apparatus is empty and full, plus the background torque as a function of  $\Omega_0$ . The turbulent theory torque curve is calculated from Eq. (6.9) where turbulent shear stress torque is calculated as a function of  $\Omega_0$ . The two Ekman layer torque curves are calculated from Eq. (6.8) where Ekman layer torque is calculated as a function of  $\delta$ , the Ekman layer thickness, and  $\Omega_0$ . The two equations for  $\delta$  as a function of  $\Omega_0$  are Eqs. (6.6) and (6.7). The point of limiting stable Couette flow is indicated by the arrow at  $\Omega_1 : \Omega_0 = 4 : 1$ . The region of unstable Couette flow is to the left of this point, and the stable Couette flow region, up to  $\Omega_1 : \Omega_0 = 1 : 1$ , is to the right of this point. Note that the trend in the data indicates decreasing instability, i.e. increasing stability as the annular rotational Couette flow profile approaches limiting stable Couette flow.

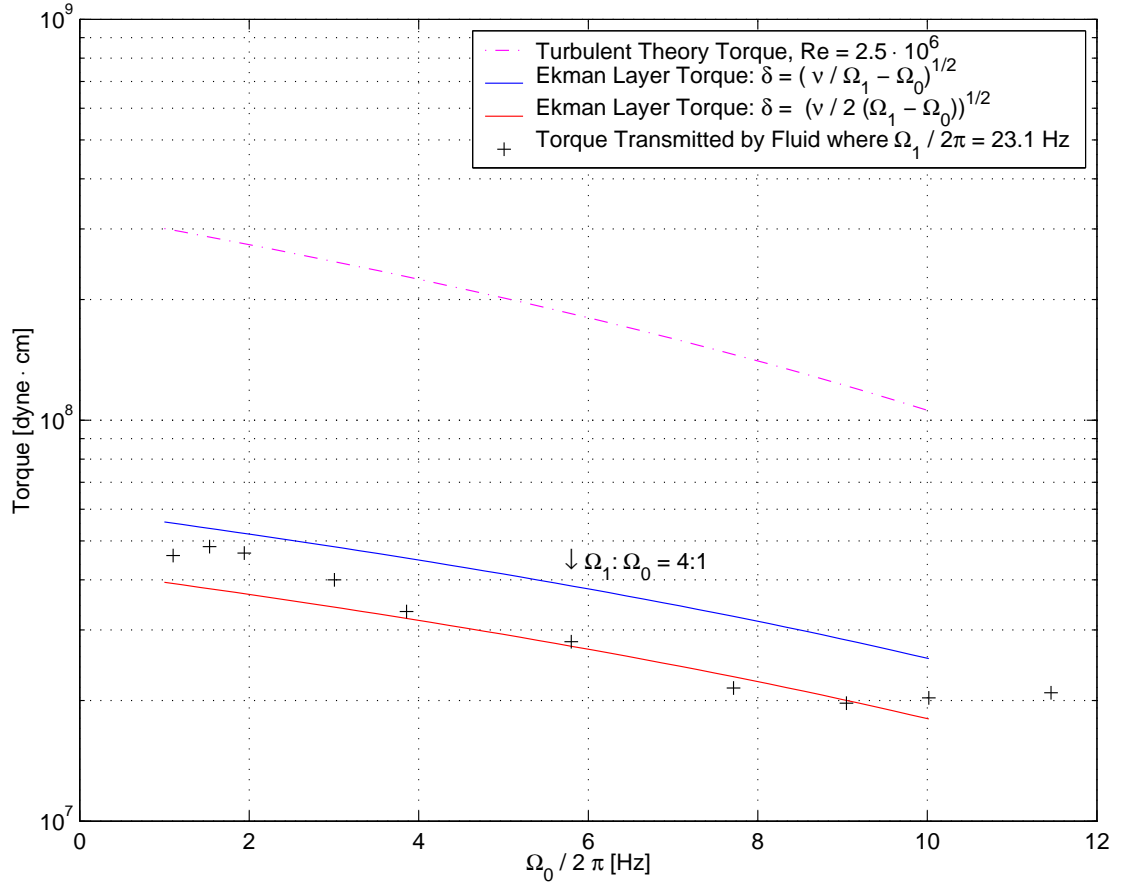


Figure 6.6: Torque transmitted by fluid as a function of outer cylinder frequency for differential rotation where  $\Omega_1/2\pi = 23.133$  Hz. The data presented is from Table 6.4 and Fig. 6.3. The torque transmitted by the fluid (+) represents the difference between the torque required rotate the outer cylinder, as a function of  $\Omega_0$ , when the apparatus is empty and full, plus the background torque as a function of  $\Omega_0$ . The turbulent theory torque curve is calculated from Eq. (6.9) where turbulent shear stress torque is calculated as a function of  $\Omega_0$ . The two Ekman layer torque curves are calculated from Eq. (6.8) where Ekman layer torque is calculated as a function of  $\delta$ , the Ekman layer thickness, and  $\Omega_0$ . The two equations for  $\delta$  as a function of  $\Omega_0$  are Eqs. (6.6) and (6.7). The point of limiting stable Couette flow is indicated by the arrow at  $\Omega_1 : \Omega_0 = 4 : 1$ . The region of unstable Couette flow is to the left of this point, and the stable Couette flow region, up to  $\Omega_1 : \Omega_0 = 1 : 1$ , is to the right of this point. Note that the general trend in the data indicates increasing stability as the annular rotational Couette flow profile approaches limiting stable Couette flow and passes into the stable Couette flow region. The slight divergence of the data from continued stability as  $\Omega_1 : \Omega_0$  ratios approach 2:1 is not understood at this time.



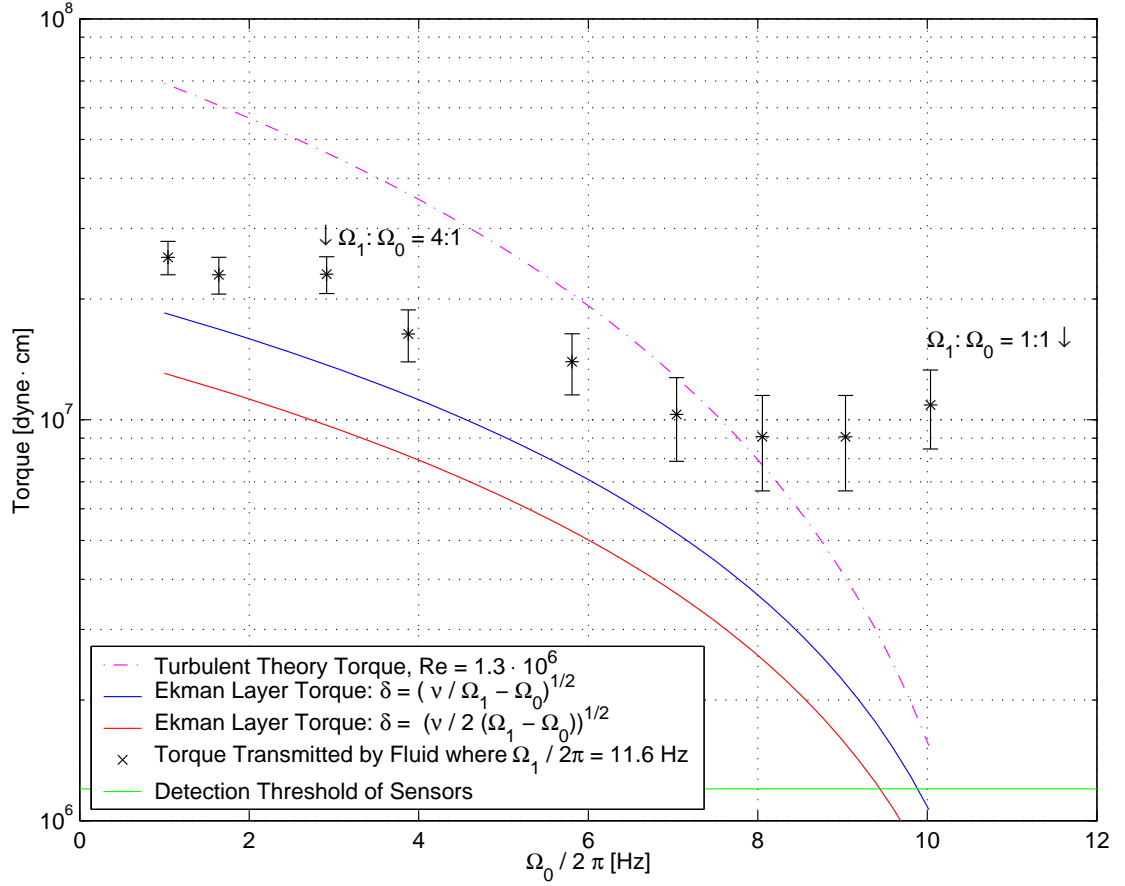


Figure 6.7: Torque transmitted by fluid as a function of outer cylinder frequency for differential rotation where  $\Omega_1/2\pi = 11.600$  Hz. The data presented is from Table 6.5 and Fig. 6.4. The torque transmitted by the fluid (x) represents the difference between the torque required rotate the outer cylinder, as a function of  $\Omega_0$ , when the apparatus is empty and full, plus the background torque as a function of  $\Omega_0$ . The turbulent theory torque curve is calculated from Eq. (6.9) where turbulent shear stress torque is calculated as a function of  $\Omega_0$ . The two Ekman layer torque curves are calculated from Eq. (6.8) where Ekman layer torque is calculated as a function of  $\delta$ , the Ekman layer thickness, and  $\Omega_0$ . The two equations for  $\delta$  as a function of  $\Omega_0$  are Eqs. (6.6) and (6.7). The point of limiting stable Couette flow is indicated by the arrow at  $\Omega_1 : \Omega_0 = 4 : 1$ . The region of stable Couette flow is between the arrow at  $\Omega_1 : \Omega_0 = 4 : 1$  and the arrow at  $\Omega_1 : \Omega_0 = 1 : 1$ . The divergence of the data from the theoretical curves indicates that the apparatus and/or the sensor system used is not well suited to investigate Couette flow characteristics at such low speeds and Reynolds number.

## 6.5 Conclusions

Analysis of the data indicates torques comparable to what are predicted for Ekman layer flow in annular rotational Couette flow at high rotation rates, and consequently high Reynolds number. The contribution to the transport of angular momentum due to turbulence in Couette flow appears to be relatively small. The decrease in torque toward limiting stable Couette flow is particularly evidenced in the data and graphical analysis of differential rotation where  $\Omega_1/2\pi = 40.067$  Hz and  $Re = 4.4 \times 10^6$ . Though the other cases presented were less definitive in their respective results, the general trend of the torque data indicates stability of the differentially rotating flows approaching limiting stable Couette flow.

The preceding analysis and results of hydrodynamic operation and characterization of the apparatus has to be understood within the context of the proposed experimental operation as an  $\alpha\omega$  dynamo. There will be continued hydrodynamic and fluid dynamic analysis performed at higher rotation rates, including the design limit of 120 Hz and 40 Hz for the inner and outer cylinders respectively. The hydrodynamic operation at the design limit will effectively conclude the experiments with the torque measurement equipment. When experimental operation begins for investigations involving the  $\omega$ -deformation, the rotational power and torque will be provided by the AC motor alone via the two electro clutches and primary belt drives. This configuration has the set  $\Omega_1 : \Omega_0$  ratio of 4:1, i.e. limiting stable Couette flow profile.

The results discussed allow confidence in predictions to be made in terms of the torque, and ultimately the power required to operate the apparatus at its design limit.

The data points at  $\Omega_1 : \Omega_0 = 4 : 1$ , representing limiting stable Couette flow, presented in Figs. 6.5 and 6.6 are consistent with Ekman layer torque at the Ekman layer thickness  $\delta_{Beckley}$ . From this basis, predictions are made of torque

and power at higher rotation rates and Reynolds number. From Eq. (6.8), the predicted torque in Ekman layer flow is

$$\begin{aligned}\tau_{Ekman}(Beckley) &= \delta_{Beckley} \rho 2\pi R_1^4 (\Omega_1 - \Omega_0)^2 = \sqrt{\frac{\nu}{2(3/4\Omega_1)}} 2\rho\pi R_1^4 (3/4\Omega_1)^2 \\ &= \sqrt{2\nu} \rho \pi R_1^4 (3/4\Omega_1)^{3/2} \quad (6.11)\end{aligned}$$

Substituting the limiting rotational frequency of  $\Omega_1 = 2\pi \cdot 120$  Hz into Eq. (6.11),  $\tau_{Ekman}(Beckley)$  is solved as

$$\begin{aligned}\tau_{Ekman}(Beckley) &= \sqrt{2\nu} \rho \pi R_1^4 (3/4(2\pi 120))^{3/2} \\ &= \sqrt{2\nu} \rho \pi 15.25^4 (180\pi)^{3/2} = 3.23 \times 10^8 \text{ dyne cm}\end{aligned}$$

The power required to drive the apparatus at this level of torque is

$$\begin{aligned}\dot{W}(Beckley) &= \tau_{Ekman} \cdot \Omega_1 = 3.23 \times 10^8 \cdot 240\pi \\ &= 2.44 \times 10^{11} \text{ dyne cm s}^{-1} = 24.4 \text{ kW}\end{aligned}$$

In this case the power requirement is  $\sim 1/2$  the available power from the 50 kW AC motor.

The difference in Ekman layer thickness, Ekman layer torque, and ultimately the power required when using  $\delta_{Prandtl}$  (Eq. (6.6)) is different by a factor of  $\sqrt{2}$ . Thus the torque and power would be

$$\begin{aligned}\tau_{Ekman}(Prandtl) &= 4.57 \times 10^8 \text{ dyne cm}, \\ \dot{W}(Prandtl) &= 34.4 \text{ kW}\end{aligned}$$

For the  $\omega$ -deformation magnetodynamic experiments, liquid sodium will be used as the electrically conducting fluid. At the operating temperature of the experiments,  $\sim 110$  C, liquid sodium has the same kinematic viscosity as water and has a density of  $0.92 \text{ g/cm}^3$ . For Ekman layer flow torque considerations, this linearly translates to 92% of the above calculated values.

For  $\omega$ -deformation experiments, a quadrupole (poloidal) magnetic field will be applied to the apparatus, and consequently the liquid sodium. The  $\omega$ -deformation experiments are designed to investigate the topological change of the magnetic field from poloidal to toroidal. The differentially rotating liquid sodium flow will have a resistive torque due to the magnetic field pressure from the differential winding of the applied field. The strength of the applied field will vary based upon the test parameters chosen. A reasonable upper limit of  $10^2$  Gauss will be assumed. The torque in the fluid due to the magnetic field pressure parallel to the flow can be calculated as a dimensional estimate for the magnetic stress torque.

$$\begin{aligned}\tau_{magnetic} &= \textit{Tangential Force} \times \textit{Differential Volume} \times \textit{Lever Arm} \\ &= (P_{magnetic}/(2\pi R/N)) \times (R)(L)(\Delta R) \times R\end{aligned}\quad (6.12)$$

The tangential force is the magnetic field pressure divided by the circumferential length within the annulus per winding number turn of the magnetic field. In cgs units, the magnetic field pressure is  $B^2/8\pi$ . The number of turns,  $N_\omega$ , is the multiplication factor for the topological change of poloidal to toroidal field where  $B_{toroidal}/B_{poloidal} = N_\omega B_{poloidal}$ . This factor  $N_\omega$  is proportional to the magnetic Reynolds number, where  $N_\omega = Rm_\omega/2\pi$ . From Eq. (4.3) the magnetic Reynolds number was calculated to be  $Rm_\omega \simeq 120$ . Therefore  $N_\omega \simeq 19$ . The differential radius,  $\Delta R$  is calculated from the square root of the magnetic diffusion coefficient divided by  $\Omega$ . Thus  $\Delta R = (749 \text{ cm}^2 \text{ s}^{-1}/753 \text{ radians s}^{-1})^{1/2} \simeq 1 \text{ cm}$ . Therefore the estimate for the magnetic stress torque is

$$\tau_{magnetic} = (B^2/16\pi^2) N_\omega R 2R \Delta R = (10^4/160) 19 \cdot 30 \cdot 30 \cdot 1 = 10^6 \text{ dyne cm} \quad (6.13)$$

Thus the magnetic stress torque in the dynamo apparatus  $\sim 10^{-2}$  that of the Ekman layer torque.

The fluid dynamic results and the magnetodynamic analysis show that the experimental dynamo apparatus is well suited to investigate the  $\omega$ -deformation component of the  $\alpha\omega$  dynamo.

## CHAPTER 7

### SUMMARY AND CONCLUSIONS

This dissertation has been presented as the result of the design, development, construction, and fluid dynamic operation of an experimental liquid sodium  $\alpha\omega$  dynamo. The culmination of this work is the laboratory operation of the dynamo apparatus that tests and verifies the operation of the rotating experiment and the ability of the apparatus to create and sustain stable annular Couette flow at very high Reynolds number. The data reported in this dissertation approaches the last laboratory engineering phase and is the first phase of scientific operation of the dynamo apparatus.

The apparatus is designed to withstand the mechanical stress of differential rotation frequencies at 120 Hz and 30 Hz for the inner and outer cylinders respectively. The maximum stress induced by the pressure of the differentially rotating fluid at the maximum rate condition is 72 atm. During part of the engineering test phase the apparatus was successfully hydrostatically pressure tested to 24 atm, or 1/3 of the maximum pressure stress. This 1/3 value value of the maximum pressure stress was chosen so that it would intentionally coincide with the predetermined upper limit of safe rotation frequencies that could be achieved in the laboratory. The imposed upper limit was 10% of the maximum yield stress of the rotating mass of the apparatus. This translates to 1/3 the maximum differential rotation velocity, since  $\Omega \propto v$ . In the laboratory tests, operating at the limiting rotation frequencies of 40 Hz and 10 Hz, there were no indications of any mechanical, material, or other problems with the experimental apparatus or subsystems.

In the laboratory tests, using the limiting rotation frequencies of 40 Hz and 10 Hz, the resulting maximum Reynolds number for the annular Couette flow was  $\text{Re}_{H_2O} = 4.4 \times 10^6$ . The importance of this result is that it is significantly greater than previous values of similar flow configurations by a factor of 20. Efforts were made to acquire reliable torque and power data reported in this dissertation. Subsequent error analysis of the data and comparison to hydrodynamic theory provide evidence, as predicted, that the annular Couette flow in the dynamo apparatus was stable at  $\text{Re} = 4.4 \times 10^6$ .

The impetus for this project has been to build an experiment that could simulate one of the possible types of dynamo processes of magnetic field creation and sustainment believed to operate in nature. The basis of the present design of the liquid sodium  $\alpha\omega$  dynamo I have built, tested and operated is to create an apparatus that can differentially rotate a stable annular flow of liquid sodium. Subsequently we may add to the apparatus the injection of axially-aligned periodic plumes within the annulus. Differential rotation results in the magnetodynamic effect of the  $\omega$ -deformation, and the  $\alpha$ -helicity is the magnetohydrodynamic effect of the non-axisymmetric, axially-aligned plumes. With these two flows an  $\alpha\omega$  dynamo can be investigated. The fluid dynamic results and the magnetodynamic analysis discussed in this dissertation show that the experimental apparatus is well suited to creating and analyzing the requisite fluid flow fields for the  $\omega$ -deformation component of the  $\alpha\omega$  dynamo.

## REFERENCES

- American Institute of Physics Handbook, 3rd Ed.*, 1972, [McGraw Hill, New York], 2, p. 269
- American Institute of Physics Handbook, 2nd Ed.*, 1963, [McGraw Hill, New York], 2, p. 250
- Batchelor, G.K., 1999, "An Introduction to Fluid Dynamics" Cambridge Univ. Press
- Batchelor, G. K., 1954, Heat Convection and Buoyancy Effects in Fluids, *Quart. J. R. Met. Soc.*, 80, 339
- Böhm-Vitense, E., 1958, *Z. Astrophys.*, 46, 108
- Boussinesq, J., 1903, *Théorie Analytique de la Chaleur* [Gauthier-Villars, Paris, France], vol. 1, p. 172
- Busse, F.H., Müller, U., Stieglitz, R., & Tilgner, A., "A Two-scale Homogeneous Dynamo: An Extended Analytical Model and Experimental Demonstration Under Development", *Magnitnaya Gidrodinamika*, T.32, 259-271 (1996).
- Canuto, V. M., Goldman, I. & Mazzitelli, I., 1996, Stellar Turbulent Convection: A Self-consistent Model, *Astrophys. J.*, 473, 550
- Cattaneo, F., Brummell, N. H., Toomre, J., Malagoli, A. & Hurlburt, N. E., 1991, Turbulent Compressible Convection, *Astrophys. J.*, 370, 282
- Chan, K. L. & Sofia, S., 1989, Turbulent Compressible Convection in a Deep Atmosphere .4. Results of 3-Dimensional Computations, *Astrophys. J.*, 336, 1022
- Chan, K. L. & Sofia, S., 1987, Validity Tests of the Mixing-Length Theory of Deep Convection, *Science*, 235, 465
- Chandrasekhar, S., 1961 *Hydrodynamic and Hydromagnetic Stability*, [Clarendon Press, Oxford]
- Churchill, S., 1988 *Viscous Flows; The Practical Use of Theory*, [Butterworths, Boston]
- Colgate, S. A., Li, H. & Pariev, V. I., 2001, The Origin of the Magnetic Fields of the Universe: The Plasma Astrophysics of the Free Energy of the Universe, *Physics of Plasmas*, vol. 8, pp. 2425-2431

- Colgate, S. A., Herant, M. H. & Willet, G., 2000, A Model of Plume Convection, (In Preparation)
- Colgate, S. A. & Li, H., 1999, Dynamo Dominated Accretion and Energy Flow: The Mechanism of Active Galactic Nuclei, *Astrophys. Space Sci.*, 264, 357
- Colgate, S. A. & Li, H., 1997, The Galactic Dynamo, The Helical Force-Free Field, and The Emissions of AGN, in *Proc. of the Conference on Relativistic Jets in AGN*, Cracow, Poland, ed. Ostrowski, Sikora, Madejski & Begelman, pp. 170-179
- Colgate, S. A., 1994, Acceleration in Astrophysics, *Physica Scripta*, T52, pp. 96-105
- Colgate, S. A., 1978, A Phenomenological Model of Solar Flares, *Astrophys. J.*, 221, 1068
- Colgate, S. A., Furth, H. P. & Halliday, F. O., 1960, Hydromagnetic Equilibrium Experiment with Liquid and Solid Sodium *Reviews of Modern Physics*, vol. 32, p. 744
- Colgate, S.A., “Liquid-sodium instability experiment”, UCRL 4560 (1955).
- Cowling, T. G., 1981, The Present Status of Dynamo Theory, *Ann. Rev. Astrophys.*, vol. 19, p. 115
- Cowling, T. G., 1934, *Mon. Not. R. Astron. Soc. London*, 94, 39
- Fernando, H. J. S., Chen, R. R. & Ayotte, B. A., 1998, Development of a Point Plume in the Presence of Background Rotation, *Phys. Fluids*, 10, 2369
- Ferrière, K., 1994, Spiral Galaxies: A Dynamo with a Difference, *Nature*, 368, 403
- Ferrière, K., 1993, The Full alpha-tensor Due to Supernova Explosions and Superbubbles in the Galactic Disc, *Astrophys. J.*, vol. 404, pp. 162–184
- Ferrière, K., 1993, Magnetic Diffusion Due to Supernova Explosions and Superbubbles in the Galactic Disk, *Astrophys. J.*, vol. 409, pp. 248–261
- Ferrière, K., 1992, Effect of the Explosion of Supernovae and Superbubbles on the Galactic Dynamo, *Astrophys. J.*, vol. 391, pp. 188–198
- Gailitis, A., Lielausis, O. & Platacis, E., 2001, Magnetic Field Saturation in the Riga Dynamo Experiment, *Phys. Rev. Lett.*, vol. 86, pp. 3024–3027
- Gailitis, A., Lielausis, O., Dement’ev, S., Platacis, E., Cifersons, A., et al., 2000, Detection of a Flow Induced Magnetic Field Eigenmode in the Riga Dynamo Facility, *Phys. Rev. Lett.*, 84, pp. 4365-4368



- Hossain, M. & D. J. Mullan, 1993, Simulation of Compressible Convection: A Comparative-Study of Boundary-Conditions, *Astrophys. J.*, 416, 733
- Hughes, W. & Brighton, J., 1991, *Schaum's Outline of Theory and Problems of Fluid Dynamics* [McGraw-Hill, New York]
- Hurlburt, N. E., Toomre, J., Massaguer, J. M. & Zahn, J. P., 1994, Penetration Below a Convective Zone, *Astrophys. J.*, 421, 245
- Landau, L. D. & Lifschitz, E. M., 1988, *Hydrodynamics*, [Nauka, Moscow]
- Landau, L. D. & Lifschitz, E. M., 1959, *Fluid Dynamics*, [Pergamon Press, London], p. 107
- Lavelle, J. W., 1997, Buoyancy-driven Plumes in Rotating, Stratified Cross Flows: Plume Dependence on Rotation, Turbulent Mixing, and Cross-flow Strength, *J. Geophys. Res.*, 102, pp. 3405-3420
- Lo, Y. C. & Schatzman, E., 1997, Dynamical Model of Convection in Stellar Cores, *Astron. Astrophys.*, 322, 545
- Merzkirch, W., 1987, *Flow Visualization*, [Academic Press, Orlando]
- Mestel, L., 1999, *Stellar Magnetism*, [Clarendon Press, Oxford]
- Moore, D.W., 1967, *Aerodynamic Phenomena in Stellar Atmospheres*, edited by R. N. Thomas, [Academic Press, New York], p. 405
- Morton, B. R., Taylor, Sir Geoffrey & Turner, J. S., 1956, Turbulent Gravitational Convection from Maintained and Instantaneous Sources, *Proc. R. Soc. London, Sec. A*, 1, 234
- Noguchi, K., Pariev, V. I., Colgate, S. A., Beckley, H. F., & Nordhaus, J., 2002, Magnetorotational Instability in Liquid Metal Couette Flow, *Astrophys. J.*, 575, 1
- Pariev, V. I., Colgate, S. A. & Finn, J. M., 2001, A Magnetic  $\alpha\omega$  Dynamo via Star-Disk Collisions in AGNs, (In Preparation)
- Parker, E. N., 1978, *Cosmical Magnetic Fields: Their Origin and Their Activity*, [Clarendon Press, New York]
- Parker, E. N., 1955, Hydromagnetic Dynamo Models, *Astrophys. J.*, vol. 122, pp. 293-314
- Pedlosky, J., 1987, *Geophysical Fluid Dynamics*, [Springer, New York]

- Ponomarenko, Yu. B., 1973, On the Theory of Hydromagnetic Dynamo, *J. Appl. Mech. Tech. Phys.*, vol. 14, pp. 775
- Prandtl, L., 1952, *Essentials of Fluid Dynamics*, [Hafner Pub. Co., New York]
- Priest, E. R., 1982, *Solar Magneto-hydrodynamics* [D. Reidel Pub. Co., Boston]
- Rädler, K. -H., Apstein, E., Rheinhardt, M. & Schüller, M., 1998, The Karlsruhe Dynamo Experiment. A Mean Field Approach, *Studis geoph. et geod.*, [Prague], 42, pp. 224-231
- Rieutord M. & Zahn, J. P., 1995, Turbulent Plumes in Stellar Convective Envelopes, *Astron. Astrophys.*, 296, 127
- Roark, R.J. and Young, W.C., 1975, *Formulas for Stress and Strain*, McGraw-Hill, NY
- Roberts, P. H. & Soward, A. M., 1992, Dynamo Theory, *Ann. Rev. Fluid Mech.*, 24, 459
- Sánchez, O., Raymond, D. J., Libersky, L. & Petschek, A. J., 1989, The Development of Thermals from Rest, *J. Atmos. Sci.*, 46, 2280
- Scalo, J. M. & Ulrich, R. K., 1973, Studies of Evolved Stars. I. Plume Mixing in S and N Stars, *Astrophys. J.*, 183, 151
- Schmidt, W., 1941, *Z. Angew. Math. Mech.*, 21, 265, 351
- Schmitt, J. H. M. M., Rosner, R. & Bohn, H. U., 1984, The Overshoot Region at the Bottom of the Solar Convective Zone, *Astrophys. J.*, 282, 316
- Singh H. P. & Chan, K. L., 1993, A Study of 3-Dimensional Turbulent Compressible Convection in a Deep Atmosphere at Various Prandtl Numbers, *Astron. Astrophys.*, 279, 107
- Stein, R. F. & Nordlund, A., 1989, Topology of Convection Beneath the Solar Surface, *Astrophys. J.*, 342, L95
- Stieglitz, R. & Müller, U., 2001, Experimental Demonstration of a Homogeneous Two-scale Dynamo, *Physics of Fluids*, vol. 13, pp. 561–564
- Taylor, G. I., 1945, Dynamics of a Mass of Hot Gas Rising in Air, *United States Atomic Energy Commission*, MDDC 919, LDAC 276
- Thompson, P., 1988, *Compressible-Fluid Dynamics* [RPI, New York]
- Ulrich, R. K., 1970a, Convective Transport in Stellar Atmospheres, I: A convective Thermal Model, *Astrophys. Space Sci.*, 7, 7

- Ulrich, R. K., 1970b, Convective Transport in Stellar Atmospheres, II: Model Atmosphere Calculation, *Astrophys. Space Sci.*, 7, 183
- Ulrich, R. K., 1970c, Convective Transport in Stellar Atmospheres, III: Multi-Stream Atmospheres, *Astrophys. Space Sci.*, 9, 80
- Zahn, J. P., 2000, *Astrophysical Turbulence and Convection* ed. R. Buchler and H. Kantrup, [Ann. New York Acad. Sci.], 898, 90
- Zeldovich, Ya. B., Ruzmaikin, A. A. & Sokoloff, D. D., 1983, *Magnetic Fields in Astrophysics*, [Gordon and Breach Science Publishers, New York]